Spring 5-31-1994

Particle dynamics modeling of vibrating granular beds

Yidan Lan

New Jersey Institute of Technology

Recommended Citation

Lan, Yidan, "Particle dynamics modeling of vibrating granular beds" (1994). *Dissertations*. 1078.
https://digitalcommons.njit.edu/dissertations/1078

ABSTRACT

Particle Dynamics Modeling of Vibrating Granular Beds

by
Yidan Lan

Particle dynamics modeling is done to study the behavior of granular beds subjected to vibrations imposed by a plane boundary which oscillates sinusoidally about a zero mean speed. Significant differences between the lower and higher shaking acceleration regions are found for the granular temperature and solids fraction depth profiles, which characterize the effectiveness of the boundary in fluidizing the beds. When higher accelerations are applied, the temperature is maximum at the vibrating floor and attenuates through the depth, while the solids fraction profiles exhibit a maximum at some intermediate depth. At lower acceleration values, most of the mass is located near the bottom, and fluidization occurs on the top, where a high temperature and low solids fraction is found. Simulation results are in good agreement with the kinetic theory predictions of Richman et al. in the higher acceleration regions and quantitatively consistent with the experimental data of Hunt et al. in the lower accelerations. Diffusion coefficients, computed using both the velocity autocorrelation function and the Einstein relation, are in agreement with each other and with the theoretical predictions of Savage. Critical conditions to produce a convective flow and associated segregation phenomena in a frictional bed are carefully investigated. The cell size, friction coefficient, agitation amplitude and acceleration are found to be the crucial factors. The first observation in simulation of an arching movement near the bottom of a large cell is also reported.

PARTICLE DYNAMICS MODELING OF VIBRATING GRANULAR BEDS

by
Yidan Lan

A Dissertation
Submitted to the Faculty of
New Jersey Institute of Technology
in Partial Fulfillment of the Requirements for the Degree of
Doctor of Philosophy

Department of Mechanical Engineering

May 1994

APPROVAL PAGE

PARTICLE DYNAMICS MODELING OF VIBRATING GRANULAR BEDS

Yidan Lan

Dr. Anthony D. Rosato, Dissertation Advisor — Date
Associate Professor of Mechanical Engineering, NJIT

Dr. Rong Chen, Committee Member — Date
Professor of Mechanical Engineering, NJIT

Dr. Rajesh N. Dave, Committee Member — Date
Associate Professor of Mechanical Engineering, NJIT

Dr. Ian S. Fischer, Committee Member — Date
Associate Professor of Mechanical Engineering, NJIT

Dr. Mark W. Richman, Committee Member — Date
Associate Professor of Mechanical Engineering
Worcester Polytechnic Institute

BIOGRAPHICAL SKETCH

Author: Yidan Lan

Degree: Doctor of Philosophy in Mechanical Engineering

Date: May 1994

Undergraduate and Graduate Education:

- Doctor of Philosophy in Mechanical Engineering,
  New Jersey Institute of Technology,
  Newark, New Jersey, 1994
- Master of Science in Mechanical Engineering,
  New Jersey Institute of Technology,
  Newark, New Jersey, 1989
- Bachelor of Science in Mechanical Engineering,
  Shanghai Institute of Technology
  Shanghai, P. R. China, 1982

Major: Mechanical Engineering

Presentations and Publications:

Rosato, A. D., and Y. Lan,
"Discrete Element Modeling of Vibrating Granular Beds." *Powders & Grains* (1993),241-246, A.A. Balkema Publ., Netherlands

Rosato, A.D., and Y. Lan, and D. Wang.,
"Vibratory Particle Size Sorting in Multi-Component Systems." *Powder Tech.* 66 (1991):149-160.

O'Brien, K.T., A. D. Rosato, and Y. Lan.,
"Segregation in the Flow of Polymeric Particulates with Two Constituents." *Proc. of Annual Technical Meeting, Society of Plastics Engineers, Dallas, Tx.* (1990)

This dissertation is dedicated to
my mother, my wife and my family

ACKNOWLEDGMENT

The author wishes to express his sincere gratitude to his advisor, Dr. Anthony D. Rosato, for his guidance, friendship, and moral support through this research.

Special thanks to Drs. Rong Chen, Rajesh N. Dave, Ian S. Fischer and Mark W. Richman for serving as members of the committee.

The author would like to thank Dr. Mark W. Richman of Worcester Polytechnic Institute for many stimulating discussions and for furnishing the theoretical predictions. The author is also grateful to Dr. Otis R. Walton of Lawrence Livermore National Laboratory for providing a granular shear code which was modified for the purpose of these studies.

TABLE OF CONTENTS

TABLE OF CONTENTS
(Continued)

Chapter **Page**

LIST OF TABLE

Table **Page**

LIST OF FIGURES

CHAPTER 1

INTRODUCTION

1.1 Overview

Granular materials, such as sand on the beach and sugar in a bowl, are so familiar to everyone that it is hard to imagine that the behaviors of these materials, subjected to disturbances, are far from being understood even today. This provides the main motivation of this particle dynamics simulation research on granular material.

In this work, the focus is on understanding the behavior of granular assemblies in a vibrating bed and investigating the coupling between the boundary motion and that of the particles.

The major contributions of this work can be summarized as follows:

- Relations between the granular temperature, solids fraction and boundary shaking acceleration, using a 3-D dynamics simulation method have been identified.
- Velocity autocorrelation and diffusion coefficients in a vibrated uniform granular bed are computed.
- Convection and segregation in 3-D computer simulation of a vibrating granular bed has been achieved and an analysis of the large sphere movement in response to the boundary shaking has been done.

In general, the results of this study have a great potential for industrial applications.

1.2 Literature Survey and Motivation

Granular material or bulk solids is the name given for a collection of discrete solid components of any size-range which are in contact or near contact with immediate neighbors. Owing to the particular structure, granular materials display a variety of properties that are totally different from those of other substances, one of which are the phenomena caused by vibration.

The behavior of vibrating granular beds has been of much interest to industries which process granular materials, such as plastics, powder metals, ceramics, food and pharmaceuticals (1, 2). The related studies can be traced back to over 150 years ago when Faraday (3) proposed the cause of convection driven by large-scale vibration. Since recent analogies have been found between the physics in a sand pile and that in superconductors (4), an increasing number of papers have been devoted to the dynamics of granular materials.

Due to the difficulties of obtaining the measurements of individual particle motions, early experimental studies on packed beds submitted to vibration concentrated on phenomenological results and explanations. Recent developments in image processing techniques have made two-dimensional experiments tractable in obtaining the micro-structural information. However, experiments for 3D tracking are scarce due to the expense (for example radioactive techniques) and difficulties in non-intrusive measurements.

Theoretical treatments of vibrated beds were rare a decade ago; however, advances in kinetic theory of granular flows now make it possible to study the problem analytically (5). Kinetic models use assumptions, such as the form of velocity distribution function, instantaneous binary collisions and simplified boundary conditions. Despite this, many collision-dominated flows can be at least qualitatively predicted with these theories.

Different from real experiments, discrete computer simulation methods (6), viewed as 'numerical experiments' based upon the solution of Newton's law of motion for the energy dissipating system of interacting particles, have been developed to provide dynamic properties (particle trajectories, collision forces and so on) of individual grains. From this information, subsequent calculation of macroscopic behavior, such as granular temperature and solids fraction, can be computed, and the effects of various boundary conditions on the granular bed can be studied. The results of computer simulations may be used to test the theories and discover new phenomena, and to compare with the results of physical experiments. In this sense, computer simulations act as two bridges, one between the numerical models and theoretical predictions, the other between models and experimental data.

Before going further to study vibrating beds, it is necessary to review the literature to date.

1.2.1 Two Opposite Effects of Boundary Shaking on Granular Assemblies

It has been known for a long time that imposition of boundary shaking on a granular assembly can produce two dramatically different effects: either the bed will densify or it will become fluidized. Although these two effects are closely related, most studies treated them as two separate phenomena, and concentrated only on density changes for compaction and surface flow for fluidization.

Densification of particulate media by vibration, known as vibratory compaction (7), is extensively used in industries. This technique involves the supply of increments of energy to the bed of particles at a selected frequency for a fixed time period. Increases in density of 4 to 11 percent were reported when vibrational methods were applied to the containers in a packing machine for sunflower seeds (8). The vibration of mine cars, which carry coal or ores, raised the density by 13 percent (8). In the early literature, five parameters of vibration, namely frequency, amplitude, acceleration, energy input and power input, were identified, one or more of which may be instrumental in causing the compaction of the packed bed (7). As early as 1951, Stewart (9) pointed out that a consolidation state of "maximum density" could be achieved at high frequencies and low amplitudes. The existence of a critical frequency for maximum compaction has been further confirmed by Gray (7). By placing a small load on a powder bed, Shatalova et al. (8) measured the most effective frequency ranges to achieve minimum porosity. They found frequency ranges of 100 to 200 Hz for large particles over 100 μm, 200-300 Hz for intermediate size, and over 300 Hz for small particles less than 1 micron. Acceleration was considered as the most effective parameter by Cussens and Plowman (10,11). An acceleration of 4g to 7g was recommended for table vibrators by Shatalova et al. (8). On the hand, Macrae et al. (12) argued that the densest packing was related directly to impact velocity, which may be produced by different stop settings of the container during a vibrating cycle. Besides vibratory parameters, particle shape, initial poured density, coherence and pressure on the bed also play a very important roll on the rate of compaction (7). Most of the studies on this phenomena were aimed at industrial applications, and little attention has been paid to understand the underlying physics.

Fluidization phenomenon in granular materials under vibration is a more challenging topic in science and technology. One example (13) is the fluidization of a sand pile submitted to large enough vertical vibrations. Using two vertical, coaxial tubes and an expansion vessel, which was connected with the inner tube, Eversque et al.(14) found that sand surface became fluidized and flowed down from the inner tube to the outer tube when the apparatus was vibrated sinusoidally at a high enough amplitude. After shaking, the cone shape surface of sand in the outer tube had crept up and became flatter. According to his observation that the fluidization part was confined to an upper layer of the bed, he argued that fluidization began from the surface, in contrast to most of theoretical approaches, which predicted a fluidization thickness from the bottom where energy input was applied.

Studies in vibration induced fluidization in a shallow bed were initiated by Bachman (15) who in 1940 proposed the first model of this type of bed. More recently, Thomas et al. (16) conducted experiments on sinusoidally vibrating shallow granular beds with static bed depths ranging from 24 μm to 30 mm. Through a thin, rectangular transparent vessel, they measured the critical values of vibrational intensity $Kcr = a\omega^2/g$, the ratio of maximum shaking acceleration to gravitational acceleration, at which shallow beds became " mobilized ". It was found that *Kcr* was very sensitive to particle size, cohesiveness and the initial packing state of the beds. For particles larger than 100 µm, their results showed that *Kcr* = 1 in spite of the initial packing state. *Kcr* increased monotonically as particle size was reduced below 100 µm. For fine and aeratable particles, *Kcr* was significantly higher in a densely packed bed than in a loosely packed bed. During the experiments, a phase-delayed trigger flashing system was used to take photographs for all desired shaking phase angles, from which four vibrated-bed states were distinguished by the degree of fluidization as the bed depth increased. Two 'Newtonian states' were identified for such states whereby the particles' trajectories were governed by Newtonian mechanics. The bed depths before shaking were usually less than one layer. During shaking, the highly dispersed particle pattern remained unchanged for different phase angles in the Newtonian-I state. But with a small increase of initial bed depth, notable changes were observed forming a Newtonian-II state, where uniformly distributed particles would segregate and form a dense band near the vibrating floor during a portion of a cycle. As the bed depth increased to 3-10 layers, a state, called the "coherent- expanded state", was attained. Under the influence of the aerodynamic effects, the bed moved together as a loosely packed coherent mass. As the bed collided with the floor, a rush of upward air from the gap produced a large expansion of the bed. With further increase of bed depth, a transition was found in which the bed expansion diminished. Thomas et al. termed this the " coherent-condensed state", since a condensed region of material appeared in the lower part of the bed and changed little during the vibrational cycle. It is worth mentioning that Thomas et al. found that the bed depth, particle properties (including coefficient of restitution) and aerodynamics were the primary factors affecting transitions from one state to another. They also provided a nondimentional bed- permeability parameter, which included the effect of the viscous drag force of the gas, to characterize and determine the transitions between any two states.

The density profile and velocity field in the vibrating bed are important in identifying the region and degree of fluidization. With the help of innovation in experimental methods, Clement and Rajchenbach (17) quantitatively measured these parameters in a bidimensional vibrated bed of steel spheres. The snapshots for small amplitudes of shaking, which were recorded every quarter of a shaking period, showed that the grains in the deep layers remained in triangular arrays after shaking, while the upper four or five layers were thermalized and a few particles jumped out of the bed. Averaging the data from particle displacements, density and velocity fields were calculated by a computerized technique. They confirmed that the mean density increased with the depth from the free surface, while the particles exhibited a small random velocity in denser regions. Unlike density, which was found to be independent of shaking phase, the average velocities changed periodically as the phase angle changed. Its horizontal components deviated slightly around zero, but vertical velocity components varied significantly during the cycle, with small changes along the height. Their velocity distribution calculations exhibit an approximate Gaussian and isotropic trend.

With a video recorder, Hunt et al. (18) measured the average solid fraction and bed height in a glass-walled rectangular box, which was driven by an eccentric cam mechanism. Three different bed masses of glass spheres, corresponding to three different initial bed heights, were tested. For a fixed amplitude of 1.67 times of sphere diameter, they found a critical acceleration value of 2 g, below which no obvious changes in bed height and average solid fraction were observed, while beyond this value, significant bed expansion and solid fraction decrease were found. They also noticed the local solid fraction varied with the distance from the bottom of the bed and changed during the vibration cycle, which is quite different from Clement and Rachenbach's (17) two-dimensional observation. When amplitude was reduced to the particle diameter, the critical value of acceleration decreased to 1.3 g. A critical frequency value was identified to be independent of vibration amplitude. The first critical frequency was found at 10 Hz at which the bed expansion began and solid fraction decreased. The solid fraction curves tended to be flat above 12 Hz , until the second critical frequency appeared at about 18 Hz , where a thick bed showed a further decrease. The data suggested that the minimum value of average solid fraction was approximately 0.21 for all vibrated beds used in their studies.

Recent in a three-dimensional Monte Carlo simulation approach by Mehta and Baker (19) demonstrated for the first time the compression and dilation effects in granular materials within a single mode of vibration. A local cluster of particulates in a granular pile was modeled as an assembly of potential wells, while the vibrations of particles was regarded as random noise. The large noises caused the particles to eject, while the small noises let the grains reorganize and minimize the voids. Using a sequential random close-packing algorithm, N monodisperse hard spheres were placed in a box with periodic side boundaries. The "shake cycle" began by raising the spheres above a distance of shaking amplitude in Z direction, while shifting the particles randomly around in X and Y directions. A Monte Carlo procedure, proposed by Rosato et al. (2), was used to simulate the falling of the assembly. They observed a threshold of shaking amplitude, above which, the volume fraction fell off sharply, while below this threshold, it increased. Lower mean coordination numbers in a large amplitude shaking bed reflected the existence of bridges, arches and other voids generating by this shaking. A prominent peak in pair-correlation function of sphere separation for the small amplitude shaking case indicated a significant second-neighbor shell at that time. Upon comparing the pair-correlation function for displacements in the transverse direction with those in longitudinal direction, they pointed out that the motion of neighbors above and below a particle played a more important roll than those of other neighbors in the reorganization process of the system. Large topological changes were found in the contact network of the bed subjected to large amplitude vibration, as compared with small changes in those submitted to small amplitude shaking. Although Mehta and Baker had not described the detail dynamic changes and difference between the compression and dilation stages, they have, for the first time, observed and pointed out that these two opposite effects could exist in the same vibration model only if vibrational parameters were chosen correctly.

1.2.2 Convection, Diffusion and Mixing in a Vibrating Bed

Closely related with fluidization, convection and diffusion are also typical phenomena, which have been received more and more attention in the research of vibrating bulk assemblies.

When Evesque and Rajchenbach (13) used a loudspeaker to shake a monodisperse glass sphere bed, they found that beyond a threshold of amplitude, the horizontal free surface became inclined until its slope reached an angle slightly smaller than the maximum angle of repose. An avalanche flow down the slope surface and an internal convective transport, which refilled the top of the hill, were developed in the bed simultaneously. This process occurred under a specific ratio of the bead's diameter to the displacement amplitude. They confirmed that the key parameter responsible for the instability was the amplitude of acceleration, which must exceed the acceleration of gravity "g", and appeared to be independent of the size of the beads, but related with the size and shape of the container. An alternate change in the packing of the bed was proposed to explain this situation. When the cell was raised up, the bed experienced compaction which locked up the interparticle motion. While the cell was going down, the bead were submitted to an upward acceleration and became mobile if a shaking acceleration larger than "g" was applied to the cell. It was also noticed that a chaotic pattern, with ballistic phenomenon on the top, appeared when much larger amplitude was applied and convective flow disappeared.

Using Reynold's concept of dilatancy, Rajchenbach (20) went further to analyze the formation of a small bump on the horizontal free surface. Disturbed by the vibration, a gradient of random velocities was developed in the bed, which generated an internal flow of particles from the less compressed regions to the more compressed regions. This internal flow caused the bump, and a downward avalanche flow took place when the slope of bump exceeded the angle of repose. Rajchenbach introduced an interesting experiment to show this internal flow by using a U - shaped pipe filled with an equal level of powder in both its branches. After shaking the tube for some time, the level of powder in one of the branches increased, which Rajchenbach explained as lack of surface avalanches due to the geometry of the pipe.

Faraday (3), considered one of the pioneers in this field, believed that air was instrumental for the circulatory motion in the powder pile. When the particulate mass loses contact with the bottom plate during upward motion, the air rushes into the gap from the perimeter and carries the particle mass towards the center. Recent studies of Savage (1), Evesque and Rajchenbach (13) and Rajchenbach (20) have shown this to be incorrect. Savage did not find any noticeable difference by replacing his solid vibrating plate with a plate containing air holes. Other workers also found no change for the value of the threshold by comparing their measures in air with those in vacuum.

Savage (1) considered the " acoustic wave" sent by the base as the cause of the convective flow and the source of the fluidization. Due to the dissipation in collisional interactions, he predicted an attenuation of those waves. His rectangular shaking box had a flexible metal bottom which enabled non-uniform amplitude vibrations across the width of the base. With a maximum amplitude at the center and nearly zero amplitude at the side walls, the bottom induced waves upwards through the bed. This caused a slow recirculation in which particles moved upwards in the center region of the bed and moved down near the side walls. By measuring the streamlines of this convection flow, Savage found that the circulatory velocity increased as the shaking frequency or amplitude increased, reached a maximum value, and then decreased with further increase in frequency and amplitude. The collisional contact of particles with the vibrating bed over the complete cycle was regarded as the primary source to maintain and enhance the convective motion. Savage explains this as follows. By using too high a frequency or amplitude, yielding an acceleration larger than a critical value, the circulation would be reduced, since the particles lose contact with the vibrating floor over part of the cycle, and hit the floor too hard when the bed is moving upward from its lowest position. Using the analogy between recirculating flows and "acoustic streaming" in the air, Savage developed an approximate theoretical analysis of convection after introducing a modified constitutive theory and simplified assumptions. The results from experiments compared well with the theory except for a slight overestimate in velocities.

Based on his 2D numerical simulation results, Taguchi (21) postulated that convection was induced by the elastic interaction between the particles. A viscosity term was included in his force model, while rotation was omitted. In order to reproduce other experimentalists' results, a larger viscous friction was used between sphere and side walls than that between particles. Acceleration amplitudes $b\omega_0^2$, were tested up to 4g by fixing the displacement amplitude "b" and changing ω_0. The test cell was partitioned into small grid-like cells. The strength of convection flow was measured by counting the time average number of particles passing through the small cells, which were fixed to the original cell. A critical acceleration amplitude value 1.2g was found when the convection strength become nonzero. Taguchi argued that the convection region first appeared near the surface, and then expanded downward as vibration strength increased, from which he found an agreement with Evesque et al.'s (14) concept of surface fluidization. He also proposed his view about the origin of convection. Two stages were distinguished in a shaking cycle. When the acceleration of gravity was larger than the downward acceleration of the base, the particles were pressed and stresses developed between them. During the interval when downward acceleration of the bottom became greater than the acceleration of gravity, the particles were in free flight. The former developed vertical stresses could easily relax in this time period, while horizontal stresses, restricted by the side wall, couldn't be released, thereby promoting relative horizontal sliding motion between particles. Taguchi did not explain why the induced horizontal flow would meet at the center of the cell, turned upwards and created a bump. He disagreed with Rajchenbach's (20) assumption that heaping caused the convection. In contrast, Taguchi thought convection was the origin of heaping.

With the help of a two-dimensional discrete element simulation, Gallas et al. (22) investigated several types of convection cells. A sinusoidal vibration was introduced through the base, where the amplitude was a cosine function whose amplitude could be varied along the width of the base. Three forces, (that is, an elastic restoration force, a dissipation force due to collisions and a shear-induced friction force), were incorporated in the collision model, while Coulomb friction and particle rotations were neglected. Since the influence of the elastic modulus on the results was negligible, a very small value was chosen to save computer time. When periodic boundary side "walls" were applied, the authors observed upwards motion of particles near the center where the amplitude was the largest. A resonance phenomenon occurred around 60 Hz, where the upper center part of the bed was not in contact anymore and average vertical velocity components reached a maximum. Another type of convection was reported when fixed frictional side walls and a uniform amplitude of the base were applied. In this case a strong trend of downward motion was observed at each side wall. An explanation of convection mechanism similar to Taguchi was given in that case. When the bed is brought upwards, the upward motion of particles with respect to the wall is reduced by a large shear friction, created from the strong pressure exerted on the walls by the compressed packing. As the bed falls down, the packing becomes looser. Particles tend to separate in the vertical direction, but interact with its horizontal neighbors with smaller friction restraint, thereby allowing the downward motion of particles with respect to the walls. An interesting phenomenon occurred when the fixed walls had no shear friction. One convection cell, not two could be found, but the motion of particles near the wall was quite uncertain, either upward or downward. Gallas et al. thought the horizontal particle flow near the bottom would reinforce at each cycle. When the fixed wall prohibited this flow, the particles were forced to move upwards. In their simulation, they also found convection did not depend on the initial condition, which provided evidence that convection was not a transient effect.

Diffusion is an important transport phenomenon associated with non-uniformity in composition or other properties. In a granular bed, the diffusion coefficients relate the particle flux to a concentration gradient, and this has a direct influence on mixing and segregation.

Savage and Dai (23) have examined the self - diffusion problem in an 'unbounded ' granular flow. From a statistical mechanics point of view, the diffusivity tensor can be found by computing the velocity autocorrelation tensor, whose components can be expressed in general as an exponentially decaying function. Kinetic theories for granular flows have been used to analytically estimate the relaxation time of this decay function. By taking the single particle velocity distribution function to be a perturbed Maxwellian and considering only binary collisions, Savage and Dai developed an expression for the self - diffusion coefficients as,

$$D = \frac{\sigma\sqrt{\pi T}}{8(1+e)\cdot \nu \cdot g_0(\nu)}$$

where $g_0(\nu)$ is the Carnahan - Starling expression for the radial distribution function evaluated when particles are in contact, T = $\langle C^2 \rangle / 3$ is the "granular temperature", and $\langle C^2 \rangle$ is the second moment of the deviatoric velocity. They also computed the self-diffusion coefficients from the velocity autocorrelation by using the results of granular dynamics simulations of unbounded shear flows. The calculation was very time consuming, since it required ensemble averages for long time periods.

Hunt et al. (18) have derived the same analytical expression for self-diffusion coefficient *D* using a different approach. In order to calculate *D*, a rough estimation was used to express the temperature. It was assumed that particles near the vibrating boundary had the same vertical velocity as the boundary and negligible velocity components in the horizontal directions. In fact, they approximated the granular temperature of the vibrated bed as the temperature associated with the vertical sinusodal velocity fluctuations of the boundary. After obtaining *D* , the diffusive mixing time expression was found by solving a 1-d diffusion equation with appropriated boundary conditions at the bottom and top surface. This theoretical mixing time result, compared with crude experimental measurements, showed relatively good quantitative agreement. In their experiments, the mixing time was computed from the changes in digital images. Several layers of blue glass sphere were placed above an equal thickness of red spheres before shaking. During shaking, pictures were taken by a video recorder at a rate of 60 image per second. The change in color distribution was analyzed and averaged by computer to determine the mixing degree. Their results for diffusive mixing and bed expansion (discussed in last section) indicated that they are two closely related phenomena. No mixing was observed in the bed when the acceleration was under 2.0 g. As the acceleration increased , the mixing time decreased dramatically and the bed expanded significantly. They also found the spacing between the front and back wall did not affect the results greatly. Another important observation was that they did not discover any recirculation pattern in their experiments, which suggests that convection and fluidization can exist separately.

As opposed to the results of Hunt et al. (18), Zik and Stauans (24) observed the convection flow of glass beads (diameter = 0.1 cm) in their vibrating cell — a 12 cm long, 1 cm wide and 10 cm high glass box. Their experimental work showed how to successfully isolate two different transport phenomena—convective transport and diffusive transport. Consequently they were able to measure the self-diffusion coefficient. By applying a vibration amplitude of 0.07 to 0.16 times particle diameter and high frequencies

(80-120 Hz), instability, such as surface heaping and convection streaming along the longitudinal direction, was minimized. However they did observe a transverse convective flow, whereby the bead moved down near the lateral boundaries and traveled upwards to the top in the bulk. To further minimize the longitudinal flows, they cemented a layer of beads on the small side wall and let the long side wall be smooth. Diffusion along the free surface was prevented by dipping some comblike metal sheets into the top surface, which allowed the surface particles to move transversely only. By coloring the beads located in a center strip of the cell and observing its progressive widening, they could measure the diffusive transport in longitudinal direction quantitatively. The concentration of colored particles was decided by the intensity of the light transmitted through the bead layer, which was then averaged over the height. A mean square width of the concentration was calculated and used to define a diffusion coefficient. Their experiments indicated that self-diffusion coefficient was independent of vibration frequency and amplitude, but linearly related to the transverse convective velocity. With a small convection, no concentration change could be seen in the lower part of the bed. No mixing occurred when convection was very small and the particles seemed to follow the vertical oscillations of the cell.

1.2.3 Different Opinions on the Cause of Segregation

A widely occurring phenomenon in granular materials associated with vibrations or shearing is known as size segregation. In fact, bulk particulates tend to unmix when subjected to various forms mechanical disturbances. Segregation has been observed in pouring and shearing; however, vibration is one important and not well-understood external driving force to cause segregation, whereby the largest particles rise to the top of the bed while the smaller particles fall to the bottom. Size segregation is usually an undesirable effect when product homogeneity is required, but there are some useful applications. In chemical, pharmaceutical, plastic and powder metallurgy industries, segregation causes serious problems, such as uneven quality, varying in packet weight and low mechanical strength. As an example, in plastic field (25), vibrational conveying of mixtures of several different types of polymers leads to the separation between the components. In contrast, segregation facilitates separation in batch sieving or classification processes. It is clear that although segregation and mixing are two opposite phenomena, both are concerned with local particle rearrangement mechanisms.

1.2.3.1 Some of the Early Work on Segregation

One of the early studies on segregation was done by J. C. Williams (26). He noted that although other factors contributed to segregation, such as density and shape, the principle factor appeared to be particle size discrepancies. In order to examine the causes of vibrational segregation, he placed a single large ball at the bottom of a glass beads bed. When the bed was subjected to vertical agitation, the large ball could always be made to rise even if its density was greater than that of the bed. An explanation was introduced in term of pressure below the surface of the large sphere. He hypothesized that the large ball would move up as long as the pressure beneath it was sufficient to prevent the movement of the small particles. But this mechanism fails to explain why an empty ball and one full of mercury both rose to the top of the bed.

Interparticle percolation has been experimentally studied by Bridgwater et al. (27) (28). The layers of particles act as a screen through which all but the large particles are able to pass and reach the stationary region below. However, when particulate sizes are comparable, the smaller particles cannot sift through the gaps formed by the larger ones.

Ahmad and Smalley (29) carried out the same type of experiments as Williams (26). They measured the time for a large particle to rise to the surface of a sand-filled vibrated bed. An acceleration range of 1-10 g and frequency range of 50-150 Hz was used. It was obsevered that acceleration was an important factor affecting the segregation. Segregation increases with an increase in acceleration for all fixed frequencies, but it was reduced with increasing frequency at a constant acceleration. It was also confirmed that the greater bed depth, the greater segregation time, while the greater the size of the large ball, the greater the tendency to segregate. Shape was not considered as a significant factor under all vibrating conditions.

With the help of radioactive tracer, Harwood (30) measured the segregation effect in real powder systems. The powder materials were selected to be of different cohesion, different size and density. The powder properties as well as vibratory parameters had profound effect on the results. Significantly increased segregation was observed when powder was fluidized under sufficient energy.

Kawakita (31) is perhaps the first person who noticed the effect of convectional flow on segregation. He hypothesized that the middle part of the bed was more porous than at the side walls, and this resulted in a movement of surrounding particles to the center. A falling flow was therefore developed at the sidewall, while rise flow developed in the center of the container. The velocity difference of convectional flow between large and small particles was proposed as one of the cause of vibrational segregation.

1.2.3.2 Recent Results on Size Segregation

Recent research on size segregation has been focused on quantitative modeling of the segregation process. Monte Carlo simulations and dynamics simulations have demonstrated great potential in characterizing various mechanisms by which the large particles segregate.

A shear-driven mechanism was proposed by Haff and Werner (32) in 1986 in a two-dimensional particle dynamics simulation to model the mechanical sorting of inelastic frictional disks. Shearing motion was applied to a pan, filled with uniform small grains and a large grain on the bottom, by introducing vertical and horizontal harmonic oscillations. The interactive normal force in their model is taken to be proportional to the amount of overlap between disks, while the tangential force is modeled using a Coulomb type friction law. In addition, a velocity-dependent damping term is employed to affect the collisional energy loss. Simulation results indicated that the amount of shear induced in the system had a strong influence on the degree and rate of sorting. It was argued that the relative rotation of particles promoted the segregation. Sufficiently high friction helped the large particle roll up over small adjacent particles, and ensured the smaller particles supporting the large one. On the other hand, frictionless particle exhibited little or no sorting tendency, since absence of grain rotation prohibited large particle from rolling up on to smaller ones.

A geometric mechanism by which vibratory segregation occurs was identified and isolated by Rosato et al. (2, 33) using a Monte Carlo simulation. Hard disks were randomly place in a container and then allowed to collapse under gravity to an equilibrium state. Shaking was simulated by repeatly lifting the assembly by a prescribed amplitude and then allowing it to collapse until equilibrium was attained. The effect of interparticle collisions and collisions with walls were modeled as random movements of the particles with respect to one another. It was demonstrated in the simulation results that the size difference created more opportunities for the small disks to fill a void which opened beneath a large one. It was shown that for a fixed size ratio (large to small diameter), an increase in the shaking amplitude resulted in a faster segregation, which is in qualitative agreement with the experimental results presented by Ahmad and Smalley (29). The specific dependence of segregation rate on time demonstrated the strong influence of local geometric structure near the large particle on the sorting mechanism, which is quite different from Williams' (26) explanation. In binary systems (34), segregation could be traced by the progression of the interface line separating the mixed region from the sorted layers. This method has been extended to multi-component system (35), by Rosato, Lan and Wang to qualitatively investigate the effects of size ratios on the rate of segregation. The concept of mutual sorting was introduced from which generalized expressions were derived for the rate of change of the size species concentrations. Simulation results showed good agreement with the theoretical predictions regarding the influence of size ratio. With a change of size ratio, a reversal of sorting order between small and large particle in a ternary system was predicted by the theory and verified by the simulation. They further confirmed that the sorting of the intermediate size was always delayed despite of size ratio.

A three-dimensional Monte Carlo model has been used to simulate the procedure of vibratory size segregation by Jullien and Meakin (36). Using periodic boundaries in the lateral direction, they created a packing of 250 large spheres and 50,000 small sphere. They also simulated the upwards motion of a single large sphere in a random packing of small spheres. After studying the dependence of the height of the large sphere, they found a size ratio threshold value of 2.8, below which the maximum upward displacement of the large sphere remained finite.

Recent experiments with a single large glass bead in a vibrating bed of small beads by Knight, Jaeger and Nagel (37) proposed a mechanism similar to Kawakita's (31). A symmetric convection cycle was observed. All the spheres, regardless of size, were found to rise in the middle at the same rate. The large sphere was trapped on the top, and failed to join in the downward motion of small particles along the walls. The rise velocity depended on the depth below the top surface. They argued that the boundary conditions at the wall were crucial for creating convection. Their claim, that segregation is caused by convection is confusing in light of their experimental data showing that large spheres of different sizes rise at the same rate. Consequently, convection cannot differentiate between sizes and therefore does not result in size sorting.

1.2.4 Kinetic Theory Approach in the Studies of Granular Flows

Fifteen years ago when Ogawa (38) first suggested the idea of granular temperature, the kinetic theoretical approach for granular flows was just at the beginning. Taking the advantage of the physical similarity between rapid granular flows and dense gases, Savage and Jeffrey (39) , Lun et al. (40) and Jenkins and Richman (41) have successfully developed various kinetic theory models for granular flows, by including the energy dissipation due to inelastic collisions. The concept of granular temperature is the most important key to understanding the behavior of collision-dominated granular flows. The velocity of each particle may be viewed as a sum of the mean velocity of the bulk material and a random component, which is the fluctuating component of the particle motion. Granular temperature, defined as the mean square value of this random velocity, is the energy per unit mass contained in the random motion of particles. Since the collisions between real particles are inelastic, granular temperature is dissipated. To maintain the temperature, energy must be continuously supplied to the system to balance that lost during collisions. All of the kinetic theory models assume that the particles interact via binary collisions, usually using a constant coefficient of restitution to represent the energy dissipated by the normal impacts between the particles. The major constituent in the derived conservation equation is related to the conduction and dissipation of granular temperature.

These treatments have been proven successful, especially when boundary conditions have been imposed to solve different kinds of flow problems. For an example, Jenkins and Richman (41) employed the averaging technique in kinetic theory of dense gases to calculate the rate at which momentum and energy were transferred between flow disks and boundaries. Upon balancing the energy, they established boundary conditions for the shear stress, pressure and flux of fluctuation energy. Their work was later extended to smooth spheres by Richman (42), whereby a modified Maxellian velocity distribution was used to analyze the shear flow driven by the bumpy boundary. He predicted that as roughness in a boundary increased, the slip velocity would decrease, which has already been verified by other simulation work (43, 44, 45). Recently, following Richman's (42) boundary conditions and Jenkins and Richman's (41) constitutive theory, Richman and Martin (46) presented for the first time a theoretical calculation of the solid fraction and granular temperature depth profile in a top-unconfined granular bed, having a bumpy floor that fluctuated with a constant root mean square speed about zero mean velocity. They concluded that a deeper and more thermalized bed resulted with an increase in boundary fluctuation, and granular temperature increased monotonically from the top to the bottom, while the solid fraction achieved its maximum at an intermediate level. It is worthwhile mentioning that similar studies have completed by Richman and Mark to discuss different types of vibrating beds (47).

1.2.5 Motivation, Objectives and Methods

The unusual behavior of granular material has drawn more and more attention among the science and technology circles. Just like semiconductors which exhibit conduction or insulator-like behavior depending on the external electrical field applied, granular materials would experience a transition from solid to liquid-like state under certain circumstance. An open question is under what condition this transition would happen, and how to quantitatively describe them. Recent studies on vibrating bed have revealed the existence of a threshold, but most of them haven't investigated the details of this transition, partly because of the difficulties in getting the dynamic information about the motion of individual particles. For example, granular temperature, which is due to the random motion of the grains, should be an important avenue to investigate fluidization and diffusion phenomena, but no recent dynamics simulations and experiments have discussed this topic. The theoretical studies of Richman and Martin (46) on the relation between temperature and boundary energy provides an excellent basis with which to make comparison with dynamic computer simulations.

Mixing and segregation in vibrating bed is another topic having both scientific and technological importance. Various mechanisms and theories have been proposed; yet a micro-structural level understanding is still lacking. The experimental work of Hunt et al. (18) and Zik et al. (24) have measured diffusion coefficients, which is the basis for studying mixing and segregation. Their studies, neglecting the temperature and density gradient, treated the bed as a whole, without considering the possible differences along the depth. A more reasonable diffusion coefficient may be developed by using the dynamics simulation method, which may also provide microstructural information. Knight et al.'s (37) convective mechanism for segregation has suggested another mechanism that of grain transportation via convection, which the authors mistakenly call segregation. Using dynamics simulation to duplicate this phenomenon, and investigating the different response of small and large particles to the boundary shaking will be helpful to understand this behavior in detail. The phenomena of convection in a granular bed is itself a puzzle deserving of further study. This is especially true since the existing two-dimensional simulations haven't set up a relation between the convection flow and granular temperature.

With a purpose of establishing a three-dimensional dynamics model and comparing simulation results obtained with all existing assumptions, theories and experimental observations, this study will concentrate on the macroscopic properties of vibrating beds, such as granular temperature, solid fraction profiles and diffusion coeffecient. The effect of boundary shaking on size segregation will be also emphasized.

1.3 Outline of Thesis

Chapter 1 reviews previous work on the vibrating granular bed. Various mechanisms, theories and experiments are mentioned to highlight different opinions. Chapter 2 describes the dynamics simulation model used in this study. After briefly introducing Walton's soft sphere model, boundary conditions for the vibrating bed and modification of the code are presented in detail. In Chapter 3, methods employed to compute diagnostic and statistical parameters are explained. Simulation results for smooth uniform beds are reported in Chapter 4, where various physical quantities, such as granular temperature, solid fraction, diffusion coefficient and mean square displacement are calculated and compared with kinetic theory predictions and recent experimental results. Moreover, coupling between boundary and particle motion is examined by spectral and correlation analysis methods. Chapter 5 is concerned with convection and "segregation", where the critical conditions to produce a convective flow are provided. Convective motion and the movement of a large sphere in a frictional bed are analyzed quantitatively. Summary and conclusions are presented in Chapter 6, together with suggestions for further research.

CHAPTER 2

THREE-DIMENSIONAL PARTICLE DYNAMICS SIMULATION MODEL

The particle dynamics simulation is a technique derived from the molecular dynamics method used in the studies of dense fluids. Although molecular dynamics simulation has a long and rich history of almost 40 years, the rise of particle dynamics simulation in granular material occured in the 1970's. The basic concept and the main techniques of molecular dynamics simulation, concerning the deterministic solution of the classical N-body problem, have been retained. The major difference between molecules of fluid and bulk particulates is their interaction models. Energy conservation is essential to molecular systems, while energy dissipation is the characteristic of granular assemblies. In contrast to gas molecules, particulates can not be modeled by perfectly elastic collisions since these do not involve any kinetic energy loss. During a collision, a portion of kinetic energy is either dissipated in plastic deformation or converted into heat. Two approaches have been developed to approximate this interaction. By considering the particles to be infinitely stiff, "hard sphere" models assume instantaneous, binary collisions. A collision operator, which is a function of the particle properties (friction, normal and tangential restitution coefficient) and pre-collisional velocity, is used to compute post-collisional velocities. The "soft sphere" model, on the other hand, allows colliding particles to overlap a small fraction of their diameters, and the interaction force is a function of this relative overlap among other factors. Collisions involving continuous and multiple contacts can be modeled, since many time steps are considered in a single collision over which to integrate the equations of motion.

In this study, the "soft sphere" model, develop by Walton et al. (6), has been used to investigate the dynamic properties of a vibrating granular bed, with the objective of connecting the "microscopic world" described by Newton's law with the macroscopic behavior characterized by quantities such as granular temperature and time correlation functions.

2.1 General Structure and Techniques

The simulation code used in current studies has been modified from a uniform shearing flow code developed by Walton and Braun (6). Parts of the diagnostic procedure were modified by Dr. Hyeong-Jin Kim when he studied Couette flow (45). The recent modifications incorporated for this dissertation include imposing special boundary conditions and implementing new diagnostic parameters to calculate the velocity and temperature fields in different cases for the vibrating bed. Two independent codes have been written and tested to compute the autocorrelation function and mean square displacement, from which diffusion coefficients can be found.

Aftrer initial coordinates for particle centers are generated via a random number generator. radii expansion technique is used to determine an initial configuration for the system. Then all the initial and boundary conditions are superimposed to initialize the simulation. A finite difference algorithm developed by Verlet (48) is employed to solve the resulting equations of motion of the system of interacting spheres for particle translations and rotations and velocities. The time increment, usually called time step, is significantly smaller than the typical time taken for a collision to ensure a sufficient degree of accuracy. Long term diagnostic parameter calculations, including mean and fluctuation velocity, solids fraction, granular temperature and stresses, are computed after the system has reached steady state.

The computer simulation is performed on a three-dimensional control volume, consisting of a vibrating floor, periodic or solid side walls and an open top surface. First the particles are allowed to fall under the influence of gravity to get a loose packing, which is called the pouring procedure. Then the floor starts to shake to simulate a vibating bed.

There are 16 subroutines in the current simulation code, which can be classified into five groups according to their functions.

1. *Subroutines for simulation parameters input and initialization.*

   Simulation parameters include:

   - basic parameters (number of particles, diameter, computational cell size and maximum run time)
   - boundary parameters (number of boundary particles and their size)
   - material properties (coefficient of restitution, stiffness, friction coefficient, mass per unit sphere and gravity acceleration)
   - vibration parameters (velocity amplitude and frequency)

   These are specified in an input file (named **i3ds**), and then read in via subroutine **Datain**. The boundary particle configuration is obtained from subroutine **Bound**. After assigning indices for free and boundary particles, the initial positions and deviatoric velocities for particle centers are generated in subroutine **Init**. The time step and diagnostic zone parameters are also calculated there. The initial configuration of the system is completed in subroutine **Findrad** after finishing radii expansion.

2. *Interparticle force subroutine.*

   Subroutine **Forces** calculates the forces between all the interaction pairs within the near neighbor array, which is created and updated from time to time by the subroutine **Update**.

3. *Integration subroutines.*

   After subroutine **Initstep** initializes the integration step, subroutines **Integ1** and **Integ2** solve the equations of motion numerically, using the Verlet algorithm (48).

4. *Diagnostic calculation subroutines.*

   Subroutines **Initcum1** and **Initcum2** initialize the short and long term cumulative average parameters respectively, and then subroutine **Diagnos2** calculates all the diagnostic parameters, such as mean velocity, granular temperature and solids fraction.

5. *Data output subroutine.*

   Subroutine **Datasave** is responsible for writing the output data into specified files.

A flow chart of this simulation code can be found in (45).

Some important strategies used in particle dynamics simulation will be introduced later in this chapter, with emphasis on the detailed methods employed in this simulation. Topics included in H. Kim's dissertation (45), such as the Verlet algorithm and linked-list logic are not discussed.

2.2 Generating An Initial Configuration

After the input data is read in, a set of random coordinates, if not contradicting boundary conditions, is assigned to the center of each particle in subroutine **Init**. However the diameter of each sphere is not yet defined. This is done in subroutine **Findrad**, which is called to find an allowable radius for each particle. For example, the radius of particle i is set equals to a fraction of the distance r_{ij} between i and its nearest neighbor j such that these two particles share this distance according to the ratio of their pre-input radius values. (See Figure 2.1) Suppose k, m and n have specified the same input radius in input file **i3ds**, and particle k's nearest neighbor is particle m, but particles m and n can claim each other as nearest neighbors. Therefore particles m and n are assigned same radius, which equals half of distance r_{nm} between them, and they just tangentially touch each other. But particle k has a radius equal to $1/2\ r_{km}$, which is larger than those of particles m and n. If the radius of a particle, decided as explained above, exceeds the specified input value, the code simply sets it equal to this input value. After all the particles have been assigned an allowable radii, those particles, having radii less than the input value, will increase their radii at a constant rate at each time step in subroutine **Findrad**. This causes interactive forces between overlaping particles, which are computed in subroutine **Forces**.

The subsequent motions are determined in subroutines **Integ1** and **Integ2**. The radius expansion procedure does not stop until each particle has the radius specified in the input file **i3ds**. In summary, the function of subroutine **Findrad** is to obtain an initial configuration by means of radius expansion.

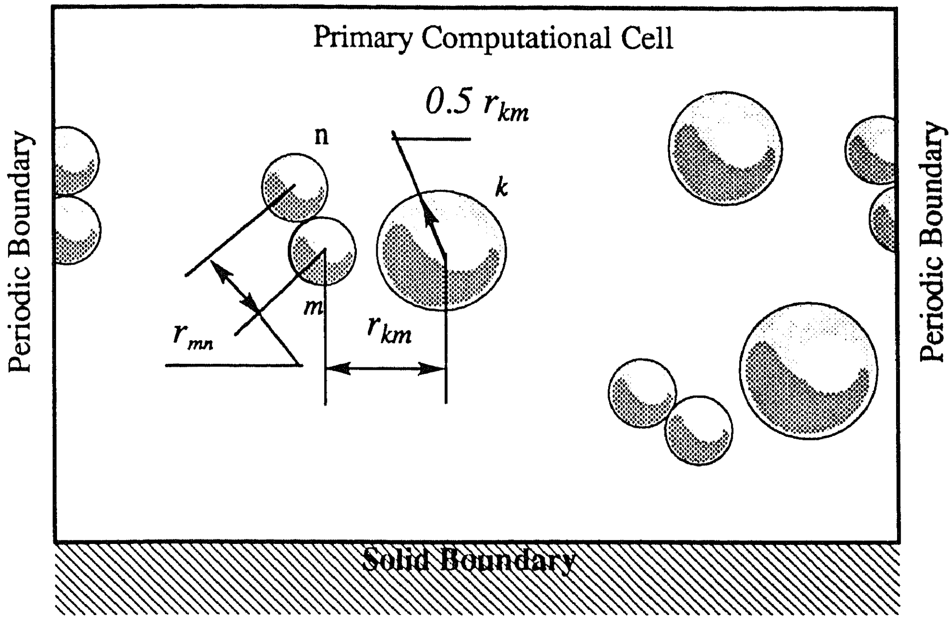

Figure 2.1 Allowable radius when nearest neighbor is considered.

2.3 Neighbor Lists and Updating

In order to evaluate of interparticle forces between particles and to permit efficient searching for contacts, a data structure called "neighbor lists" is used. Instead of looping over all particles in the cell to find contacts, the argorithm examines only the near neighbors around particle *i*, when considering the interaction between particle *i* and other particles. The near neighbors of a particle are defined by a parameter, called "search" in the code. Particle *j* will be on the neighbor list of particle *i* only if the separation distance r_{ij} between their centers is less than a distance equal to the radius of *i* plus the value of parameter "search". A list of all the neighbors of each particle is constructed and updated by the code at update time. During the updating intervals, the program checks only those particles appearing in the list, and then calculates the forces. The neighbor lists are stored in a large array, which contains not only the particle number, but also the latest tangential force history and overlap information. A pointer is used to indicate the position in the neighbor list array where the first neighbor of particle *i* can be found.

At the beginning of the program, the "search" distance is either input or set to its default value of the maximum particle radius. The initial update interval is directly proportional to the search distance and inversely proportional to the maximum initial root mean square (rms) deviatoric velocity, if the later is nonzero. Otherwise the initial update interval is set to be 20 time steps. A value of 200 time steps is set in subroutine **Init** as the maximum update interval.

The function of the **Update** subroutine is to construct and update the neighbor list. First, the routine checks for particle *i* each particle pair (*i*, *j*) to ascertain if the center of *j* lies within the search region. For those inside this region, it will further check if particle *j* is already in the previous neighbor list of particle *i*. The algorithm skips those in this previous list, while it adds each not included at the end of the list. If particle *i* has no previous neighbor list, particle *j* within the search region will be added as the first entry of particle *i*'s neighbor list.

The subroutine **Forces** loops over the neighbor list and uses the information stored for each particle, together with the current information about positions of particle, to calculate the new forces. At the same time the updated information is recorded on the new list.

The update interval is subject to change during simulation, although it had already been set in subroutine **Init**. Each time after subroutine **Update** finishes updating the list, the next update time will be recalculated from the search distance and the maximum root mean square deviatoric velocity from the last time step. Between update intervals, the ratio of search distance to the current maximum deviatoric velocity is continuously monitored by the subroutine **Diagnos2.** If the ratio is smaller than half of the value computed during the last call to the routine, the update time will be revised by this small ratio. In all cases the update interval will not be less than a time step or larger than a maximum update interval.

The neighbor lists method saves significant cpu time by looping over only a fraction of the particles instead of all particles in searching for contacts and calculating the forces. However in some particular cases, if one of the particles moves so fast that it penetrates into or through the search circle, errors may occur (Figure 2.2).

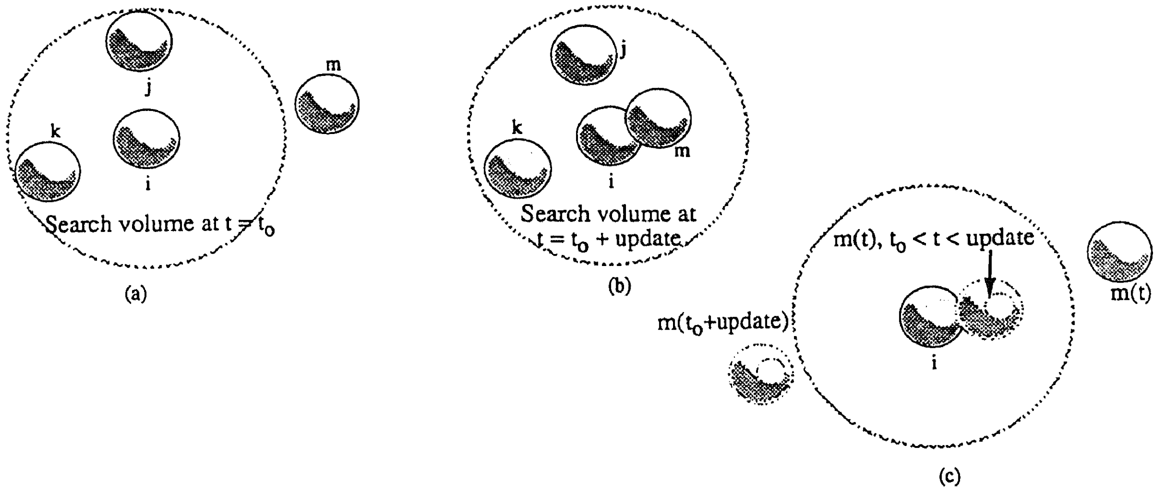

Figure 2.2 Errors occurred during the update interval.

For example, suppose particle *m* was outside of search circle of particle *i* at the update time t_0 (Figure 2.2a). During the update interval, particle *m* had not only moved inside the circle, but also impacted against particle *i* with a overlap when the next update time arrived (Figure 2.2b). An error occurred since the **forces** subroutine only calculated the particle interactive forces between the contacting pairs inside the search circle at the last update time. Particle *m* had come into contact with particle *i* during the update interval, but subroutine **Forces** failed to calculate the interactions between them, and hence nothing was recorded on the neighbor list. In this case, the code outputs an error message and then exits. An error will not be detected if particle *m* penetrates through particle *i* and consequently separates during the update interval (Figure 2.2c). Due to neglect of interactive forces by the code, particle *m* moves without any resistance, as if it never collides with particle *i*. During the course of the research reported in this dissertation, it was observed that when velocities were "too large," some particles passed right through the solid boundaries without being detected. Circumventing this error is a complex issue and it depends on the update time, search radius and particle velocities and diameters. This error occurs in general during the pouring stage of a simulation when it is possible for a particle which has a large mean free path to develop a high impact velocity Large mean free paths are prevalent when the computational cell is of a height substantially larger than the particle diameter.

The parameter "search" is a user input. As search distance is increased, the frequency of updates of the neighbor list will be decreased. However more particles will be included in the neighbor list, and this decreases efficiency. It was also observed that by increasing the value of "search", the above noted error is not eliminated, since as "search" is increased, the update time is decreased proportionally.

2.4 Collisional Force Model

In this study, a hysteretic force-displacement soft particle contact model, developed by Walton et al. (6), is used to simulate the collisions between the particles in a vibrating bed, where continuous and multiple contacts are expected to occur.

An overlap after initial contact between particles is interpreted as the deformation which generates a normal repulsive force. To estimate the value of this force, the model distinguishes a compression period (loading) from restitution period (unloading) during a single collision by using a different stiffness for the loading and unloading process. The tangential force, which approximates the Mindlin-Deresiewicz model (49), is calculated at each time step incrementally from the old value of tangential force, together with the tangential stiffness and relative surface displacement between particles at the point of contact. The details of the Walton and Braun models can be found in (6, 50). They are repeated here for completeness.

2.4.1 Normal Force Model and Normal Restitution Coefficient

The elastic collision of two spheres is divided into two periods. The first is the "compression period" (or loading period), during which elastic deformations of the spheres occur after initial contact. The degree of deformation is measured by the normal overlap between the spheres. The compression period ends as the relative velocity is reduced to zero, and the overlap has reached a maximum value. This is followed by the "restitution" or unloading period when the overlap decreases. At the end of restitution period when the spheres separate, the two particles either will have regained their original shape or will have some residual deformation before loading again. No permanent deformation of the spheres is permitted and if the particle does not suffer another collision during the unloading period , the residual α_0 is set to zero for the next collision.

Figure 2.3a is a schematic representation of the force model, which was termed the "partially latching-spring" model by Walton and Braun (6).

The normal force (F_1 or F_2) is expressed as

$$\begin{aligned} &F_1 = K_1 \cdot \alpha && \text{for loading, and} \\ &F_2 = K_2 \cdot (\alpha - \alpha_o) && \text{for unloading, or reloading from nonzero overlap,} \end{aligned} \qquad (2\text{-}4\text{-}1)$$

where K_1 and K_2 are two different spring stiffnesses, shown as the slopes of the curves in Figure 2.3b. Here α is the current overlap and α_0 is the overlap value where the unloading curve goes to zero along the slope K_2. In this model, the initial loading follows the slope K_1 from point *a* to *b*. If unloading occurs at point *b*, it will take place along a the steeper slope of K_2 from point *b* to *c*, until the normal force is reduced to zero with a remaining overlap α_0. Reloading from any point between *b* and *c* will follow the path *c-b-d*.

Unloading from a different point *d* will be along a different path but at the same slope of K_2.

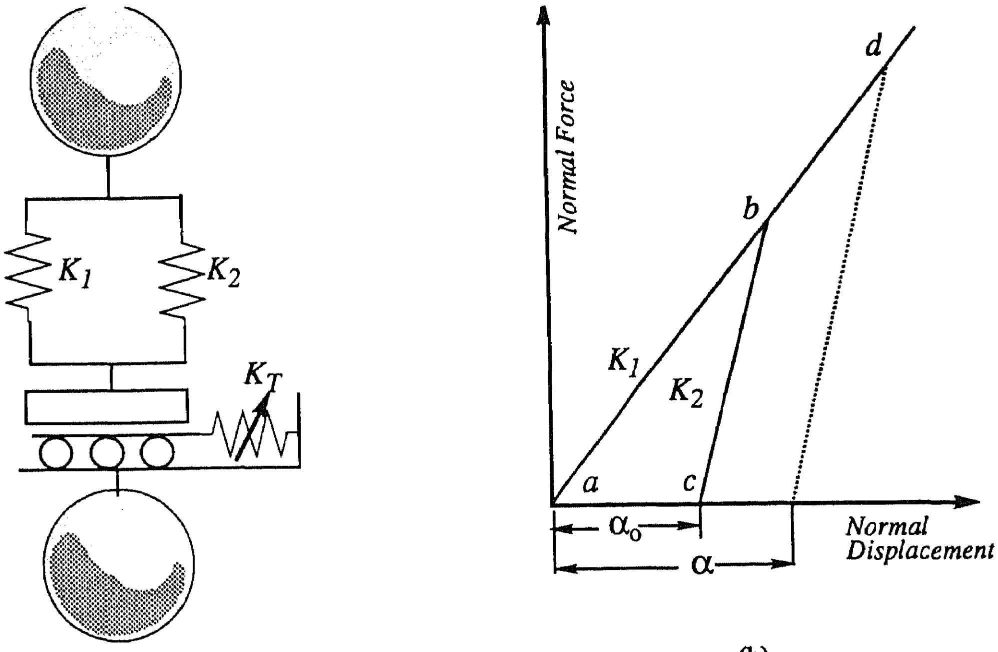

(a)

(b)

Figure 2.3 (a)Model of partially latching-spring (6) for collision interaction and (b) linear normal force loading and unloading with stiffnesses K_1 and K_2, respectively.

During the simulation, the code calculates the value of F_1 and F_2 values at each time step, and chooses the smaller one to be the normal force between the particles, which results in the loading, unloading and reloading paths as described above. A detailed explanation is as follows.

1. Loading from zero remaining overlap ($\alpha_0 = 0$) (Figure 2.4 a):

   Since $K_1 < K_2$, it is clear that

   $$F_1 = K_1 \cdot \alpha < K_2 \cdot (\alpha - 0) = F_2.$$

   therefore, F_1 will be used as the normal force in this case, which means loading follows the path having a smaller slope K_1.

2. Unloading :

   Unloading from point b will follow the path *b-c* (Figure 2.4b). Here F_2 will always be smaller than F_1.

3. Reloading from $\alpha_o \neq 0$:

   From Figure 2.4c, it is clear that $F_2 < F_1$ when reloading from *c* to *b*. Choosing F_2 as the normal force is the equivalent to reloading along path *c-b* (slope K_2). After reaching point *b*, $\overline{F_2}$ will be larger than $\overline{F_1}$. So $\overline{F_1}$ will be used as the normal force, ensuring further loading along *b* to *d*.

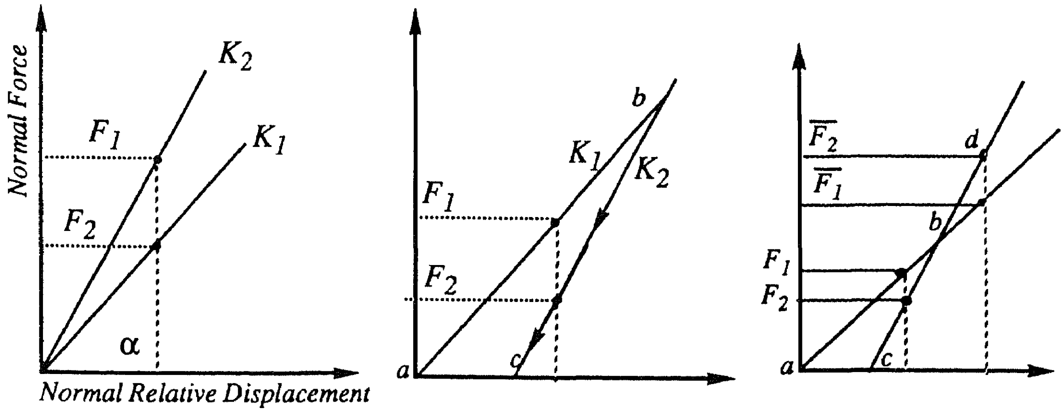

(a) (b) (c)

Figure 2.4 Procedure for normal force loading (a), unloading (b) and reloading (c)

Although the normal force model discussed above is a simple empirical model, Walton and Braun (6) had shown that it can effectively approximate the behavior observed in experiments and finite element calculations (50). In this study, this model has been used to simulate the behavior of vibrating beds. Results compared with experimental data also demonstrate the effectness of this model.

The normal coefficient of restitution *e* derived from the above force model proceeds as follows. Consider the impact of two spheres approaching along the line joining the centers of the spheres. The normal interaction force F_1 begins to act and change the velocities of the spheres after their initial contact. Suppose v_1 and v_2 are the value of these velocities, m_1 and m_2 sphere masses; then the equations of motion are,

$$m_1\cdot\frac{dv_1}{dt}=-F_1 \qquad\qquad m_2\cdot\frac{dv_2}{dt}=-F_1 \tag{2-4-2}$$

Hence, the relative velocity of approach $\dot{\alpha}$ is,

$$\dot{\alpha}=v_1+v_2 \tag{2-4-3}$$

From (2-4-1) , (2-4-2) and (2-4-3), the acceleration of approach can be expressed as,

$$\ddot{\alpha}=-K_1\alpha\cdot\frac{m_1+m_2}{m_1\cdot m_2} \tag{2-4-4}$$

Upon multiplying both sides of (2-4-4) by $\dot{\alpha}$ and using the notation $\mu=\frac{m_1\cdot m_2}{m_1+m_2}$

$$\tfrac{1}{2}d(\dot{\alpha})^2=-\frac{K_1}{\mu}\alpha\cdot d\alpha \tag{2-4-5}$$

Let v_a be the approach velocity when α = 0 and α_m be the maximum deformation when $\dot{\alpha}$ = 0.

Integrating of (2-4-5) yields,

$$\frac{1}{2}\dot{\alpha}^2\Big|_{\dot{\alpha}=v_a}^{\dot{\alpha}=0}=-\frac{K_1}{2\mu}\Big|_{\alpha=0}^{\alpha=\alpha_m}\Rightarrow v_a=\alpha_m\cdot\sqrt{\frac{K_1}{\mu}} \tag{2-4-6}$$

Next consider the equation of motion for unloading period when the spheres are separating under the force F_2. Then,

$$m_1\cdot\frac{dv_1}{dt}=F_2 \qquad\qquad m_2\cdot\frac{dv_2}{dt}=F_2 \tag{2-4-7}$$

The relative approach velocity $\dot{\alpha}$ is given by $\dot{\alpha}=-(v_1+v_2)$, and $F_2=K_2\cdot(\alpha-\alpha_0)$. By following the same procedure as above, we have,

$$\frac{1}{2}\cdot d(\dot{\alpha}^2)=-\frac{K_2}{\mu}(\alpha-\alpha_0)\cdot d(\alpha-\alpha_0) \tag{2-4-8}$$

from which, by integration,

$$\frac{1}{2}\cdot\int_{\dot{\alpha}=v_s}^{\dot{\alpha}=0} d\left(\dot{\alpha}^2\right)=-\frac{K_2}{2\mu}\int_{\alpha=\alpha_0}^{\alpha=\alpha_m} d\left[(\alpha-\alpha_0)^2\right] \tag{2-4-9}$$

where the lower limit v_s is the relative velocity of separation of the two spheres when the interaction force is zero. It follows from (2-4-9) that,

$$v_s=\left(\alpha-\alpha_0\right)\sqrt{\frac{K_2}{\mu}} \tag{2-4-10}$$

Therefore, the effective coefficient of restitution e can be obtained from the definition,

$$e=\frac{v_s}{v_a}=\frac{\left(\alpha-\alpha_0\right)\sqrt{\frac{K_2}{\mu}}}{\alpha_m\sqrt{\frac{K_1}{\mu}}}=\frac{\left(\alpha-\alpha_0\right)}{\alpha_m}\sqrt{\frac{K_2}{K_1}} \tag{2-4-11}$$

Upon noting that the ratio $\frac{\alpha_m-\alpha_0}{\alpha_m}=\frac{F_2/K_2}{F_2/K_1}=\frac{K_1}{K_2}$ is independent of the past loading history, we find a constant of coefficient restitution,

$$e=\sqrt{\frac{K_1}{K_2}}. \tag{2-4-12}$$

2.4.2 Tangential Force Model

The tangential force model used in this study is patterned after the theorectical model developed by Mindin and Deresiewicz (49), who proposed to use a tangential stiffness which decreases with the tangential displacement until full sliding occurs.

The tangential force between two interacting spheres is the component on the tangential plane which is perpendicular to the vector pointing from one sphere center to the other. As the position of spheres change, the tangential plane also changes. The following discussion is based on a coordinate system fixed to the tangential plane between two interacting spheres at the previous time step (t-Δt).

The force due to relative surface slip at time *t* between particles *i* and *j*, denoted by **ftij**, is calculated from the previous value (at t-Δt) of the tangential force, **tf**, by considering the adjustment caused by the relative surface displacement ΔS, namely,

$$\mathbf{ftij} = \mathbf{tp} + K_t \cdot (\Delta S_t) + K_o \cdot (\Delta S_n) \qquad (2\text{-}4\text{-}13)$$

where **tp** is a vector lying in the tangential plane (at time *t*) whose magnitude is obtained from the projection of **tf** onto this plane (Figure 2.5). It is important to note that **tf** shown in the figure does not lie in the tangent plane at time t, since this plane has moved during Δt. Here K_t is the effective tangential stiffness, K_o is the initial tangential stiffness, ΔS_t and ΔS_n are the components of ΔS in the tangential and normal directions of the tangential plane at time *t*, respectively (Figure 2.6). Therefore, $K_t \cdot (\Delta S_t)$ and $K_o \cdot (\Delta S_n)$ represent the tangential forces due to the relative surface displacement.

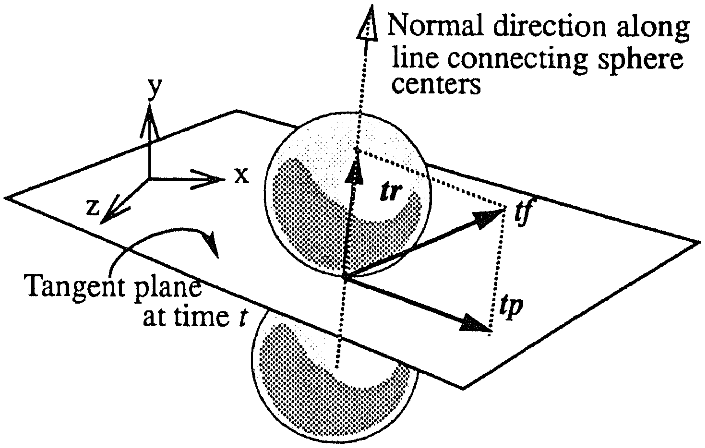

Figure 2.5 Collision of two spheres at time *t*. Here **tf** is the interaction from the tangential force model at thie *t* - Δ *t*, and **tp** and **tr** are its projection into the tangent plane and normal direction as shown.

In rectangular component form, equation (2-4-13) for the force **ftij** (ftijx, ftijy, ftijz) is given by,

$$ftijx = txp + Kt \cdot (\Delta S_t)_x + K_0 \cdot (\Delta S_n)_x$$

$$ftijy = typ + Kt \cdot (\Delta S_t)_y + K_0 \cdot (\Delta S_n)_y \qquad (2\text{-}4\text{-}14)$$

$$ftijy = tzp + Kt \cdot (\Delta S_t)_z + K_0 \cdot (\Delta S_n)_z$$

where *txp, typ* and *tzp* are the components of **tp** in the *x,y* and *z* directions, respectively.

The friction force **tf** calculated at the last time step (at t-Δt) is not in the current tangential plane (Figure 2.5), while the effective part for the current time *t* is its tangential component **tp** in the current tangential plane. The rectangular components *txp*, *typ* and *tzp* of **tp** can be calculated from the rectangular components *tfx*, *tfy* and *tfz* of **tf** by resolving **tf** into tangential component **tp** (*txp, typ, tzp*) and normal component **tr** (*trx, try, trz*). It is clear that **tp** may be written as,

$$\mathbf{tp} = \mathbf{tf} - \mathbf{tr} \qquad (2\text{-}4\text{-}15)$$

By making use of

$$\begin{pmatrix} trx \\ try \\ trz \end{pmatrix} = \begin{pmatrix} xk & yk & zk \end{pmatrix} \begin{pmatrix} tfx \\ tfy \\ tfz \end{pmatrix} \begin{pmatrix} xk \\ yk \\ zk \end{pmatrix},$$

where (*xk yk zk*) are the direction cosines of current tangential plane, equation (2-4-15) can be written in rectangular component form as,

$$\begin{pmatrix} txp \\ typ \\ tzp \end{pmatrix} = \begin{pmatrix} tfx \\ tfy \\ tfz \end{pmatrix} - \begin{pmatrix} xk & yk & zk \end{pmatrix} \begin{pmatrix} tfx \\ tfy \\ tfz \end{pmatrix} \begin{pmatrix} xk \\ yk \\ zk \end{pmatrix} \qquad (2\text{-}4\text{-}16)$$

The values of *tfx*, *tfy* and *tfz* are known from the neighbor list, and *xk*, *yk* and *zk* are calculated from the current particle position.

The relative surface displacement ΔS (*dsx dsy dsz*) contains two parts (Figure 2.6) One is the contribution due to the translation of the particles, the other is the contribution due to the relative rotation, which depends on the angular velocities of both particles. The tangential component ΔS_t is obtained simply by projecting ΔS (*dsx dsy dsz*) onto the current tangential plane, yielding

$$\begin{pmatrix} (\Delta S_t)_x \\ (\Delta S_t)_y \\ (\Delta S_t)_z \end{pmatrix} = \begin{pmatrix} t_x & t_y & t_z \end{pmatrix} \begin{pmatrix} dsx \\ dsy \\ dsz \end{pmatrix} \begin{pmatrix} tx \\ ty \\ tz \end{pmatrix} \qquad (2\text{-}4\text{-}17)$$

where (*tx ty tz*) are the direction cosines of the unit vector in the current tangential plane, given by $\frac{\mathbf{tf}}{|\mathbf{tf}|}$

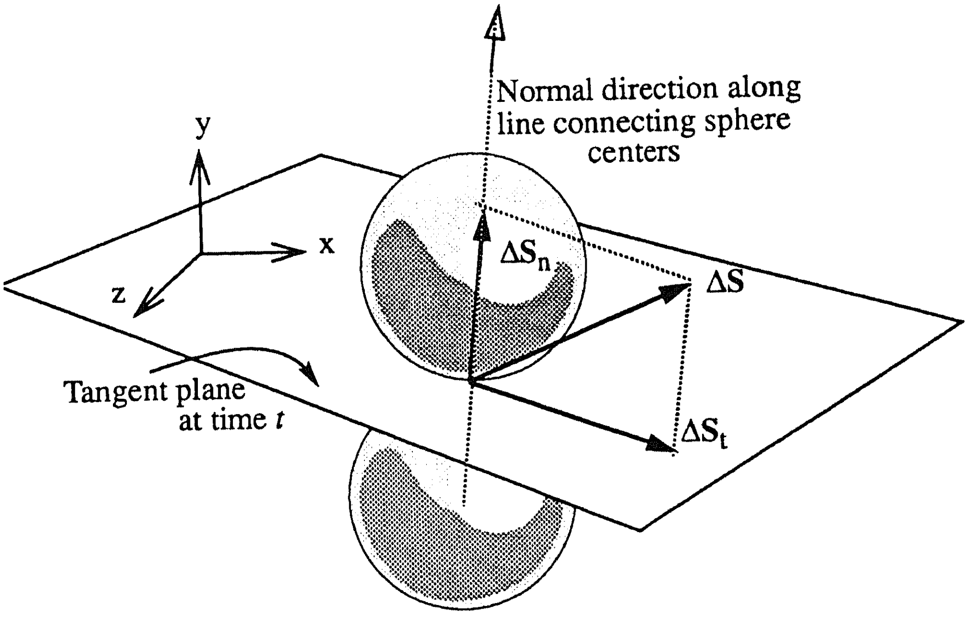

Figure 2.6 Relative surface displacement ΔS at time (t - Δ t) of two interaction spheres and its projection onto the tangent plane ΔS_t and normal direction ΔS_n at time t.

Once ΔS_t has been obtained, ΔS_n (*dsxp dsyp dszp*) is straightforward to compute by vector subtraction,

$$\Delta S_n = \Delta S - \Delta S_t \tag{2-4-18}$$

which in component form is given by,

$$\begin{pmatrix} dsxp \\ dsyp \\ dszp \end{pmatrix} = \begin{pmatrix} dsx \\ dsy \\ dsz \end{pmatrix} - \begin{pmatrix} tx & ty & tz \end{pmatrix} \begin{pmatrix} dsx \\ dsy \\ dsz \end{pmatrix} \begin{pmatrix} tx \\ ty \\ tz \end{pmatrix}. \tag{2-4-19}$$

The stiffness values used for the two components of ΔS are different. Since slip cannot occur in the direction along the line of centers of the spheres, the initial tangential stiffness K_0 is fixed and defined as $K_1 \cdot ratk$, where K_1 is normal stiffness and *ratk* is an input ratio. However, the effective tangential stiffness K_t in this model is a variable, related to the Coulomb friction limiting value and the direction of the total tangential force. To evaluate the potential sliding in the two directions, the code introduces a factor *scalek* to express K_t, namely,

$$K_t = K_0 \cdot scalek \tag{2-4-20}$$

where *scalek* is given by

$$scalek = \left(1 - \frac{T - T^*}{\mu N \pm T^*}\right)^{1/3} \tag{2-4-21}$$

Here, μN is the maximum Coulomb friction force, T is the smaller value of the old friction force **tf** and μN, T^* is a variable, which is initially zero and subsequently set to the value of T, whenever the slip reverses direction. The sign of T^* is also decided by the slip direction.

2.5 Time Step and Material Properties

The proper selection of a time step and material properties, such as the loading stiffness, particle densities and normal restitution coefficient, is essential to make effective comparisons between the simulations and physical experiments. In making such a comparison, it is preferable to use realistic properties. However, this has the disadvantage of sigificantly increasing computing time. The cpu time depends on the time step, which is generally specified by the force model and is closely related to the choice of particle material properties. The use of a relatively larger time step than that determined from realistic material properties can save significant computing time, but results in some loss of accuracy in intergration of the system of equations. The balance of these two aspects is very important.

The time step used in this study is derived from the normal force model by considering the time spent in the restitution (unloading) period during a particle collision.

Consider the general integration of (2-4-8)

$$\frac{1}{2}\cdot\int_{\dot{\alpha}=0}^{\dot{\alpha}=\dot{\alpha}} d\left(\dot{\alpha}^2\right) = -\frac{K_2}{2\mu}\int_{\alpha=\alpha}^{\alpha=\alpha_m} d\left[\left(\alpha-\alpha_0\right)^2\right]$$

namely,

$$\frac{d\alpha}{dt}=\dot{\alpha}=\sqrt{\frac{K_2}{\mu}}\sqrt{\left(\alpha_m-\alpha_0\right)^2-\left(\alpha-\alpha_0\right)^2} \qquad (2\text{-}5\text{-}1)$$

This gives a restitution time *tr*,

$$\begin{aligned} t_r &= \int_{\alpha_0}^{\alpha_m}\frac{d\left(\alpha-\alpha_0\right)}{\sqrt{\frac{K_2}{\mu}}\cdot\sqrt{\left(\alpha_m-\alpha_0\right)^2-\left(\alpha-\alpha_0\right)^2}} \\ &= \sqrt{\frac{\mu}{K_2}}\cdot\arcsin\frac{\alpha-\alpha_0}{\alpha-\alpha_m}=\frac{\pi}{2}\sqrt{\frac{\mu}{K_2}} \end{aligned} \qquad (2\text{-}5\text{-}2)$$

For a monodisperse system of particles (i.e., uniform density and size) the reduced mass μ becomes *m/2;* hence it follows from (2-4-12) that,

$$t_r = \frac{\pi}{2}\sqrt{\frac{m}{2K_2}} = \frac{\pi}{2}\cdot e\cdot\sqrt{\frac{m}{2K_1}} \qquad (2\text{-}5\text{-}3)$$

In the actual simulation code, the duration of the impact is approximated as $2t_r$ We note that the time spent in restitution compared to compression has not been monitored and that the use of $2t_r$ is merely an estimate. Then time step Δt using in the simulation is determined by dividing t_r into n intervals, i.e.,

$$\Delta t = \left(\frac{\pi\cdot e}{n}\right)\cdot\sqrt{\frac{m}{2K_1}} = \left(\frac{\pi\cdot e}{n}\right)\cdot\sqrt{\frac{\pi d^3\cdot\rho}{12\cdot K_1}} \qquad (2\text{-}5\text{-}4)$$

where d is the diameter of particle, ρ is the density of the material. The value of n is input by the user. Equation (2-5-4) shows that the time step is dependent on the material properties e, n, K_1, ρ and the sphere diameter.

From (2-5-4), it is clear that as n decreases, the value of time step increases, which means a higher computing efficiency but less accuracy. In this simulation, after testing several different values of n, it was found that values between 15 -30 gave good accuracy and efficiency. This was done by checking the results for various choices of n.

In general, the results are sensitive to the restitution coefficient e. Since it is usually very difficult to measure e correctly, comparisons with simulations are sometimes uncertain. In this study, a value of $e = 0.9$ is chosen to model glass or plastic material in most of cases studies except when discussing the effects of this parameter.

The normal stiffness K_1 is the most important factor affecting the time step in this force model, but it is not listed in any handbooks. A related parameter usually listed in the handbooks is Young's modulus E. Therefore, the relationship between stiffness K_1 and Young's modulus E in current force model is the key for estimating stiffness. However, to the author's knowledge, this relationship has not been reported for contact model employed in these studies. Therefore, an equivalent Hertz force model is used for estimation. Such an approach is reasonable since collisional deformation is less than one or two percent of the sphere diameter, and consequently Walton and Braun's partially latching spring model follows the Hertian 3/2 power model well.

The force-displacement relationship in Hertz contact model can be expressed as,

$$F = K_H \cdot \alpha^{3/2} = \frac{E\sqrt{d}}{3(1-\nu^2)}\alpha^{3/2} \tag{2-5-5}$$

where K_H is the stiffness, E is Young's modulus, ν is the Poison's ratio, d is the diameter of the particle, and α is the relative displacement or overlap after initial contact (50).

To find the an equivalence between the Hertz model and the spring-latching model, the maximum strain energies from these two models are equated. This means that the areas under the two force-displacement curves must be equal (Fig. 2.7). For the Hertz model, upon condidering (2-5-5), this maximum strain energy U_{max} is given by,

$$U_{\max} = \int_0^{\alpha_{\max}} F_H \cdot d\alpha = \int_0^{\alpha_{\max}} K_H \cdot \alpha^{3/2} \cdot d\alpha$$

$$= \frac{2}{5} K_H \cdot \alpha_{\max}^{5/2} = \frac{2 \cdot E\sqrt{d}}{15 \cdot (1-\nu^2)} \cdot \alpha_{\max}^{5/2} \tag{2-5-6}$$

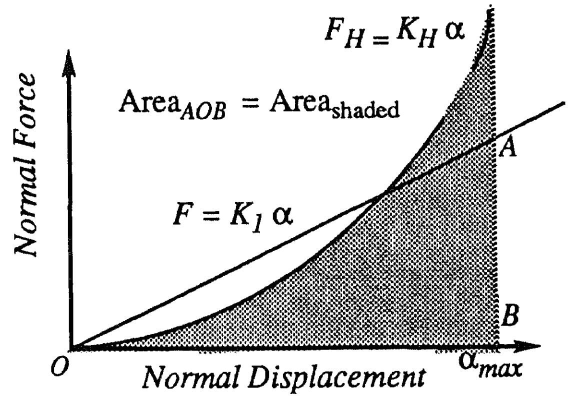

Figure 2.7 An equivalence between Hertz model and spring-latching model.

Suppose the maximun impact velocity between two spheres in a vibrating bed is determined by the maximum shaking velocity $v_{\max}$ of the vibrating floor. The kinetic energy of a particle whose velocity is $v_{\max}$ is given by,

$$U_{\max} = \frac{1}{2} m v^2_{\max} \tag{2-5-7}$$

where m is the particle mass. The maximum overlap $\alpha_{\max}$ is obtained by equating (2-5-6) and (2-5-7), i.e.,

$$\alpha_{\max} = \left[\frac{15 m v^2_{\max} \cdot \left(1 - \nu^2\right)}{4 \cdot E \sqrt{d}} \right]^{\frac{2}{5}} \tag{2-5-8}$$

From the spring-latching model, the work done is given by,

$$U_{\max} = \int_0^{\alpha_{\max}} F_1 \cdot d\alpha = \int_0^{\alpha_{\max}} K_1 \cdot \alpha \cdot d\alpha = \frac{1}{2} K_1 \alpha^2_{\max} \tag{2-5-9}$$

The loading stiffness K_1 is then approximated by equating (2-5-7) with (2-5-9), which yields, $K_1 = m \cdot \left(\frac{v_{\max}}{\alpha_{\max}} \right)^2$ .It is important to realize that this is merely an estimate and that $K1$ is in fact a material parameter.

The influence of normal stiffness K_1 on the computed granular temperature and solids fraction profiles has been carefully studied by making a comparison of two cases having different K_1 values with other properties being identical. The results of this comparison, which is discussed in Chapter 4, clearly indicated that the use of a normal stiffness value one hundred times smaller than that derived from the equivalent Hertz model, caused an insignificant difference in the computations. Recall from equation (2-5-4) that the time step Δt depends on the value of K_1. In order to reduce computing time, most of the simulations which are compared with real experiments and kinetic theory predictions employ the smaller normal stiffness value.

Besides material properties, the time step is considerablly influenced by the size of the particle. Particles smaller than 3 mm in diameter are usually used in experiments, but cause problems for use in simulation. For example, suppose one is modeling a granular flow of glass spheres of 3 mm in diameter. The time step (from equation (2-5-4)) will be of the order of 10^{-6} seconds, for glass spheres with density $\rho = 2490 \ {}^{kg}\!/_{cm^3}$, and Young's modulus $E = 6.8948 \times 10^{10} \ {}^{N}\!/_{m^2}$. For a small system of particles (*np* = 240), approximately 240 hours of CPU time on a Sun Sparc10 workstation was required to model a 40 second real time experiment.

2.6 Boundary Conditions

Once the interparticle forces are specified, only the boundary conditions and the initial conditions are required to completely solve the problem. Experiments and theoretical studies have shown that boundary conditions greatly influence observed bulk flow behavior (1, 42).

Due to dissipative interparticle collisions in granular material, external energy must be continually introduced into the system to maintain the granular temperature. Boundary shaking and shear work are two important methods to provide this energy. Vibrating or shearing walls may therefore be considered as a local source of temperature. On the other hand, collisions with the boundary, especially with a fixed wall, are also dissipating energy. From a kinematics point of view, a solid boundary is a kind of particular constraint acting on the system, which is quite different than periodic boundaries. For example, simulation results have shown that the presence of solid side walls is crucial for producing a convective motion in a vibrating bed.

In this simulation study, both the vibrating floor and side walls can be chosen to be smooth, or frictional and flat or bumpy. Figure 2.8 illustrates the computational cells and boundary conditions used in these studies.

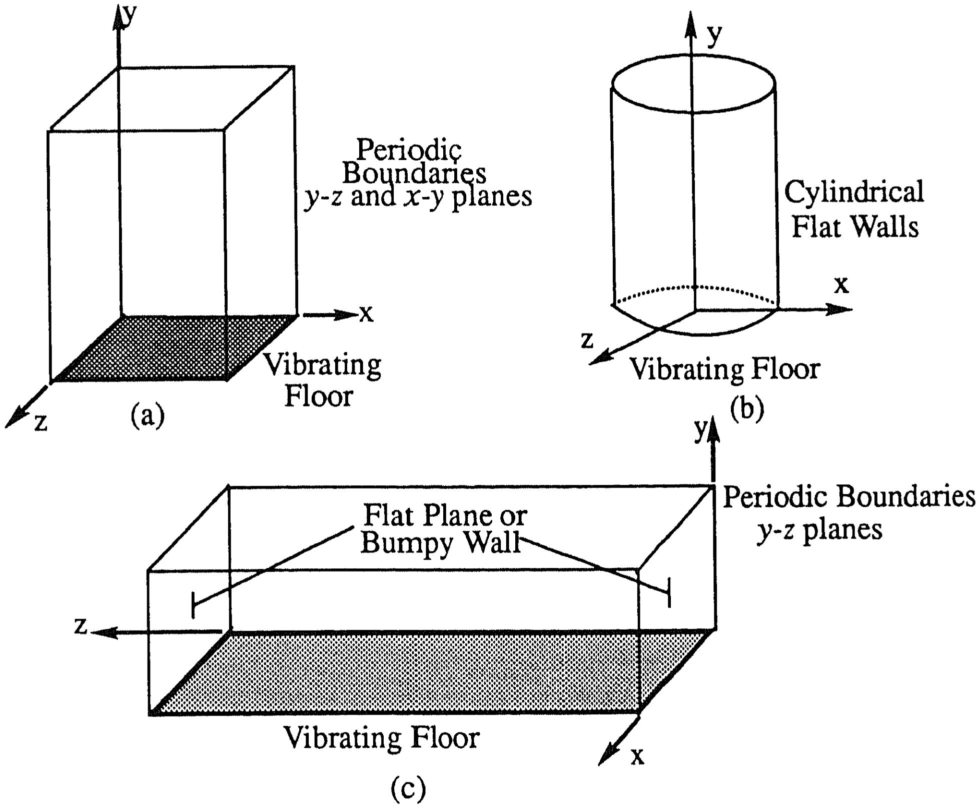

Figure 2.8 Computational cells and boundary conditions

2.6.1 Periodic Boundary Condition

Due to the limitation of storage and speed of the computer, particle dynamics simulations are usually performed on a small number of particles. If these particles are confined by the walls of a container, a large fraction of them will lie on the surface, where the particles experience quite different forces from those in the bulk. Periodic boundary conditions are to be preferred in most instances since they minimize these surface effects and preserve a macroscopic homogeneity. Also, the use of nonperiodic cells with small systems might preclude the occurrence of phenomena such as clustering (51), which takes place over a large length scale.

Instead of having a real confining wall, the periodic boundary condition is constructed by a primary cell and surrounding imaginary cells. Particles are originally in the primary cell, whose lengths in x, y and z direction are given by *xcell*, *ycell* and *zcell*, respectively. Each imaginary cell is a replica of the primary cell. For each particle having coordinates (x_p, y_p, z_p), there are an infinite number of images in the imaginary cells at position (x_i, y_i, z_i), where

$$\begin{cases} x_i = x_p + l \cdot xcell \\ y_i = y_p + m \cdot ycell \\ z_i = z_p + n \cdot zcell \end{cases} \quad (l,m,n \text{ are arbitrary positive or negative integers}) \qquad (2\text{-}6\text{-}1)$$

In the course of a simulation, as a particle in the primary cell moves, its image in each neighboring cell moves in exactly the same way. As a particle leaves the primary cell, one of its images will enter from the opposite side. Since there are no real walls, no surface effect exists.

A particle's real position can be inside or outside of the primary cell. Particle collisions can occur in variety of ways between particles' images or between the particle and other particles' images. An example is depicted in Figure 2.9, particles *I*, *J* and *K* are in three different cells. Here, particle *I* is colliding with the image of particle *K* outside of the primary cell, while particle *I*'s image in primary cell is just touching the image of particle *J*. Each time the program calculates the real distance between two particles to determine if collision has occured, it also checks the distance between one particle and other particle's image, as well as between the two images. Suppose $r_x = x(J) - x(I)$ is the real distance in the x direction between particle *I* and *J*, then the smallest distance between their images may be found by calculating a new r_x value, which is given by

$$r_x = r_x - xcell \cdot Int\left(r_x/_{xcell}\right) \qquad (2\text{-}6\text{-}2)$$

where r_x in left side of equation (2-6-2) is the new value of r_x , r_x in right side of (2-6-2) is the old value, and *Int* represents the integer conversion function.

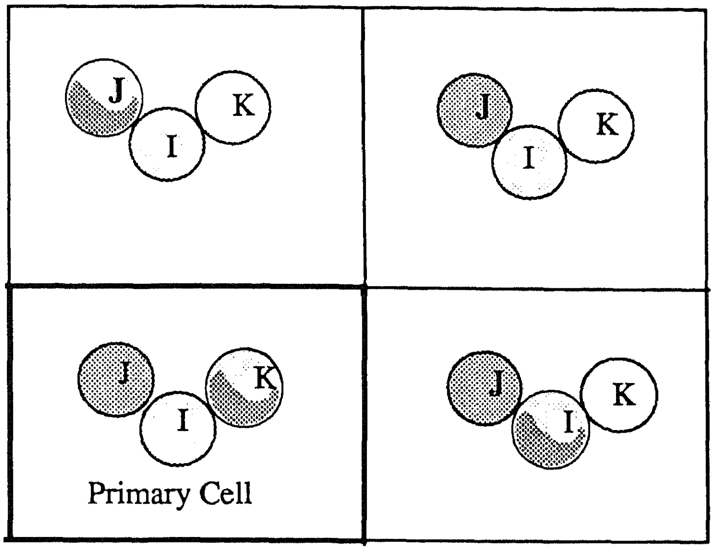

Figure 2.9 Collisions between particles and their images. Spheres depict the real particles

If *I* and *J* are in the same cell, $Int\left(rx/_{xcell}\right)$ will be zero since $r_x < xcell$. Therefore the value of r_x will not be changed. If *I* and *J* are in different cells, the new r_x value is given by equation (2-6-3). Similarly, the nearest image distance in the *y* and *z* directions is found by

$$r_y = r_y - ycell \cdot Int\left(r_y/_{ycell}\right) \qquad (2\text{-}6\text{-}4)$$

$$r_z = r_z - zcell \cdot Int\left(r_z/_{zcell}\right) \qquad (2\text{-}6\text{-}5)$$

In the vibrating bed case, the periodic boundary conditions are imposed only in the x and z directions. The solid vibrating floor is located at $y = 0$. Thus the nearest image distance checking in *y* - direction is not performed.

2.6.2 Plane Boundary

A plane boundary means that there is a solid plane to reflect the particles. A particle impacts this plane only when the distance from the center of the particle to the plane is just equal to or less than the radius of the particle. During the impact, the plane exerts a normal force and a tangential force on the particle (Figure 2.10)

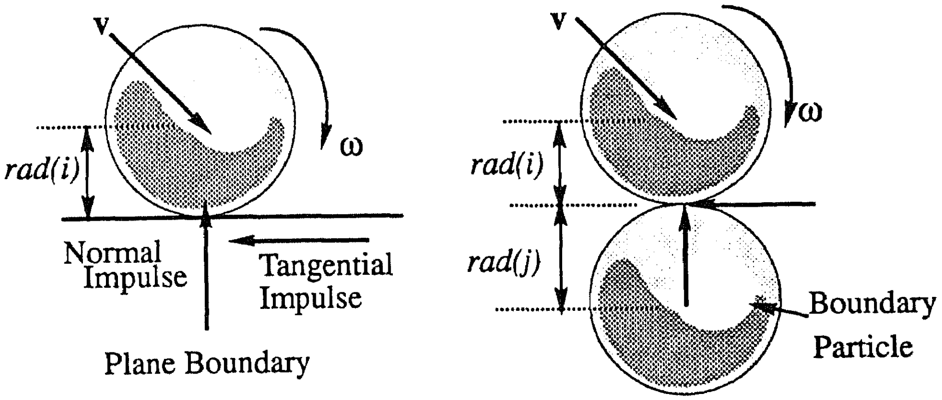

Figure 2.10 A plane boundary is modeled by a boundary particle of infinite mass

The solid plane is modeled by a sphere, which reflects an impacting free particle. It is noted that the solid plane sphere is unaffected by the impact and consequently maintains the same motion it had before impact. Suppose the plane boundary is located in the $y = 0$ plane. The center of corresponding boundary sphere j should be in the plane of $y = -rad(j)$, where $rad(j)$ is its radius. The x and z coordinates of the boundary particle are not specified. In order to find if particle i of radius $rad(i)$ hits the plane , the code only checks if the distance r_{ij} between the center of particle i and boundary particle j is equal to or less than the sum of their radii.

$$r_{ij}^2 = r_x^2 + r_y^2 + r_z^2 \leq \left[rad(i) + rad(j)\right]^2$$

where r_x , r_y and r_z are the x, y, and z coordinate differences between the center of the two spheres. For the previous example (plane at $y = 0$), r_x and r_z are always set to zero, which means the center of boundary particle has the same x and z coordinates as particle i. The only nonzero coordinate difference occurs in the y direction, i.e, r_y. The friction coefficient and restitution coefficient of the boundary particle can be input in **i3ds**. In this way the boundary particle can model a wall having various properties — smooth or frictional. (Figure 2.10)

2.6.3 Bumpy Boundary

Bumpy boundaries can be composed of identical, smooth or frictional half spheres. Two types of arrangements are currently available for use in this code, square arrangement or triangular arrangement. Details about these arrangements can be found in (45). It is important to check the spacing between the boundary particles in order to prevent free particles from passing through the gap. Overlap of boundary particles is not allowed, since the overlapped sphere volume will be counted twice when calculating the total volume of the cell and the zone (an equal portion of the cell).

2.6.4 Velocity of the Vibrating Floor

The initial velocity of a boundary particle is input by the user in the file **i3ds**. When a free particle collides with the boundary, only the free particle will experience change, while the particle representing the boundary remains unaffected as if it had infinite mass.

The velocity and displacement of vibrating floor is specified in subroutine **Integ2** after certain parameters (such as *tpour*, *frq* and *vamp)*, are read in by **Datain**.

Here, *tpour* is a parameter indicating the desired time for pouring, during which the velocity of the vibrating bottom is set to zero. After this is completed, the bottom starts to shake at a fixed frequency *frq*. The amplitude of vibrating velocity increases linearly from zero to the input value *vamp* in the first second of shaking, and then remains fixed. When a sinusoidal vibration is applied in vertical *y* direction, the floor velocity *v(y)* is given by

$$v(y) = vamp \cdot \cos(2\pi \cdot frq \cdot t) \qquad (2\text{-}6\text{-}6)$$

Shaking in three direction can be achieved by adding the other two velocity components, hence

$$\begin{aligned} v(x) &= vamp_x \cdot \cos(2\pi \cdot frq_x \cdot t + \varphi_x) \\ v(y) &= vamp_y \cdot \cos(2\pi \cdot frq_y \cdot t + \varphi_y) \qquad (2\text{-}6\text{-}7) \\ v(z) &= vamp_z \cdot \cos(2\pi \cdot frq_z \cdot t + \varphi_z) \end{aligned}$$

where φ_x, φ_y and φ_z are the initial phase angles.In the studies which are compared with theoretical predictions, the boundary is oscillated in three directions with equal phase angles of zero and equal frequencies and amplitudes.

2.6.5 How to Define a Boundary Condition

The number of boundary particles along each coordinate direction is specified in file **i3ds**. For example, *nybx0* and *nzbx0* are the number of boundary particles along *y* and *z* direction at the plane of $x = 0$, respectively. Setting both of them equal to zero implies periodic boundary condition at that plane. A plane boundary is created by setting *nybx0* = *nzbx0* = *1*. Any other number (except zero and one) for *nybx0* or *nzbx0* means a real bumpy boundary on plane $x = 0$. There are other analogous flags defined by subroutine **Datain**, each of which represents the number of boundary particles in a particular direction on a particular plane (eg., *nxbz1*,*nybz1*). If a flag is omitted, the code will set this flag to its default value of zero, which implies a periodic boundary.

CHAPTER 3

DIAGNOSTICS AND DATA ANALYSIS

The advantage the of dynamics simulations is to obtain a substantial amount of time-ordered information about individual particle's positions, velocities (including angular velocities) and forces. Methods to compute macroscopic or bulk properties, such as granular temperature, as well as time correlation functions, is the topic to be discussed in this chapter. In a dynamics simulation, it would be inappropriate to store every configuration on a disk or tape for further processing. Usually the bulk properties are obtained by taking appropriate weighted averages during the simulation. Calculation of time correlation functions are made after completing a simulation by post-processing stored data stored on disk.

3.1 Diagnostic Quantities and Averages

In order to examine the macroscopic properties in a granular flow, diagnostic parameters are computed by taking space and time averages of particle velocities and their fluctuations. These include mean and deviatoric velocities, mean kinetic energy density, granular temperature and solids fraction.

Two types of spatial average method are employed. One is the "global" or "computational cell" average, which is performed by considering the contribution of every particle in the system. The other, a "local" average taken over a portion of the computational cell, provides a means of examining spatial variations of diagnostic quantities. Depending on the relative size of the computational region over which averages are performed, it is possible to analyze details of the microstructure. In studies where periodic boundary conditions are applied in the directions perpendicular to the gravity field, the computational cell is partitioned into "zones" along its depth since properties should be uniform in the other directions. Generally a particle may occupy up to three zones, since each element of the partition of has a minimum height equal to the radius of the largest free (i.e., non-boundary and non-fixed) particle. An instantaneous zone diagnostic is a mass-weighted average taken over all the particles which occupy a zone at some time t. For example, in Figure 3.1, only the mass contained in the lower part of particle 1, the central portion of particle 2 and the upper segment of particle 3 (dark region) are counted when performing the average for zone y. Therefore, the instantaneous mean velocity in zone y is simply given by,

$$\mathbf{u}(y,t)=\frac{\sum_{i\in y}\hat{m}_i(t)\cdot\mathbf{v}_i(t)}{\sum_{i\in y}\hat{m}_i(t)} \tag{3-1-1}$$

where $\mathbf{v}_i(t)$ is the velocity of particle i, $\hat{m}_i(t)$ is the mass fraction of particle i in zone y, while $\sum_{i\in y}$ means the summation over all the particles occupying zone y. So the denominator of (3-1-1) is the total particle mass of zone y, while the numerator is its total momentum.

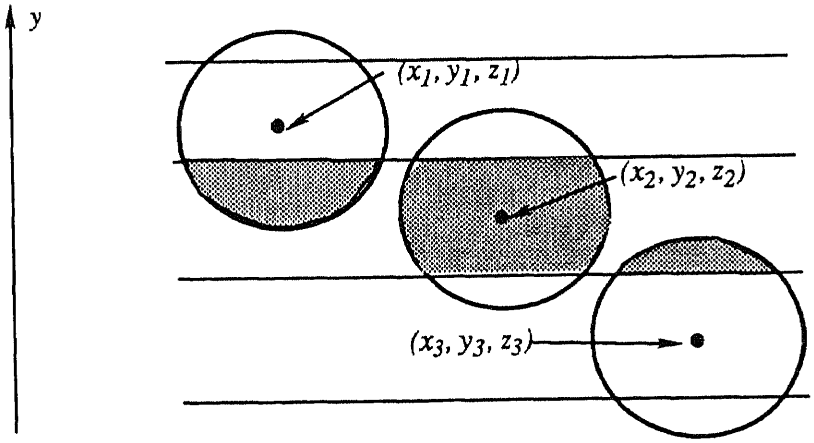

Figure 3.1 In computing mass-weighted averages of diagnostic quantities, only the tractional portion of the particle in the zone contributes to the average.

It is straightforward to express the instantaneous cell average mean velocity as

$$\mathbf{u}_{cell}(t) = \frac{\sum_{i \in cell} m(i) \cdot \mathbf{v}_i(t)}{\sum_{i \in cell} m(i)} \tag{3-1-2}$$

where *m(i)* is the mass of particle *i* and the summation is over all particles in the computational cell.

Time averages of the mass-weighted, instantaneous quantities are computed both as "short-term" or "long-term" values. Short term time averages are performed over time intervals specified by the user (i.e., usually *dtout*, a user-input parameter to specify when computed diagnostics will be written to the output files). The smallest time interval for computing short-term averages is the time step Δt (discussed in section 2.7). Although it is not practical to choose time step as the short term average interval, an interval of 7.5 times of time step has been frequently used in this study when spectral analysis is used to examine the change of zone average velocities. In a y-zone, the short term cumulative mean velocity can be expressed as

$$\langle \mathbf{u}(y,t) \rangle_s = \frac{\sum_{t \in dtout} \left(\sum_{i \in y} \hat{m}_i(t) \cdot \mathbf{v}_i(t) \right)}{\sum_{t \in dtout} \left(\sum_{i \in y} \hat{m}_i(t) \right)} \tag{3-1-3}$$

where the notation $\langle \ \rangle_s$ stands for the short term time average, and $\sum_{t \in dtout}$ represents the sum of the instantaneous values in the time interval *dtout*. Equation (3-1-3) is merely then a short-term, mass-weighted cumulative mean value.

The time interval over which to compute the long term cumulative average of instantaneous mass-weighted values, denoted by $\langle \ \rangle_L$, is a user input quantity. For this purpose, statistics are accumulated after the system has attained steady state. Long term cumulative average will be denoted by $\langle\ \rangle_L$ later. So it is straightforward to express long term cumulative mean velocity in zone y as,

$$\langle \mathbf{u}(y) \rangle_L = \frac{\sum_{t=t0}^{t\max}\left(\sum_{i\in y}\hat{m}_i(t)\cdot\mathbf{v}_i(t)\right)}{\sum_{t=t0}^{t\max}\left(\sum_{i\in y}\hat{m}_i(t)\right)} \qquad (3\text{-}1\text{-}4)$$

where the outer summations are taken from t = to (standing for "*tzero*") to "*tmax*", a flag for maximum time running simulation.

In this study, the short and long term cumulative mean velocities in different zones are calculated in rectangular component form and saved separately in the files named **zxvel** (for the *x* components), **zyvel** (for the *y* components) and **zzvel** (for the *z* components).

The space-time averages of other diagnostic parameters are defined and computed in a manner analogous to equations (3-1-1), (3-1-3) and (3-1-4).

The deviatoric velocity of a particle, commonly referred to as the fluctuating part of velocity, is found by subtracting the mean velocity from the particle's absolute velocity. Hence, the instantaneous deviatoric velocity $\mathbf{C}_i(t)$ for particle *i* in zone *y* is expressed as,

$$\mathbf{C}_i(t) = \mathbf{v}_i(t) - \mathbf{u}(y,t) \qquad (3\text{-}1\text{-}5)$$

where **u**(y,t) is given by (3-1-1).

A parameter extensively used in statistical physics is the root-mean-square (rms) deviatoric velocity, whose *y*-zone mass-weighted average at time *t* is calculated as,

$$\mathbf{C}(y,t) = \left(\frac{\sum_{i\in y}\hat{m}_i(t)\cdot\mathbf{C}_i(t)^2}{\sum_{i\in y}\hat{m}_i(t)}\right)^{1/2} \qquad (3\text{-}1\text{-}6)$$

where the mass-weighted average is taken over the square of deviatoric velocity $C_i(t)$, given by (3-1-5), for all the particles occupying zone *y* at time *t*. The long term cumulative mass-weighted average of the rms deviatoric velocity is computed after steady state is attained at time $t = t_o$ over a time interval $(t_{max} - t_o)$ and is given by,

$$\langle \mathbf{C}(y,t)\rangle_L = \left(\frac{\sum_{t=t0}^{t\max} \left(\sum_{i\in y} \hat{m}_i(t)\cdot(\mathbf{v}_i(t)-\mathbf{u}(y,t))^2 \right)}{\sum_{t=t0}^{t\max} \left(\sum_{i\in y} \hat{m}_i(t) \right)} \right)^{1/2} \tag{3-1-7}$$

In the code, the short and long term rms deviatoric velocity values for different zones are saved in the file **zpadel** in subroutine **Datasave**.

A particularly important quantity to characterize the bulk behavior is the "granular temperature" — a term first used by Ogawa(38) twenty six years ago. From the kinetic theory point of view, the random motion of granular particles has an obvious analogy with the thermal motion of molecules in liquids and gases. Similar to the definition of temperature in thermodynamics, granular temperature, denoted by T, has been defined as a measure of the kinetic energy of the granular mass due to the particles' fluctuating velocities. It is commonly referred to as the "translational fluctuation energy per unit mass" and is defined by,

$$\frac{3}{2}\cdot T = \frac{1}{2}\cdot\langle \mathbf{C}(y,t)\rangle^2. \tag{3-1-8}$$

By using the the above notation, long term cumulative mass-weighted average granular temperature $T(y)$ (of zone y) is computed as,

$$T(y) = \frac{1}{3}\cdot(\langle \mathbf{C}(y,t)\rangle_L)^2 = \frac{1}{3}\frac{\sum_{t=to}^{t\max} \left(\sum_{i\in y} \hat{m}_i(t)\cdot(\mathbf{v}_i(t)-\mathbf{u}(y,t))^2 \right)}{\sum_{t=to}^{t\max} \left(\sum_{i\in y} \hat{m}_i(t) \right)} \tag{3-1-9}$$

In addition to the above, the mean translational kinetic energy density KE and solids fraction ν are monitored at each time step and averaged over short and long term periods. The long term mean of *KE,* which measures the translational kinetic energy per unit volume, is computed as,

$$KE(y)=\frac{\sum\limits_{t=to}^{t\max}\left(\frac{1}{2}\sum\limits_{i\in y}\hat{m}_i(t)\cdot(\mathbf{v}(t)-\mathbf{u}(y,t))^2\right)}{\sum\limits_{t=to}^{t\max}Vol(y)} \qquad (3\text{-}1\text{-}10)$$

where $Vol(y)$ is the volume of zone y. The long term cumulative average of the solids fraction $\nu(y)$ is given by,

$$\nu(y)=\frac{\sum\limits_{t=to}^{t\max}\left(\sum\limits_{i\in y}vol_y(i)\right)}{\sum\limits_{t=to}^{t\max}Vol(y)} \qquad (3\text{-}1\text{-}11)$$

where $vol_y(i)$ is the volume of particle i in zone y.

3.2 Spectral Analysis and Time Correlation Functions

A powerful technique to analyze random phenomena is through spectral analysis, which is done using Fast Fourier Transforms (FFT). In this work, power spectral density of the velocity field history is used to reveal the frequency composition of this time function. Intensity peaks at certain frequencies indicate the energy level distribution in the frequency domain. A white noise type record will have a broad spectral density function, while the spectral density for a narrow-band random record is contentrated around the frequency of the instantaneous variation within the envelope. In spite of the seemingly random nature of vibrating particle beds, the results of this work does indicate a strong degree of statistical regularity.

In order to compute statistics for the flow, it is necessary to accumulate (or sample) large quantities of data after the system reaches steady state (at t = t_0). This is done by restarting the code at t_0 and storing the configuration data (i.e., phase space). A minimum time interval for sampling t_S should be chosen to be approximately one-half of the mean collision time (time for the loading-unloading process to occur) to compensate for the fact that during a collsion, the direction of a particle's velocity will change. An approximation to this time is used, given by $(n/2)\Delta t$, where Δt and n are defined in equation (2-5-4).

If $X(f)$ is the Fourier transforms of real time function $x(t)$, the power spectral density of $x(t)$ can be expressed as,

$$S(f\pm) = \lim_{\tau_p \to \infty} \frac{1}{\tau_p} X(f) X^*(f) \tag{3-2-1}$$

where $S(f\pm)$ is the spectral density function over positive and negative frequencies, τ_p is the averaging period, and X^* is the complex conjugate of X.

An important statistic is the correlation function, which is a measure of the "similarity" between two stochastic variables $w_1(t)$, $w_2(t)$. We imagine performing a large number of experiments to generate an ensemble (or collection), denoted by $\{w_1(t)^k, k = 1,2,3,\ldots\}$, $\{w_2(t)^k, k = 1,2,3,\ldots\}$ Then, as shown in Figure 3.2a, the correlation between them is determined by multiplying the ordinates of the two records at each time t and then computing the average value, denoted by $\langle w_1(t) w_2(t) \rangle$, over the ensemble of experiments by dividing the sum of the products by the number of products. It is evident that the correlation so found will be largest when the two records are similar or identical. For dissimilar records, some of the products will be positive and others will be negative, so their sum will be smaller.

Next consider the case where $w_2(t) = w_1(t) = w(t)$. Then the autocorrelation function, denoted by $R(\tau)$, is defined by $\langle w(t) w(t+\tau) \rangle$, where $\langle \ \rangle$ denotes the average over the ensemble. Here τ is a time shift, as shown in Figure 3.2b. $R(\tau)$ is then the expected value of the product $w(t)w(t+\tau)$, that is,

$$R(\tau) = E[w(t)w(t+\tau)] = \langle w(t)w(t+\tau)\rangle \tag{3-2-2a}$$

If the process is ergodic, i.e., that the ensemble average can be replaced by a time average taken from only a single sample which is representative of the ensemble, then the autocorrelation can be computed as,

$$R(\tau) = \langle w(t)w(t+\tau)\rangle = \frac{1}{t_{\max}} \sum_{t=1}^{t_{\max}} w(t)w(t+\tau) \tag{3-2-2b}$$

where t is the sampling time t_s, and t_{max} is the maximum time over which the computation is performed, usually one-half of the simulation run time. Properties of $R(\tau)$ can be found in (52) and are briefly discussed here. If $w(t)$ is stationary, then $E[w(t)] = E[w(t+\tau)] = m$. Also, because of the assumed stationary nature of $w(t)$, the value of $R(\tau)$ depends only on the time interval; hence $R(\tau) = R(-\tau)$ and therfore the function is even-valued. It is clear that $R(\tau)$ reduces to the mean square value $E\left[w(t)^2\right]$ at $\tau = 0$ which is its maximum. Since for a random process there will be no correlation between $w(t)$ and $w(t+\tau)$ at large values of τ, it can be shown that $\underset{\tau\to\infty}{R(\tau)} \to m^2$. Consequently, for processes with a zero mean, $R(\tau)$ decays to zero as $\tau \to \infty$. If $w(t)$ is periodic, $R(\tau)$ is always periodic.

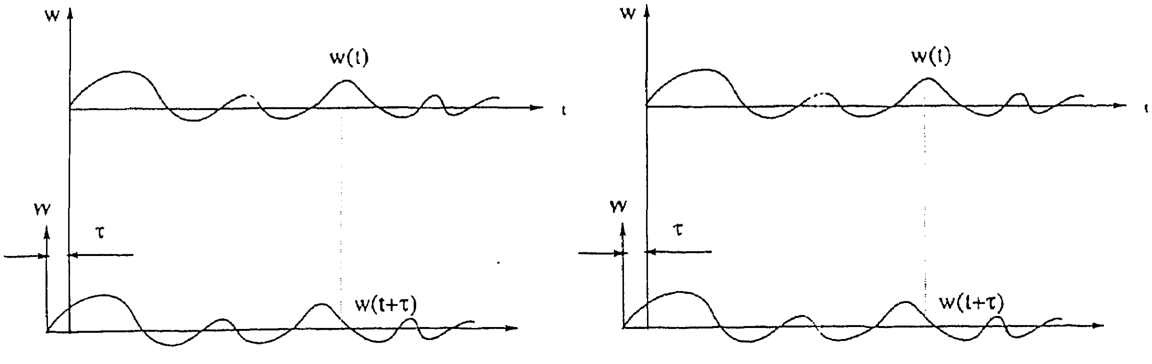

Figure 3.2 Calulation of correlation functions.
(a) Correlation between $w_1(t)$ and $w_2(t)$, (b) $w(t)$ shifted by τ

Similarly, the cross-correlation between two variables of $w(t)$ and $u(t)$ is defined by,

$$R_{wu}(\tau) = E\left[w(t)u(t+\tau)\right] = \left\langle w(t)u(t+\tau)\right\rangle$$

(3-2-3)

$$= \frac{1}{t_{\max}} \sum_{t=1}^{t_{\max}} w(t)u(t+\tau)$$

Unlike the autocorrelation function, the cross-correlation is not an even-valued.function of τ, It has an important application in detection of the time delays between two signals, which will be shown by following example.

Consider two random processes $x(t)$ and $y(t)$, defined by

$$x(t) = x_0 \sin(\omega t + \theta)$$

$$y(t) = x_0 \sin(\omega t + \theta - \phi)$$

where the probability density of phase angles θ is given by,

$$p(\theta) = \begin{cases} \frac{1}{2\pi} & \text{for } 0 \le \theta \le 2\pi \\ 0 & \text{elsewhere} \end{cases}$$

and ϕ is a constant phase angle. Obviously, $y(t)$ can be regarded as the response of $x(t)$ in an electrical or mechanical system with a phase lag ϕ. Then the autocorrelation function $R(\tau)$ of $x(t)$ can be calculated from the definition (3-2-1) as,

$$R(\tau) = E\left(x(t)x(t+\tau)\right) = E\left[x_0^2 \sin(\omega t + \theta)\sin(\omega t + \omega\tau + \theta)\right]$$

$$= \frac{1}{2\pi}\int_0^{2\pi} x_0^2 \sin(\omega t + \theta)\sin(\omega t + \omega\tau + \theta)\, d\theta$$

which, after making use of the identity,

$$\sin(\omega t+\omega\tau+\theta)=\sin(\omega t+\theta)\cos(\omega\tau)+\cos(\omega t+\theta)\sin(\omega\tau)$$

and evaluating the integrals, gives,

$$R(\tau)=\frac{1}{2}x_0^2\cos(\omega\tau). \qquad (3\text{-}2\text{-}3)$$

The cross-correlation function R_{xy} of $x(t)$ and $y(t)$ can be calculated in a similar manner as,

$$R_{xy}(\tau)=E(x(t)y(t+\tau))=E\left[x_0^2\sin(\omega t+\theta)\sin(\omega t+\omega\tau+\theta-\phi)\right]$$

$$=\frac{1}{2\pi}\int_0^{2\pi}x_0^2\sin(\omega t+\theta)\sin(\omega t+\omega\tau+\theta-\phi)d\theta$$

which results in,

$$R_{xy}(\tau)=\frac{1}{2}x_0^2\cos(\omega\tau-\phi) \qquad (3\text{-}2\text{-}4)$$

A comparison of $R(\tau)$ with R_{xy} shows that they differ only by a phase angle. In the event that two random signals have almost same power spectral density, (which means their frequency contents are almost same), the phase lag, usually not easily detected from the original waveforms, can be found by comparing the peaks in the plots of autocorrelation and cross-correlation functions.

Another important application of time correlation function occurs in the determination of a self-diffusion coefficient, which, in three dimensions, is given by,

$$D=\frac{1}{3}\int_0^{\infty}d\tau\langle \mathrm{v}(\tau)\cdot \mathrm{v}(0)\rangle \qquad (3\text{-}2\text{-}5)$$

where $\mathrm{v}(0)$ is the centre-of mass velocity of a single particle at time zero, and $\mathrm{v}(\tau)$ is the velocity at a time τ seconds later. The autocorrelation function used in this context $\langle \mathrm{v}(\tau)\cdot \mathrm{v}(0)\rangle$ in (3-2-5) represents an ensemble average, which, in performing the actual calculation, is replaced by a time average, assuming that the process is ergodic. During the simulation, the velocities of a particle are sampled (after the system attains steady state) at equally spaced intervals t_s. In order to improve statistical accuracy, in this study, the velocity autocorrelation functions are first computed for each of the N free particles separately, and then the results are added together and divided by N to obtain an average value. Hence, for each value of τ which is a multiple of the sample time t_s, the autocorrelation $R(\tau)$ is computed as,

$$\begin{aligned} R(\tau) &= \langle \mathbf{v}(\tau)\cdot\mathbf{v}(0)\rangle = \frac{1}{N}\sum_{i=1}^{N}\langle \mathbf{v}_i(t+\tau)\cdot\mathbf{v}_i(t)\rangle \\ &= \frac{1}{N}\sum_{i=1}^{N}\left[\frac{1}{t_{\max}}\sum_{t=1}^{t_{\max}}\mathbf{v}_i(t+\tau)\cdot\mathbf{v}_i(t)\right] \end{aligned} \tag{3-2-6}$$

The self-diffusion coefficient, which is the trace of the diffusion tensor, is then computed from (3-2-5). This function will, in general, decay to zero at a time called the "relaxation time".

In performing the autocorrelation calculation (3-2-6), the number of time-sampled velocities for each particle should be sufficiently large, otherwise the statistical precision for large time shift values τ will be very poor. For example, if the number of velocity data values is equivalent to the maximum time shift ($\tau_{\max} + 1$), calculation of $R(\tau_{max})$ will involve only one term in the sum, i.e., the product of first and last data value. To avoid this, a set of two thousand velocity data points for each particle has been used in this study, while the maximum time shift is only one thousand. Thus the product terms in summation (shown as t_{max} in (3-2-6)) is at least one thousand for each τ.

The autocorrelation computation expressed by (3-2-6) will be very time consuming if the data stored in a file are read in by FORTRAN direct access I/O statements. Most of the CPU time would spent on accessing data from the file in a nonsequential manner. To speed up the computation, a large array is generated to store velocity time history of all *N* particles. Although for a large system of particles, this array will require substantial memory, approximately 95 percent savings in CPU time is achieved.

It is also possible to improve the speed of calculating time correlation function by taking the advantage of FFT technique (53). The autocorrelation function may be obtained by using the inverse Fourier transform of the spectral density. But this technique would require even more memory, which was not available in computer system used in these studies.

3.3 Mean Square Displacement

A method to compute the self-diffusion coefficient *D* has been evaluated in the previous section by means of velocity autocorrelation function. An equivalent method using the Einstein expression for self-diffusion, is discussed in this section. In what follows, a derivation of this expression and its relationship to the autocorrelation function is presented (54).

Suppose that at time $t = 0$ a group of particles are located within a small volume centered at $\mathbf{r} = 0$. At time t, the fraction of these particles per unit volume around the point $\mathbf{r}$, denoted by $G_s(\mathbf{r},t)$, obeys a diffusion equation given by,

$$\frac{d}{dt}G_s(\mathbf{r},t) = D\nabla^2 G_s(\mathbf{r},t) \qquad (3\text{-}3\text{-}1)$$

where *D* is the self-diffusion coefficient. Under the isotropic assumption, a solution of (3-

3-1) subject to the initial condition that $G_s(\mathbf{r},0)=\delta(\mathbf{r})$ is,

$$G_s(r,t)=\frac{1}{(4\pi Dt)^{3/2}}\exp\left(-r^2/4Dt\right) \tag{3-3-2}$$

It is clear that $G_s(r,t)dr$ is the probability of finding a particle in a region dr around point r at time t given that the particle was at the origin at time $t = 0$. So the mean square displacement $\left\langle |\mathbf{r}|^2 \right\rangle$, computed as the expected value of r^2, is given by,

$$\left\langle |\mathbf{r}|^2 \right\rangle = \int_0^\infty r^2 G_s(r,t)\cdot 4\pi\, r^2 dr \tag{3-3-3}$$

Upon substituting (3-3-2) into (3-3-3) and integrating, the Einstein relation

$$2tD=\frac{1}{3}\left\langle [\mathbf{r}(t)-\mathbf{r}(0)]^2 \right\rangle \tag{3-3-4}$$

is obtained. Thus the self -diffusion coefficient D can be computed from the mean-square displacement as,

$$D \equiv \lim_{t\to\infty}(6t)^{-1}\left\langle [\mathbf{r}(t)-\mathbf{r}(0)]^2 \right\rangle \tag{3-3-5}$$

Equation (3-3-5) is equivalent to (3-2-5) for stationary processes as can be seen by observing that

$$\begin{aligned}\frac{1}{2t}\left\langle (\mathbf{r}(t)-\mathbf{r}(0))^2 \right\rangle &\approx \frac{1}{2}\frac{d}{dt}\left\langle (\mathbf{r}(t)-\mathbf{r}(0))^2 \right\rangle \\ &= \int_0^t d\tau \left\langle \dot{\mathbf{r}}(\tau)\dot{\mathbf{r}}(0) \right\rangle\end{aligned} \tag{3-3-6}$$

In the actual computation of the mean square displacement, the same averaging strategy is employed as that in computing the autocorrelation function. That is, the mean square displacement for each particle is obtained, and an average is then computed for the system of particles. Hence we have,

$$\left\langle |\mathbf{r}|^2 \right\rangle = \frac{1}{N}\sum_{i=1}^{N}\sum_{t=1}^{t\max}\left\{\left[x_i(t+\tau)-x_i(t)\right]^2+\left[y_i(t+\tau)-y_i(t)\right]^2+\left[z_i(t+\tau)-z_i(t)\right]^2\right\} \quad (3\text{-}3\text{-}7)$$

where x_i , y_i and z_i are the center coordinates of particle *i*, which are not reflected back into the primary computational cell when they move outside of this cell. In running the simulation, before restarting the code for sampling after steady state is attained, the input *icoord*, is set to *1*, which signal the output of the particles' real coordinates possibly outside of the primary computational cell.

The Einstein relation provides an alternative way to compute aself-diffusion coefficient and it also has some advantages over velocity autocorrelation method. In the case that the correlations decay slowly to zero, their tails may extend so long as to exceed the range for which the velocities have been recorded. By omitting the contribution of the integral under such a long tail, significant statistical errors in diffusion coefficient calculation can occur. Use of the mean square displacement, however, does not require any numerical integration, and in addition, the treatment of displacement variables is relatively easy to handle. In this study, both methods are used for comparison purposes.

CHAPTER 4

SMOOTH UNIFORM BEDS WITH PERIODIC SIDE WALLS

The particle dynamics modeling of the smooth, uniform vibrating beds with periodic side walls and a flat vibrating floor will be discussed in this Chapter. The focus on the simple smooth, uniform beds makes it possible to compare these results with recent kinetic theory predictions. The use of periodic side boundaries permits modeling of a small system without significant wall effects. Since nearly smooth, uniform spheres have been used in many of the experiments on vibrating granular beds, it is also possible to find suitable cases to check the effectiveness of the results to be discussed.

The computational cell (see Figure 2.8a) in this study consists of a plane floor, periodic boundaries along the sides and an open top surface. The cell is usually 2.5 times as high as the densest packing. A right-handed Cartesian coordinate system is established such that the origin of the x and z axes coincides with a corner of the floor; gravity acts in the $-y$ direction.

After the initial configuration has been randomly generated in the cell, a "pouring" of particles is simply simulated by allowing particles to fall freely under the influence of gravity into a loose packing. Then the bottom plane starts to vibrate sinusoidally. At the first second of shaking, the amplitude of velocity increases linearly from zero to a user input value. Usually it takes more than four hundred shaking cycles for the system of particles to reach a "steady state". After that statistics to compute long time cumulative averages of diagnostic parameters are accumulated. In order to determine the depth profiles of diagnostic quantities, the cell is partitioned into zones (or layers) of thickness equal to the sphere diameter.

The first study is focused on an investigation of the temperature and solids fraction depth profiles of uniform, smooth beds to compare the results with recent theoretical predictions of Richman and Martin (46) for smooth spheres. The effects of the bed mass, the boundary shaking velocity and acceleration have been investigated. The influence of normal stiffness (with restitution coefficient fixed) on simulation results is also studied.

Bed expansion and densification phenomena are examined by using a fixed displacement amplitude of shaking. The influence of shaking acceleration on the bed height and average cell packing fractions are analyzed and compared with the experimental results of Hunt et al. (18).

Spectral analysis methods are introduced to examine the coupling between the boundary velocity and the mean velocity in each layer. A simple method to measure the sound attenuation in the granular medium is also discussed.

Diffusion in granular vibrating beds has also been carefully studied. Results calculated from velocity autocorrelation functions are compared with those obtained by mean square displacement methods and analytical methods.

The diagnostic methods used in this study have been briefly introduced in Chapter 3, and will be specified in each case study before introducing the results.

4.1 Temperature and Solids Fraction Profiles

The concept of a granular temperature is perhaps the most important key to understanding the behavior of agitated granular systems. The work done by the external forces transfers kinetic energy into mean motion of a granular system. Meanwhile, the interparticle collisions convert some of the kinetic energy of the mean motion into granular temperature (which is the kinetic energy associated with the random particle velocities). Therefore, the magnitude of granular temperature is proportional to the mean velocity gradient within the material. Finally, the inelastic collisions will dissipate granular temperature into real thermodynamic heat. An increase in granular temperature reflects an increase in the random motion of the particles, a larger velocity gradient or a smaller dissipation due to inelastic collisions between particles.

Another physical quantity of interest is the solids packing fraction ν — the local fraction of the volume occupied by particles — of the granular bed. This quantity is directly connected with granular temperature, which will be shown by the simulation results which follow.

In order to examine the local change of temperature and solids fraction, a series of parameter studies were performed, from which comparisons with Richman and Martin's theoretical predictions (46) were made. In making these comparisons, several of their parameters are used.

To allow the floor to vibrate in three directions, the components of boundary particle velocity v are given by,

$$\begin{aligned} v_x &= v_0 \cos(2\pi f \cdot t) \\ v_y &= v_0 \cos\left(2\pi f \cdot t + {}^{2\pi}\!/_{3}\right) \\ v_z &= v_0 \cos\left(2\pi f \cdot t + {}^{4\pi}\!/_{3}\right) \end{aligned} \tag{4-1-1}$$

where v_0 is the velocity amplitudes and f is frequency. The components in (4-1-1) have different initial phase angles, in order to make v a rotary vector similar to the case of rotary currents in electricity. This is done in order to eliminate any mean motion across the cell. For smooth spheres and flat floor case, the x and z components do not transfer any momentum to the bed.

An analogy is made by equating the time average of (4-1-1) to Richman and Martin's rms boundary fluctuation energy, denoted by V^2. Hence,

$$V^2 = \frac{1}{3}\left\langle \mathrm{v}^2 \right\rangle = \frac{1}{3\tau}\int_0^{\tau}\left(v_x^2 + v_y^2 + v_z^2\right)dt = \frac{v_0^2}{2} \tag{4-1-2}$$

where τ is the period of the boundary velocity. This is normalized to yield a dimensionless boundary fluctuation velocity V_b,

$$V_b = \frac{V}{\sqrt{dg}} = \frac{v_0}{\sqrt{2dg}} = \frac{2\pi f \cdot a}{\sqrt{2dg}} \tag{4-1-3}$$

where d is the diameter of the particle, g is the gravitational acceleration, and a is the displacement amplitude. Obviously, V_b is a measure of the input boundary fluctuation energy.

The mass of spheres supported by the vibrating floor is quantified by the dimensionless "mass hold-up", m_t, which is given by

$$m_t = \int_0^{L/d} \nu(\xi) d\xi = \frac{N\pi d^2}{6A}, \tag{4-1-3}$$

where L is the depth of the bed, $\xi \equiv \frac{L-y}{d}$, $\nu(\xi)$ is the solid fraction along the depth, A is the cross-section area of the cell, and N is the number of the spheres. A dimensionless measure of granular temperature, given by

$$W(Y) = \sqrt{T/_{d \cdot g}} \tag{4-1-4}$$

where T is the granular temperature, $Y \equiv y/_d$, is introduced to characterize the effectiveness of the vibrating boundary to thermalize the granular mass.

4.1.1 Effect of Mass Hold-up m_t

In the first set of case studies, a system of acrylic spheres with density $\rho = 1200\,{kg}/_{m^3}$ and diameter $d = 0.1\ m$ was used. Sinusoidal oscillations of 50 Hz. were induced in three directions through the bottom of a computational cell, which has equal width and length ($xcell$ = $zcell$ = 0.5 m) and periodic side walls. The normal stiffness ($K_1 = 2.7 \times 10^8\ {N}/_{m}$) was estimated by the equivalent Hertz force model discussed in Chapter 3, yielding a time step dt = 6.4294×10^{-6} seconds. The effects of mass hold-up m_t and dimensionless boundary fluctuation velocity V_b on granular temperature and solids fraction depth profile were investigated. A summary of the parameter values used in this first set of studies appears in Table 4.1.

Table 4.1 List of parameters (Case 1)

Parameter	**Value**
Particle Diameter d (m)	0.1
Density ρ $\left(kg/m^3\right)$	1200
Normal Stiffness K_1 $\left(N/m\right)$	2.7×10^8
Restitution Coefficient	0.9
Frequency f (Hz.)	50
Mass Hold-up m_t	1.0, 2.5, 5.0
Boundary Fluctuation Velocity V_b	0.25, 2.0, 5.0

The behavior of vibrating beds with mass hold-up $m_t = 1.0$ *and* 2.5 is shown in Figures A4.1a,b for a fixed boundary fluctuation velocity $V_b = 2.0$. (displacement amplitude a can be calculated by (4-1-3), since f and V_b are known) The dimensionless granular temperature *W(Y)* and solids fraction are plotted versus the demensionless bed depth *Y*. The solid and dotted lines in the figures are the kinetic theory predictions of Richman and Martin (46).

For a shallow bed (m_t = 1), which consists of approximately two layers after pouring, the bed swells in the vibrated state and particles disperse forming an expanded bed, which is evident from its flat solids fraction profile (Figure A4.1b). The temperature *W(Y)* decreases slowly along the depth (Figure A4.1a). This phenomenon is qualitatively in agreement with the observations of Thomas et al. (16) in their "Newtonian state" experiments. In contrast to the shallow bed, the deep bed (m_t = 2.5, 5.0) is only slightly thermalized for the same boundary fluctuation velocity V_b. The temperature profiles $W(Y)$ in Figure A4.1a ($m_t = 2.0$) show a maximum at the vibrating floor and a monotonic decrease with depth, while the solids fraction profile $\nu(Y)$ has a peak at some intermediate depth and a lower value at the vibrating floor. Both temperature and solids fraction profiles are in good agreement with the kinetic theory predictions.

4.1.2 Effect of Boundary Fluctuation Velocity

The results in Figures A4.2a, b show the behavior of the bed when boundary input fluctuation velocity is increased for a fixed granular mass ($m_t = 5$). Large values of V_b are more effective in thermalizing the bed as depicted by the increase of $W(Y)$ in Figure A4.2a and in the expansion of the bed shown in the solids fraction profiles of Figure A4.2b. Since the total mass in the cell is equal, the area enclosed by each solids fraction curve is the same for each case. However, the shapes of these areas are quite different. A large agitation ($V_b = 5.0$) pushes most of the mass to the top. When the agitation is small ($V_b = 0.25$), the bed is only slightly thermalized with a nearly uniform density. In all cases, the maximum temperature appears in the bottom, where the particles' motion is quite random and the solids fraction is low. Simulation results again show good agreement with the theoretical curves (46), represented by solid or dotted lines in Figures A4.2a, b.

Figures A4.1 and A4.2 reveal that when energy input is large enough, the vibrating bed can maintain a region of low density near the bottom floor, where the granular temperature is maximum. This is similar to the effect of temperature on gases, where the density of gas decreases as temperature rises. As mentioned above, the value of the granular temperature is determined by the balance between temperature generation by the vibrating floor and dissipation via inelastic collisions. The large granular temperature near the vibrating floor can be attributed to the great temperature generation near the external energy source and the relatively small temperature dissipation due to the solids fraction in this region (i.e., low collision frequency).

4.1.3 The Influence of Normal Stiffness

In the previous simulations with acrylic spheres, an equivalent Hertz force model was used to estimate the value of normal stiffness, which resulted in a small time step Δt and consequently a substantial amount of cpu time. For a system of 240 particles with a diameter $d = 0.1$ m, this simulation required 72 hours cpu time on a SUN sparc-10 workstation. For $d = 0.003m$, the cpu time will be longer than 240 hours. Therefore, the influence of loading stiffness K_1 has been carefully investigated. The objective is to find a reasonable range for which the results would be essentially unaffected. A system of $N = 119$ spheres is used for the test runs; all parameters can be found in Table 4.2.

Table 4.2 List of parameters (Case 2)

Parameter	Value
Particle Diameter d (m)	0.01
Density ρ $\left(kg/m^3\right)$	2490
Normal Stiffness K_1 $\left(N/m\right)$	2.7×10^8, 3.64×10^6, 1.2×10^5
Restitution Coefficient	0.9
Frequency f (Hz.)	50
Mass Hold-up m_t	2.5
Boundary Fluctuation Velocity V_b	2.0

First the stiffness $(K_1)_H$ was found using the equivalent Hertz model (equation (2-5-10)) which was described in Chapter 2, section 5. Since the time step dictated by this computed value was very small, a trial value of $K_1 \cong (K_1)_H \times 10^{-2}$ was selected. During the simulation, the overlap was monitored and if its maximum value α_{max} exceeded one percent of a particle diameter, the simulation was halted. The value of K_1 was increased slightly and the procedure repeated until $\alpha_{max} \leq 0.01d$. Figures A4.3a and A4.3b compares results for three different stiffness values with other parameters being identical. The dotted lines in figures are theoretical predictions of Richman and Martin (46). The triangles are the results for the stiffness estimated by the equivalent Hertz model (equation (2-5-10)); the crosses represent the results found by the monitoring α_{max}, and the circles are the results for a stiffness much smaller than the previous two values. Only a small difference was found between the depth profiles of granular temperature and solids fraction. Hence, a reduced stiffness value obtained from the maximum overlap procedure has been used in the majority of the investigations in order to reduce computing time.

4.1.4 Effect of Shaking Acceleration

In order to determine the range of shaking acceleration amplitude $\Gamma = a\omega^2$ in which the simulation results agree with the kinetic theory predictions, a system of 119 spheres (m_t = 2.5, $\rho = 2490 \ {}^{kg}\!/_{m^3}$), with diameter d = 1 cm, was studied under a fixed boundary fluctuation (V_b = 2.0) and a varied frequency range from 5 Hz. to 100 Hz. This corresponds to a change of acceleration Γ from $2.84g$ to $56.5g$. It is important to observe that in these studies, since V_b is held fixed, an increase of Γ as frequency f is increased implies a compensating decrease in amplitude a. A pronounced effect of acceleration Γ on the depth profiles of dimensionless temperature and solids fraction can be found in Figures A4.4a and A4.4b. The data matches well with kinetic theory predictions when $\Gamma = 28.3g$ (f = 50 Hz.) and $56.5g$ (f =100 Hz.), where the granular mass is apparently thermalized to a degree consistent with assumptions implicit in the theory. However, at the low accelerations (eg., $\Gamma = 5.68g$), the granular temperature does not decrease monotonically from the bottom to the top as predicted by the kinetic theory. For $\Gamma = 2.48g$, the dimensionless temperature decreases slowly from the maximum value at the bottom, reaches a minimum at about 5 layer above the floor, and then increases slowly to a constant value at the top of the bed. The solid fraction profile shows a large expansion of the bed with a peak located at the layer where temperature has its minimum value.

Deviation of simulated results when Γ is small from kinetic theory predictions provides motivation for the next series of investigations in which comparisons are made with existing experimental data.

4.2 Bed Expansion and Densification Phenomena

This study aims at comparing simulation results with recent experimental data provided by Hunt et al. (18) for the average solids fraction and bed height of a vibrating mass of glass spheres. In order to make a legitimate comparison between the physical data and simulated /computed quantities, we employ the same materials as used in the experiments, i.e., glass spheres of density $\rho = 2490\ {}^{kg}\!/_{m^3}$ and diameter d = 3 mm.

The primary computational cell, which is 15 mm in both length and breadth has periodic side walls and a smooth plane vibrating floor. The total bed mass in the simulation cell is much smaller than the total mass (136 kg) used in the acutal experiment cell. However, the use of periodic side walls makes it possible to compare the results if the mass hold-up in simulation cell is the same as calculated from the experiment cell (m_t = 5). Consequently, the number of spheres N = *239* and primary computational cell dimensions were chosen so that m_t = 5. Smooth spheres (no rotation) are employed in the simulations since particles used in the experiments were essentially smooth,

The vibrational parameters of the simulations are also the same as those used in the experiments. A vertical sinusoidal vibration is introduced from the bottom floor, with a fixed displacement amplitude of 5 mm (1.67d). The vibrational frequencies are varied from 7 Hz. to 38 Hz., corresponding to a change in shaking acceleration from 1 to 30g.

Due to the large Young's modulus of glass, the normal stiffness estimated by the equivalent Hertz model is large. With such large a stiffness and such small a diameter, the time step would be very small. Therefore, the stiffness used in this simulation is determined by the criterion that maximum overlap would not exceed one percent of the sphere diameter. Table 4.3 lists all of the relevant parameters for this study.

Table 4.3 List of parameters (Case 3)

Parameter	**Value**
Particle Diameter d (m)	0.003
Density ρ $\left({kg}/{m^3}\right)$	2490
Normal Stiffness K_1 $\left({N}/{m}\right)$	10^6
Restitution Coefficient e	0.9
Shaking Amplitude (m)	0.005
Shaking Acceleration Γ (g)	1.0, 1.2, 2.0, 2.35, 2.8, 3.15, 3.6, 4.1, 30
Mass Hold-up m_t	5.0

In Hunt et al.'s experiments, the bed height was roughly determined from the height of a thin sheet of paper lid placed on the top of the vibrated bed. Obviously, their height measurements represented an average value since ballistic effects at the bed surface cannot lift the paper lid. In the results to be presented on bed height, only a single snapshot of the configuration was used and ballistic surface trajectories were ignored by removing those particles from the data file. The height was then determined from the solids fraction depth profile of this selected configuration. Clearly, more accurate computations could have been done by averaging over many configurations after the onset of steady state. In the physical experiments, average bulk solids fraction was computed by using the total volume of spheres divided by the product of the bed height and crosssectional bed area. The same technique is employed in the simulations. Although above measure of bulk solids frction is made by viewing one configuration, it is found that the bulk solids fraction calculated by above method is very close to long term average bulk solids fraction. (The long term depth profile of solids fraction will be discussed later). Hence, above estimation on bed height and bulk solids fraction is reasonable.

Comparisons of the average bed height and average bulk solid fraction versus acceleration Γ with the data of Hunt et al. (18) are presented in Figures A4.5 and A4.6. The figures show that the simulation bed expands a little bit higher than the experimental bed, which could be due in part to the neglect of friction between spheres in simulations. However, the basic trends are in agreement. The height of the simulation bed remains almost constant until the acceleration increases to $2g$, where a larger jump than reported in experiment occurs. As the acceleration increases, a further expansion is found in both simulation and experimental beds, with a plateau appearing at $\Gamma \cong 2.8g$. Simulations were also carried out at a large acceleration value of $\Gamma = 30g$, which is far outside of the experimental range. The data renders nearly the same bed height when $\Gamma = 30g$ as for $\Gamma = 3.6g$. It is important to note the critical Γ value for bed expansion predicted from the simulations lies beween 1.2 and $2.0g$. In Figure A4.6, the simulation and experiment data for bulk solid fraction are also found to be in good agreement except at $\Gamma = 2g$.

The granular temperature and bulk density profiles in Figures A4.7a and A4.7b depict a similar phenomenon as was shown in Figures A4.4a and A4.4b of the previous case. When the low acceleration vibrations are applied to the cell, the bed expands significantly. The maximum temperature area is near the top surface where the density is very low. The maximum density occurs several layers above the bottom where granular temperature is at its minimum value. In contrast, the temperature depth profiles for high Γ values exhibits behavior predicted by the kinetic theory. It is worthwhile to note that this case study is different from the case compared with the kinetic theory predictions (Figures. A4.4a, b) for which V_b was held constant. In the current study, the boundary fluctuation velocity increases as frequency (or Γ) increases since the amplitude is fixed. Hence, the local temperature near the bottom increases as Γ increases.

The location of the maximum density for different Γ values are plotted versus the dimensionless depth Y in Figure A4.8. As the acceleration increases, the peak shifts to a higher layer. The peak for $\Gamma = 30g$ is more than five times higher than the peak for $\Gamma = 1.2g$. This local density change is also observed in Figure A4.9, where the mass percentage below the depth Y has is plotted. For $\Gamma = 2g$, about 50 % of mass is located below a depth of five sphere diameters, as compared to only 10 % when $\Gamma = 30g$.

Snapshots of selected two dimensional configurations (projected on xy plane and the particle sizes has been reduced for clarity) in Figures A4.10 provides some interesting information. The bed height at $\Gamma = 1.2g$ remains the same as pre-vibrated bed (Figure A4.10a), but the particles are aligned in columns with the direction of shaking (Figure A4.10b). Although only one snapshot is plotted here, it was observed in simulation this phenomenon exit in all of the shaking phase angles, which is indicative of a strong coupling between the boundary and the bed. A surface fluidization phenomena is observed at $\Gamma = 2.0g$, where the less restricted top particle layers expand, while the bottom remains in a densely packed configuration. At $\Gamma = 3.15g$, the bed appears thermalized and expanded although its height is not significantly different from its value when $\Gamma = 2.0g$. A distinct local density change can be recognized upon comparing Figure A4.10e ($\Gamma = 30g$) with Figure A4.10d ($\Gamma = 3.15g$). At $\Gamma = 30g$, the strongest fluidization (or thermalization) appears at the bottom, while $\Gamma = 3.15g$, this takes place at the surface. These figures strongly support the granular temperature and solids fraction depth profiles of Figures A4.7a, b. We remark that for all values of Γ, regions of high granular temperature correspond to relatively low solids fractions, and vica versa.

The simulation results also show that the cell average granular temperature increases as Γ increases (Figure A4.11). When Γ is below $4.1g$, the average temperature increases quickly and a jump appears between 1.2 and $2.0g$. After $\Gamma = 4.1g$, the rate of increase is suddenly reduced. Related to this change, the average number of collisions per particle (average over 40 seconds) becomes smaller as Γ increases (Figure A4.12), where a rapid descent occurs between 1.2 and 2.0g. The collision number is reduced very slowly after $\Gamma = 4.1g$.

From the kinetic theory point of view, collision rate Λ (collisions/second) is a function of granular temperature and density, i.e., $\Lambda = 4\nu^2 d^2 (\pi kT)^{1/2}$ where k is the Boltzmann constant, T is the granular temperature and ν the solids fraction. When the density is low, the temperature must increase to maintain the same collision rate. Or, at a reduced collision rate, more energy must be dissipated per collision in order to dissipate same amount of energy. Consequently a higher granular temperature is produced.

The reason for the previously discussed differences in the granular temperature depth profiles at small and large values of Γ is explained as follows. When Γ is small, particles near the cell floor, do not experience a sufficient impulse to jump upwards and consequently they approximatly follow the oscillating floor motion. The temperature (and deviatoric velocities) near the floor is small, which is a combined effect of low temperature generation due to a weak floor acceleration and high collisional dissipation as a result of a high local solids fraction. The environment for particles near the top surface is quite different. These particles are not significantly overburdened, and a small agitation transferred from the bottom causes them to fly freely from the surface. The solids fraction is low here, and therefore the collisional rate is also low. This produces a high granular temperature at the top. It is obvious that when Γ is "small" and a region of high solids fraction exists near the floor, collisions will not be binary in nature. Rather, it is likely that continuous contacts are dominant in most of the bed. Accordingly, it is reasonable to expect simulation results to depart from kinetic theory predictions in this case.

For large values of Γ, the movement of particles near the bottom deviates from the floor motion. The temperature near the bottom is high, promoted by significant fluctuations supplied by the vibrating floor, and this in turn creates a region of low solids fraction. Transfer of boundary energy to the top of the bed becomes minimal which produces an upper region of low temperature and high solids fraction. It should be understood that high granular temperature (fluctuation energy per unit mass) doesn't necessarily imply a large total kinetic energy.

Simulation results (Figures A4.10c and A4.10d) support the hypothesis that fluidization begins from the surface (14, 17), and that the fluidized region expands as Γ increases. However this is true only for a range of small Γ values. In a high acceleration range, the fluidized region exists near the bottom with the dense region on the top. At any input shaking condition, energy is transfered from the bottom. Hence it is useful to study how the vibrating boundary couples energy into the particle bed.

4.3 Coupling Between the Boundary Motion and Bed Response

Granular temperature is important since it reflects the fluctuating contribution to the kinetic energy in a system. It is also relevent to study the mean motion, since granular temperature is proportional to the mean velocity gradient, and mean velocity itself reflects the average energy level in the flow. It is crucial to understand how the energy is transfered from the floor and how it propagates upwards through the bed of spheres.

In this study, the spectral analysis method has been used to quantify the mean velocity field of a vibrating bed, consisting of 239 smooth spheres with a diameter of 0.1m. A frequency of 7 Hz and amplitude of 0.05m are applied. Data is accumulated after the system reaches steady state and subsequent computations of the mean velocity time history for each layer (or zone) of the depth partition are performed, sampled and stored in a file. The time history of the component of mean velocity in the y-direction in each zone is shown in Figures A4.13. It is clear that the waveform in each zone does not change greatly except in top zones (zone 11,12 and 13), while the amplitude of the mean velocity is decreases rapidly. The power spectral density diagrams depict this fact more clearly. In every zone with the exception of the top zones, the maximum power peaks occur at the same frequency as the boundary shaking frequency. However, the magnitudes of these peaks decrease rapidly. This means the frequency components of mean motion in each zone (or layer) are wholly determined by the frequency of the floor. Energy is input from bottom, where power spetral density has the maximum value. As the energy is transfered by collisions from layer to layer, it becomes smaller and smaller, which is evident from the decrease in magnitude of the power spectral density. At the top layers, the time history and power spectral density differs considerably from the lower layers. The waveforms are similar to a wide-band random noise signal. The power spectrum exhibits a peak at a much lower frequency and this is indicative of a weak floor influence.

Although spectral density analysis produces the frequency components of a signal, it does not provide any phase information. This can be done by computing cross correlation functions between the time histories of the boundary velocity and y-components of the mean velocities in each zone. Several results are depicted in Figures A4.14 to examine the phase delay of energy tranfer between the floor and the bed. The autocorrelation of boundary velocity is shown in Figure A4.14a, where a peak in $t = 0$ is expected. Figure A4.14b displays the cross correlation function between boundary velocity and mean velocity in the second zone (near the floor). Obviously, the peak has already shifted a small amount to the right. As we move further away from the floor, the peak shift becomes larger. Computations using the velocity cross correlation between boundary and the tenth zone reveal a 0.118 second phase delay. This calculation provides a simple but useful method to measure the speed of sound in granular material for further study.

From above spectral and correlation analysis, it is clear that as the depth increases towards the bed surface, the energy transferred from the floor becomes smaller and the response to the boundary movement gets delayed. Finally at the very top of the bed, the influence of the vibrating floor is very small, and particles are in chaotic motion.

4.4 Autocorrelation Functions and Self Diffusion Coefficients

As discussed in Chapter 3, the velocity autocorrelation function of a system is in itself a good measure for the "randomness" of the vibrated bed, and it also provides a convenient means to calculate self-diffusion coefficients. In order to examine the randomness of the bed motion in different directions, the velocity autocorrelation functions are separated into three components as follows:

$$\langle \mathrm{v}(\tau)\cdot \mathrm{v}(0)\rangle = \langle \mathrm{v}_x(\tau)\cdot \mathrm{v}_x(0)\rangle + \langle \mathrm{v}_y(\tau)\cdot \mathrm{v}_y(0)\rangle + \langle \mathrm{v}_z(\tau)\cdot \mathrm{v}_z(0)\rangle \qquad (4\text{-}4\text{-}1)$$

In the above, the three terms on the right-hand side represent the coordinate components of velocity autocorrelation function. From (3-2-5) and (4-4-1), the self-diffusion D is computed as,

$$\begin{aligned} D &= \frac{1}{3}\int_0^\infty d\tau \cdot \langle \mathrm{v}(\tau)\cdot \mathrm{v}(0)\rangle \\ &= \frac{1}{3}\left[\int_0^\infty d\tau \cdot \langle \mathrm{v}_x(\tau)\cdot \mathrm{v}_x(0)\rangle + \int_0^\infty d\tau \cdot \langle \mathrm{v}_y(\tau)\cdot \mathrm{v}_y(0)\rangle + \int_0^\infty d\tau \cdot \langle \mathrm{v}_z(\tau)\cdot \mathrm{v}_z(0)\rangle\right] \qquad (4\text{-}4\text{-}2) \\ &= \frac{1}{3}\left[D_x + D_y + D_z\right] \end{aligned}$$

where D_x, D_y and D_z are regarded as the three components of self-diffusion coefficient D.

In this study, velocity autocorrelation functions and self-diffusion coefficients are calculated for a system of 239 smooth spheres with the same material parameters (see Table 4.4) as used in Section 4.1 (case 1), except that the normal stiffness ($K_1 = 2.8\times 10^6$) was reduced for computational efficiency (dt = 6.3135×10^{-5}). Only vertical sinusoidal vibration is induced from bottom. Table 4.4 provides a complete list of the parameters. Velocity data sampling was initiated after the simulation had run for 40 seconds. (Steady state conditions occurred at approximately 30 seconds.) The sample interval was one-half of the mean collision time. Since the number of time step during collision was set to equal 15 in this case study, the sample interval is 7.5 time steps. 2000 data points were accumulated for each velocity component and stored in three separate large files, from which autocorrelation function was computed.

Table 4.4: List of Parameters (Case 4)

Parameters	**Value**
Particle Diameter d (m)	0.1
Density ρ $\left({kg}/{m^3}\right)$	1200
Normal Stiffness K_1 $\left({N}/{m}\right)$	2.8×10^6
Restitution Coefficient e	0.9
Shaking Amplitude (m)	0.0089, 0.05
Shaking Acceleration Γ (g)	5, 10, 20, 90, 483
Mass Hold-up m_t	5.0

Calculations of D were compared with its value obtained from an analytical expression derived from the kinetic theory by Savage (23) and given by,

$$D = \frac{d\sqrt{\pi \cdot T}}{8(1+e) \cdot \nu \cdot g_0(\nu)} \tag{4-3-3}$$

Here, T is the granular temperature, ν is bulk solids fraction, d is the diameter of the particle and $g_0(\nu)$ is the Carnahan-Starling approximation to the radial distribution function at contact, i.e.,

$$g_0(\nu) = \frac{(2-\nu)}{2(1-\nu)^3} \tag{4-3-4}$$

In calculation, T and ν were expressed by cell average granular temperature and solids fraction respectively. The influence of shaking acceleration is first investigated with a fixed frequency (50 Hz.) and varied amplitude. Two large accelerations were selected:

$\Gamma = 90g$ ($a = 0.089d$) and $\Gamma = 483g$ ($a = 0.5d$). Since both cases have a high acceleration, the granular temperature and solid fraction profiles (Figures A4.15a and A4.15b) are consistent with the kinetic theory predictions. The maximum temperature in the bottom and density peak near the top indicates a chaotic motion in the low layers of this system. In Figure A4.16 and A4.17 the components of autocorrelation function are plotted versus time. In both cases, all three components have exponentially decaying tails. The x and z components are quite smooth, but the y components for both cases have a lot of wiggles in the tails, especially when a small amplitude ($0.089d$) is applied. This implies that in the direction of shaking (y), the motion of the boundary still maintains substantial influence on the up and down behavior of the bed even though the acceleration is large ($\Gamma = 90g$ or $483g$). Following equation (4-4-2), integrations of these autocorrelation functions yield the diffusion coefficients. It is found that the self-diffusion coefficient D for the small amplitude case is quite close to the value computed from the analytical predictions of Savage (see equation (4-4-3)). For the large amplitude case, D is slighly higher than the analytical value. (See Table 4.5 for a list of values).

Table 4.5 Self-Diffusion Coefficient

Parameters	D (Simulation) $(m^2/\text{sec.})$	$\overline{D}$ (Analytical) $(m^2/\text{sec.})$	Bulk Solids Fraction	Cell Ave. Temperature
$\Gamma = 90$ g, $f = 50$ Hz. (Amp. = 0.0089 m)	0.00544	0.00532	0.44	0.7950
$\Gamma = 483$ g, $f = 50$ Hz. (Amp. = 0.05 m)	0.2676	0.2116	0.14	13.80

The above computations show that for a fixed shaking frequency, the diffusion coefficient increases as acceleration (or amplitude) increases.

The effect of shaking acceleration on the diffusion coefficient is also examined with a fixed amplitude and varied frequency. Three acceleration values ($\Gamma = 5g$, $10g$, $20g$) are selected with a fixed amplitude equal to $d/2$. The temperature and solids fraction profiles (Figures A4.18 and A4.19) for these three cases are quite different. The autocorrelation functions are plotted in component forms in Figures A4.20, A4.21 and A4.22. It is found that the x and z components of autocorrelation functions for all three cases are very smooth and close to the exponentially decaying time correlation function assumed in the kinetic theory analysis (23). As Γ increases, the initial value (at $t = 0$) of these components increases. The important observation here is that the autocorrelation functions for v_y do not exhibit a relaxation time by decaying to zero, but oscillate for all cases, indicative of a strong correlation with the vertical boundary motion. Since the form of the boundary velocity is a *cosine*, then a total correlation of the bed with the boundary would produce a *cosine* autocorrelation function. Although not presented in this work, the autocorrelation function of the y-component of the velocity at $\Gamma = 1.2g$ did behave as a cosine function. In Figure A4.20 ($\Gamma = 5.0g$), this tendency is still very large. As Γ increases, the oscillatory part in the autocorrelation function of v_y (Figure A4.22) becomes less pronounced. Therefore it is not unreasonable to see that the oscillations in the tail persists even $\Gamma = 90g$ Figure A4.16). The calculation of y-component of self-diffusion coefficient (D_y) has been omitted, due to the strong correlated motion in y direction. The x and z components of diffusion coefficient are computed, and results are listed in Table 4.6 and plotted in Figure A4.23. Obviously, the diffusion coefficient increase as the acceleration increases, which supports Hunt's experimental data (18).

For the case $\Gamma = 10g$, the values of x and z component are very close to each other, while in the other two cases, the magnitudes of x and z component are slightly different. This maybe caused by the randomness of the particle motion. It is difficult to follow the system for a fairly long time and to sample a large amount of data due to the limited computing time and computer memory available for these investigations. For the diffusion computations, 2000 data were sampled every 0.94 seconds. Each sampled value is actually a short term average value. When velocity autocorrelation functions were calculated, a maximum time shift of 0.47 seconds (1000 data points) was used in order to improve the accuracy. Given sufficient resources, it would be possible to follow the system for a significantly longer time period and to increase the quantity of sampled data, consequently minimizing differences between the D_x and D_z.

The relationship between diffusion and temperature is shown in Figure 4.24, where the D_x and D_z are plotted versus the x and z components of cell average granular temperature T_x and T_z. Results reveal a phenomena similar to thermal diffusion in thermodynamics, that is, diffusion increases as temperature increases.

Table 4.6 Self-Diffusion Coefficient

Parameter	D_x $(m^2/\text{sec.})$	T_x	D_z $(m^2/\text{sec.})$	T_z
$\Gamma = 5$ g, Amp. = 0.5d ($f = 5$ Hz.)	0.002765	0.1193	0.003420	0.1193
$\Gamma = 10$ g, Amp. = 0.5d ($f = 7$ Hz.)	0.006441	0.1656	0.006396	0.1675
$\Gamma = 20$ g, Amp. = 0.5d ($f = 10$ Hz.)	0.007554	0.2679	0.008691	0.2679

The effect of shaking amplitude on D has been studied for a fixed acceleration $\Gamma = 10g$. It is found when the amplitude descends from one-half of a diameter to one-hundredth of a diameter, the velocity autocorrelation function will decrease much faster. Figure A4.25 shows the autocorrelation function an amplitude of 0.00103m (0.01d), and $f = 50$ Hz. Although the acceleration is as high as $10g$, the initial value (at t = 0) of autocorrelation is very small, and the tendency to follow the boundary movement is strong, as can been seen from the small oscillation in the tails of the x and z components of autocorrelation functions. The diffusion coefficients when $a = 0.01d$ (Table 4.7) are nearly three orders of magnitude smaller than those when the amplitude is one half of a diameter.

Table 4.7 Self-Diffusion Coefficient

Parameter	D_x ($m^2/\text{sec.}$)	D_z ($m^2/\text{sec.}$)
Amp.= .00103 m, $\Gamma = 10g$ ($f = 50$ Hz.)	8.7×10^{-6}	9.3×10^{-6}
Amp. = .05 m $\Gamma = 10g$ ($f = 7$ Hz.)	0.006441	0.006396

In order to further validate the diffusion results above using velocity autocorrelations, the mean-square displacement of particle motion is calculated for use in equation (3-3-5). The absolute displacements of particles are sampled in the same way as was done to find the velocity autocorrelation functions. The procedure for determining the average is to first compute the mean-square displacement for each particle, and then these values are averaged over all particles in the system. The detailed calculation procedure has already been introduced in Chapter 3, Section 3.3.

Several cases, which have been already discussed in the calculation of autocorrelation function, are selected to compute the mean-square displacement. The system, consisting of 239 spheres with material properties are listed in Table 4.4, is shaked through the floor at an applied relative acceleration $\Gamma = 90g$. Its velocity autocorrelation functions are shown in Figure A4.16. The mean-square displacement $\langle |\mathbf{r}|^2 \rangle$ of this system, plotted versus time (seconds) in Figure A4.26, appears quite smooth and linear. By using the Einstein relation (equation (3-3-5), the self-diffusion is determined as one-sixth of limiting (at large t) slope of mean-square displacement curve. It is found that the self-diffusion coefficient determined in this fashion is exactly the same as that calculated from velocity autocorrelation function. The comparisons and results are listed in Table 4.8.

Table 4.8 Comparison of Self-Diffusion Results

Parameter	$D\ (m^2/\text{sec.})$	$D^*(m^2/\text{sec.})$
Γ=90 g, f = 50Hz.	0.00544	0.00530

Parameter	D_x $(m^2/\text{sec.})$	D_x^* $(m^2/\text{sec.})$	D_z $(m^2/\text{sec.})$	D_z^* $(m^2/\text{sec.})$
Γ = 10g	0.006441	0.006269	0.006396	0.006282

* Values are calculated from mean-square displacement method

The mean-square displacement for a system with acceleration $\Gamma = 10g$ ($f = 7$ Hz) was also computed and plotted in Figure A4.27. Here it is observed that the mean-square x-displacement $\langle x^2 \rangle$ and mean-square z-displacement $\langle z^2 \rangle$ curves are very smooth and linear, and have the same limiting slope. However, the mean-square y-displacement $\langle y^2 \rangle$ has a strong sinusoidal waveform, corresponding to the sinusoidal component in the long tail of velocity autocorrelation function (see Figure A4.21). It is anticipated that this curve (Figure A4.27) would approach a limiting slope if it were possible to perform the computations for a much longer period of time than was done in this study. However, this was not possible with the computing resources available. Following equation (3-3-4), the x and z components of self-diffusion coefficient (D_x and D_z) are computed by taking one-half of the limiting slopes of $\langle x^2 \rangle$ and $\langle z^2 \rangle$, i.e.

$$D_x \cong \lim_{t \to \infty} (2t)^{-1} \left\langle [x(t) - x(0)]^2 \right\rangle \qquad (4\text{-}4\text{-}5)$$

$$D_z \cong \lim_{t \to \infty} (2t)^{-1} \left\langle \left[z(t) - z(0) \right]^2 \right\rangle \tag{4-4-6}$$

The results listed in Table 4.8 show fairly good agreement with those calculated from velocity autocorrelation functions.

CHAPTER 5

FRICTIONAL BEDS WITH SOLID SIDE WALLS

The behavior of real granular beds is highly complex. The previous discussions on the smooth uniform beds cannot be applied to most cases, since the effects of factors such as particle friction, size distribution, and side walls must be incorporated into the modeling. Observations (4, 22, 55) indicated that various of phenomenon in granular beds, such as convection, heaping, arching and segregation are closely related to the friction between the particles and the walls. This then provides motivation for the following investigations of frictional beds with solid side walls.

The primary computational cell with a sinusoidal vertical floor vibration is illustrated in Figure 2.8c. Fixed solid flat side walls are only applied to the boundaries parallel to the *x-y* plane. The *y-z* plane boundaries are periodic, which assures homogeneity of properties in *x* direction. To measure and analyze the velocity field, the cell is partitioned into a lattice of small parallelepipeds in the *z-y* plane having a width equal to the *x*-dimension of the primary computational cell (Figure 5.1). Each small cell has same length and height equal to the diameter of the particle. The mean velocity in a small cell is calculated by averaging the velocities of those particles, whose center occupy the cell during the time interval. To do so, the (*y, z*) coordinate of the particle center is monitored at each time step to locate in which small cell it resides. For example, suppose the coordinate of the center of particle *i* at time *t* is (x_i, y_i, z_i). The *z* and *y* index (mc, nc) of the small cell occupied by particle *i* is given by,

$$mc = Int\left(z_i \cdot {mzcell}/{zcell}\right) + 1$$

$$nc = Int\left(y_i \cdot {nycell}/{ycell}\right) + 1$$

where *mzcell* and *nycell* are the total number of small cells in z and y directions, and *zcell* and *ycell* are the cell dimension in z and y directions, respectively. Accordingly, the velocity of particle i at that instant contributes to the small cell average. Both short and long term cumulative mean values are computed in this study.

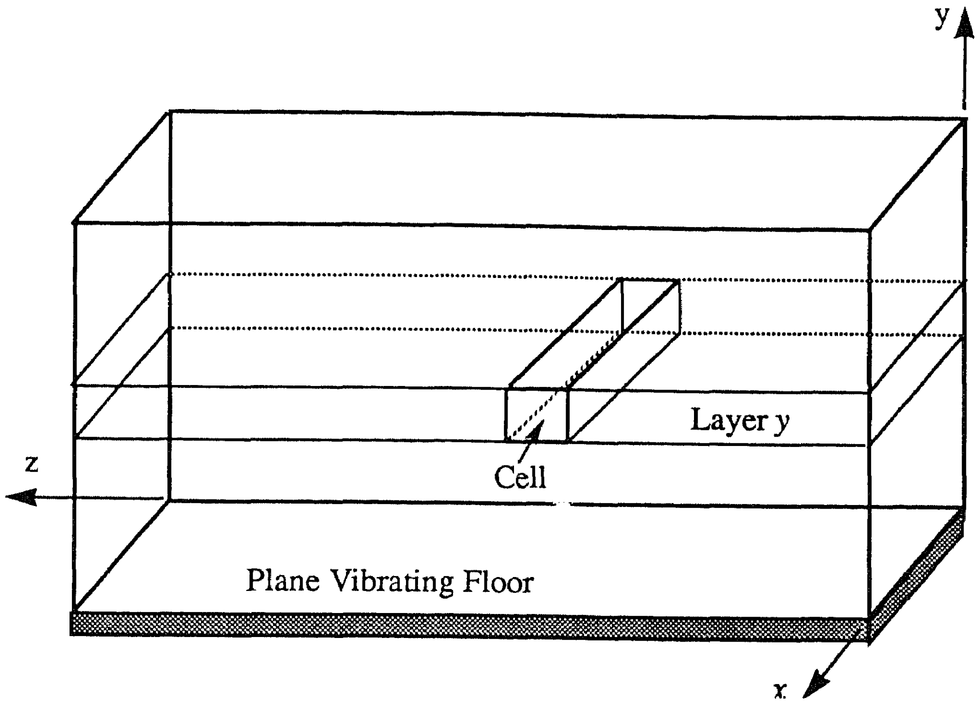

Figure 5.1 The primary computational cell is partitioned into small cells to determine the y and z components of the mean velocity field

5.1 Critical Conditions to Produce Convective Flow

When a mass of bulk solids is vibrated, under certain conditions a convective flow is induced whereby particles move upwards in the center and downwards in a narrow stream near the side walls. The occurrence of this phenomenon is dependent on a number of factors, such as particle properties, side wall conditions and vibratory parameters. It appears that the most critical of these is the existence of frictional or rough side walls. Indeed, no convection was found in these investigations when periodic boundary conditions were applied to compare with the experiments of Hunt et al (18). However, side walls alone are not sufficient and this will be discussed in what follows.

5.1.1 Effects of Shaking Amplitude

Shaking displacement amplitude is a key factor to produce a convective flow. With a fixed shaking acceleration of Γ = 10g, three different displacement amplitudes were chosen to test using a computational cell of length equal to 6*d* and width equal to 3*d*. The vibration and material parameters are listed in Table 5.1, and the convective velocity fields, which are long term averag value over 80 seconds after reaching a steady state, are shown in Figure A5.1, where the magnitude of velocity is quantified by the length of the velocity vector. No convection tendency was observed when a shaking amplitude of 0.25*d* was applied (Figure A5.1a). As the amplitude is increased to 0.3*d*, a steady convective flow develops as shown in Figure A5.1b, where a downward stream near the frictional side walls, and upward flow in the middle of the cell represents a typical circulatory pattern as observed by other workers (1, 21, 22). This convection becomes extremely strong at a amplitude equal to 0.5*d* (Figure A5.1c). But only the columns of particles directly touching the wall have a strong trend of downward motion due to the narrow cell length of 6*d*. At two particle diameters away from the side wall, the convection velocities is nearly zero. The magnitude of convective velocity for surface particles is much larger than those near the bottom, which is also illustrated in Figure A5.1. This velocity field is similar to that of Galas et al. (22), but different from Taguchi (21), which showed a convective velocity with a maximum magnitude at an intermediate depth, and very small magnitude near the surface. Perhaps this is because Taguchi used a relatively small acceleration $\Gamma < 4g$.

In order to quantitatively expressed the strength of the convective flow, the average magnitude of the convective velocity in the whole computational cell is calculated and listed in Table 5.1, from which the dependence of convection on displacement amplitude is very clear. Moreover, the average velocity magnitudes for each column of small cells are also plotted in Figures A5.2a, b and c, where the horizontal axes describe the location of the small cell in which convection occurs (*y*-*z* plane of the cell), while the vertical coordinates represent the magnitudes of mean velocity. It is found that the magnitude of convection velocity near the side walls shown in Figure A5.2c, where the shaking amplitude is $0.5d$, are significantly larger than those for the smaller amplitudes shown in Fig A5.2a, b. Both facts above indicate the possible existence of a threshold shaking displacement amplitude below which the convection will not occur even if the acceleration Γ is large. We remark that during the initial phases of these investigations, no convection was observed when high frequency and low amplitude vibrations (which means high acceleration Γ) were applied via the floor.

Table 5.1 Vibrational Parameters and Material Parameters

Diameter of the Particle (m)	**Normal Stiffness** (N/m)	**Density of particle** (kg/m^3)	**Friction Coefficient of the particle**	**Friction Coef of the Boundary**
0.1	2.8×10^6	1200	0.8	0.8

Acceleration (g)	**Frequency** (Hz.)	**Amplitude** (Dia.)	**Ave. Convection Velocity** (m/s)
10	7	0.5	0.0368
10	7.878	0.3	0.0185
10	9.996	0.25	0.0054

5.1.2 Friction Between the Particles and the Wall

The effect of the friction between the particles and side walls is examined in this study by considering limiting or extreme conditions. Four different pairs of friction coefficients have been considered while other parameters are held fixed (see Table 5.2). When the friction coefficient of particle (denoted by *fmu* in the code) is fixed at a value of 0.8, it is found that a large boundary friction coefficient (denoted by *fmub* in the code) results in a large convection velocity. This is shown in Figures A5.3 and A5.4 for the cases where *fmub* = 0.8 and *fmub* = 0.2. An extreme case is tested where the boundary friction *fmub* = *0*, which means that the side walls act only as a smooth constraint in the horizontal direction, and does not provide any tangential impulse to contacting particles. Figure A5.5 shows that the circulation direction is the same as above two cases, but the width of the downwards flow near the wall has extended to two particle diameters. An interesting change in flow pattern can be seen in Figure A5.6, when the particle friction coefficient *fmu* = 0, and boundary friction coefficient *fmub* = 0.8. The particles near the wall goes upwards instead of downwards, while all the other particles move downwards. As opposed to the convection patterns in Gallas et al's two-dimensional simulations (22), (which has been mentioned in Chapter 1), there are two convection cells, one at each side wall, shown in Figure A5.6 for this case.

Table 5.2 Parameters for study the effect of friction coefficient

Fixed Parameters	**Amplitude** (Dia.)	**Frequency** (Hz)	**Acceleration** (g)	**Normal Stiffness**
	0.5	7	10	2.8×10^6

Particle Friction Coefficient	**Boundary Friction Coefficient**	**Direction of Convection Along the Side Wall**
0.8	0.8	downwards
0.8	0.2	downwards
0.8	0	downwards
0	0.8	upwards

5.1.3 Influence of the Cell Size

Three different computational cell sizes were considered in this study. Their length × width ($z \times x$) dimensions are $100d{\times}1d$, $20d{\times}3d$, and $6d{\times}3d$. (These three cells will be referred to as $100d{\times}1d$, $20d{\times}3d$, and $6d{\times}3d$). The friction coefficients of the particle and the wall are equal to 0.8 (i.e., *fmu* = *fmub* = 0.8), while the other parameters are as listed in Table 5.2.

The convection field for a $20d{\times}3d$ cell shows the downstream flow near the wall has extended to two particle diameters. A symmetric convection pattern consisting two vortex-like structures is observed at the left and right side walls.(Figure A5.7) In the center of the cell, a small upwards stream is present.

The situation for the $100d{\times}1d$ cell is quite different (Figure A5.8a). Near the walls two small convective vortices exist which are about $8d$ wide each. This is similar to the $20d{\times}3d$ cell. In the center of the bed, convection is weak and appears somewhat random, as seen in the enlarged velocity field plot (Figure A5.8b). Figure A5.9 shows a significant difference of the velocity magnitudes near the near wall region and the central portion of the bed. It is possible that this is the reason why Hunt et al. (18) weren't able to observe a strong convective flow in their relatively large cell, while Zik et al. (24) were able to measure the convective motion near the wall.

The most striking phenomena while shaking the wide $100d{\times}1d$ cell is the occurrence of arching or waves. In Figures A5.10a-d, configurations of the z-y projected reduced spheres are shown at eight phase angles within a single cycle ($0, \pi/4, \pi/2, ..., 2\pi$). The dotted lines in each figure indicates the position of the vibrating floor at the instant shown. Arching almost disappeared when the bed mass made contact with the floor as it moved down from its highest position. Arching became more pronounced as the floor moved upwards from its lowest level. In examining several such sequences, this pattern did not appear to repeat itself in a predictable manner, but seemed somewhat random. In order to determine the local velocity field of the bed while arches are formed during a single shaking cycle, eight (short term) velocity field averages are computed, i.e.{(0 - $\pi/4$), ($\pi/4$ - $\pi/2$), .., ($7\pi/4$ - 2π)}, corresponding to the eight configurations shown in Figures 5-10a-d. These are presented in the vector field plots of Figures 5.11a-d, where regions devoid of spheres are visible, (i.e., velocity vectors are absent). In the central region of the bed away from the side walls, convection patterns can be seen forming over the cycle. However, averages taken over a long time scale (Figures A5.8a and A5.9) tends to hide the details. It is most likely that the creation and break-up of the arches occurs at some time scale not on the same order of the period of the vibrating floor. However, since only a single cycle was examined in these investigations, it is not possible to deduce the time scales of the observed arching structures.

5.2 Convection and "Segregation"

Convection and segregation are two different phenomenon. Convection is a means of particle transport and tends to promote mixing while segregation causes the opposite effect. Recently Knight, Jaeger and Nagel (37) argued that segregation can be caused by convection, since they found spheres of all sizes rise in the middle of a vibrated cylinder at the same rate, but the large particle became trapped on the top. The mechanisms which cause this large particle to remain at the top are those which promotes size sorting (or segregation) and therefore must be understood. In this study, various of shaking conditions, friction coefficients and boundary conditions have been examined. Analogous to the physical experiments of Knight et al. (37), a strong induced convection field was responsible for the motion of large sphere upwards through the cell. Therefore, this section addresses the connection between the transport of a large particle in relation to an induced convective velocity field. No attempt is made here to uncover those mechanisms which promote size sorting.

First, the influence of cell size was studied. A large sphere, with diameter $D = 3d$ (where d is the diameter of the smaller bed spheres) was placed in the center of the floor.

Other parameters are the same as listed in Table 5.1. In a $6d\times3d$ cell, the large sphere moved up quickly (about 15 seconds), and then remained on the surface thereafter. Figure A5.12 shows the trajectory of the large particle. The reason why the large particle has been trapped at the surface is as Knight et al (37) had explained, that is, the narrow downward convecton stream cannot carry it back down. In a larger $20d\times3d$ cell, the large particle ascended to the top at the almost same speed, but it sank near the wall to an intermediate depth and then moved up again (Figure A5.13). The large sphere, initially located in the center of the floor of a $100d\times1d$ cell, did not move upwards during a 160 second run, due to the nature of the convection field discussed in the previous section.

The displacement and velocity of the large particle have been compared with those of several small particles. We choose one of these just beneath the large one and another adjacent to the wall. The behavior to be described for these two small particles is typical several others considered. The displacement and velocity time histories and power spectral densities are shown in Figures A5.14a, b, c. It is obvious that the small sphere beneath the large one experiences a very similar displacement and velocity history to that of the large sphere (Figures A5.14a, b). Both particles experience a pulse-like upward displacement and saw-tooth like velocity, whereby each jump in the velocity coincides with a rapid ascent in displacement. The linear regressions for both displacement curves exhibit an almost same slope, which means the large and small particle rise at a same speed. The spectral density for both velocities showed a same significant frequency peak at around 2.5 Hz, which is much lower than the boundary frequency of 7 Hz probably due to the existence of friction. This is quite different from the smooth sphere studies presented in Chapter 4, where the power spectral density of mean velocity in each zone exhibited a peak at the shaking frequency of 7 Hz. It is important to notice that the power spectral density for the small particle near the wall (Figure A5.14c) also showed a maximum peak located around 2.5 Hz, although its net displacement is downwards.

Factors which affect the strength of the convection field must influence the speed of large sphere. Therefore, as the shaking amplitude increases, the strength of convection increases, which causes the large particle to reach the surface more quickly. An increase of friction coefficients for the walls and particles also creates a faster upward movement. In Figure A5.15, the effect of wall and particle restitution coefficients (e_b, e, respectively) on the speed of large particle in a 6d × 3d cell is shown for different pairs of e_b and e, with both particle and particle friction coefficients equal to 0.8. The large particle reaches the surface very quickly (15 seconds or 105 shaking cycles) when $e_b = e = 0.6$; this occurs much more slowly (60 seconds or 420 shaking cycles) when $e_b = e = 0.9$. The large restitution coefficient promotes a higher granular temperature in the system, but causes a decrease in the strength of convective velocity field, as shown in Figure A5.16a, b. By examining the other two cases (Figure A5.15), i.e., when $e = 0.6$, $e_b = 0.9$, and $e = 0.9$, $e_b = 0.6$, it is concluded that a small restitution coefficient for free particles ($e = 0.6$) is in favor of speeding up the large particle.

The neighborhood of large sphere has been studied by computing the coordination number history over a shaking cycle. The smallest coordination number is unity when the floor moves downwards from its highest position, while the largest coordination number occurs while the floor moves upwards. It can been observed from Figure A5.17, that the peak of the coordination number curve coincides with the peak of large particle velocity. This indicates that the upward motion of large particle does not occur during its free flight period, but during the time when it is closely surrounded by small particles. It is worth while mentioning the fact that the neighborhood of smaller spheres around the large sphere remains unchanged as it move upwards and this means these small particles are "dragged up" with the large one within the convection stream.

From above analysis, it appears that induced convection is responsible for particle transport and does not result in size separation. Further studies are needed and these will be discussed in Chapter 6.

CHAPTER 6

SUMMARY AND CONCLUSIONS

An in-depth investigation of the behavior of vibrating granular beds has been carried out using particle dynamics simulations, an outgrowth of molecular dynamics type studies used in the field of statistical and computational physics, to model this complex N-body problem. Such problems are generally non-equilibrium in nature. This work has applications in the field of bulk solids transport used in numerous solids handling industries.

Smooth uniform beds are modeled in a primary computational cell with periodic side walls and a plane vibrating floor. It is found that the bed behavior is strongly dependent on the floor shaking acceleration amplitude (Γ).

In the low Γ region, simulation results quantitatively reproduce many of the phenomenon observed experimentally by Hunt et al (18), Evesque(14) and Clement (17). A threshold exists between $1.2g$ and $2g$, below which the bed is densely packed and no fluidization is observed. A fluidized region near the surface appears at $\Gamma \cong 2g$, which grows downwards as Γ is increased. The bed experiences a large upward expansion for $2g \leq \Gamma \leq 3.6g$ and then its height remains fairly constant thereafter. The maximum solids fraction occurs several layers above the vibrating floor where particles are physically overburdened, and where granular temperature is a minimum. At the surface where the solids fraction is low, the granular temperature is high.

A dramatic behavioral change occurs when high shaking acceleration is applied. The strongest fluidization appears at bottom, promoting a highly dense packing at the surface. Simulation results show a good agreement with the kinetic theory predictions of Richman and Martin (46). A maximum granular temperature and low solids fraction region is maintained near the vibrating floor, with temperature decreasing monotonically and solids fraction exhibiting a peak at an intermediate depth.

Another measure of the behavior of the bed as a function of Γ is provided by the velocity autocorrelation functions and self-diffusivity. At high Γ, all three components of the velocity autocorrelaion function are exponentially decaying, thereby exhibiting a relaxation time. The tails for the x and z components are very smooth with the component in the direction of shaking (i.e., y component) showing some small fluctuations. The self-diffusion coefficient calculated from these autocorrelation functions are very close to that computed from analytical expression derived from kinetic theory by Savage (23), and that measured from the limiting slope of mean-square displacement curve suggested by Einstein relation (3-3-5). In contrast, at low Γ values, the y component of velocity autocorrelation function is not an exponentially decaying function, but oscillates about zero with a frequency equal to that of the vibrating floor. Hence, there is a strong coupling of the vertical movement of the granular mass with the floor. The other two components of the autocorrelation function do exhibit a relaxation time with smooth tails, indicating a minimal sensitivity to the floor.

Frictional beds are simulated in a primary computational cell having fixed solid plane side walls, a flat vibrating floor and lateral periodic boundaries. Results show that convection in granular vibrating bed is a conditional phenomena, whereby particles move downwards in a narrow stream near the side walls, and rise upwards in the center of the cell (6*d*~20*d*) A sufficiently large amplitude and acceleration is necessary to create a convective flow, while the friction of spheres and walls influence the strength and direction of the circulation. A reversed convection flow pattern is observed when particles are smooth and walls are highly frictional (*fmu* = 0, *fmub* = 0.8)). Also, a low sphere restitution coefficient is found to promote the convection. In a wide computational cell (~100*d*), the convective flow is confined to a narrow region adjacent to the side walls.

Convection is weak and appears unstable in the center of the cell, where a striking phenomenon of the formation and break-up of arches occurs.

Simulations in which convection occurs faithfully reproduce the particle transport phenomenon observed by Knight et al. (37). All particles ascend to the top at about the same speed. A single large sphere becomes "trapped" on the surface by failing to join in the narrow downward stream of small particles near the side walls. It is found that the peak in coordination number curve of large sphere is highly correlated with the peak in the large particle velocity history.

Coupling between granular beds and the vibrating floor is examined by spectral analysis methods. Energy is found to attenuate from the bottom as expected. In a smooth bed, the frequency of mean velocity through the depth remains the same as that of the floor with a phase delay. In a frictional bed, the frequency of mean velocity versus depth is much lower than the floor frequency.

In summary, we have presented particle dynamics simulations to investigate the behavior of vibrated systems of smooth and frictional spheres. Our model has produced, in accordance with experimental observations of Hunt et al. and Knight et al., the phenomenon in which the bed experiences either expansion or convection motion. In addition, good agreement of computed granular temperature, solids fraction profiles and diffusion coefficients with recent kinetic theory predictions of Richman et al. and Savage et al. was found in a high acceleration region where the bed is sufficiently thermalized.

The work which has been discussed in this dissertation provides strong direction and motivation for continued detailed studies. Several problems and striking phenomena have been revealed which easily lend themselves to further investigations.

(1). Investigate the microstructure change at different shaking phase angles, using 3-D Voronoi diagram.

(2). Calculate the self-diffusion tensor by following the system dyanimcs over a long time.

3). Study wave propagation through the bed and in granular materials by considering the phase delay of the velocity cross-correlation functions.

(4). Simulate the vibrating transport of granular beds.

(5). Further study the segregation phenomenon in vibating beds by performing amicrostructural analysis of diagnostic quantities.

(6) Create 3-D video animations of the simulations which could reveal phenomena not easily observed, such as the formation and breakup of arches and heaping.

APPENDIX

PLOTS

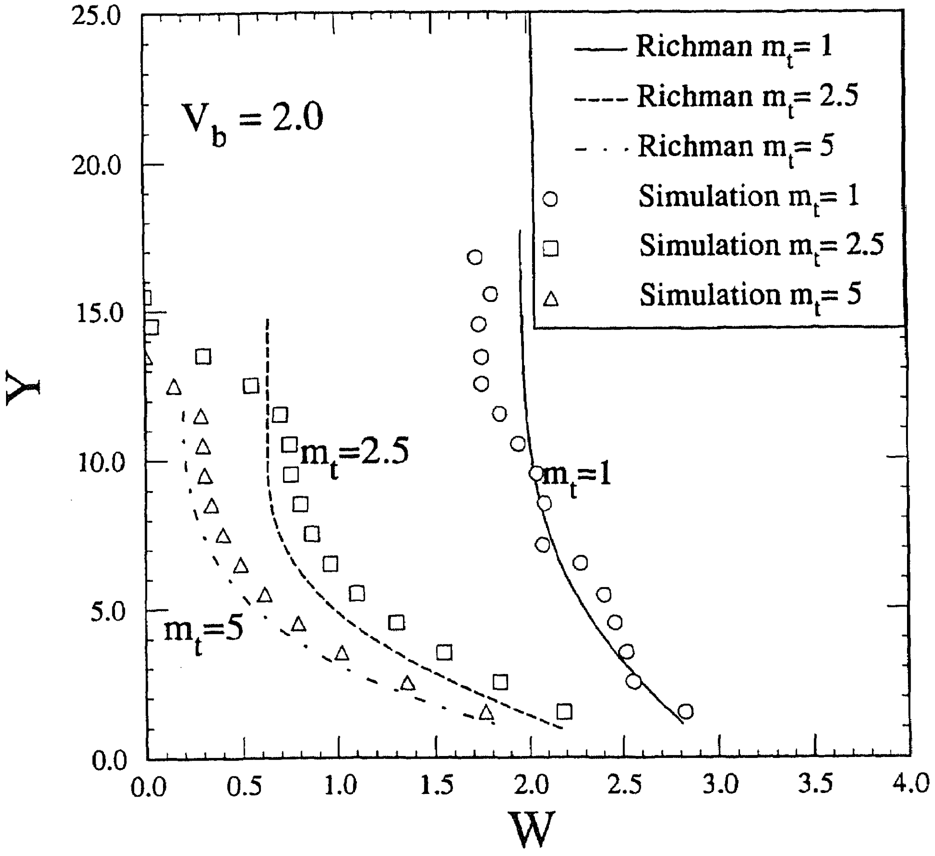

Figure A4.1a Dimensionless granular temperature depth profiles for $V_b = 2.0$ compared with theoretical predictions of Richman and Martin (46).(dotted and solid lines). $d = 0.1m$, $e = 0.9$, $frq. = 50\ Hz$, $K_l = 2.7\times10^8$.

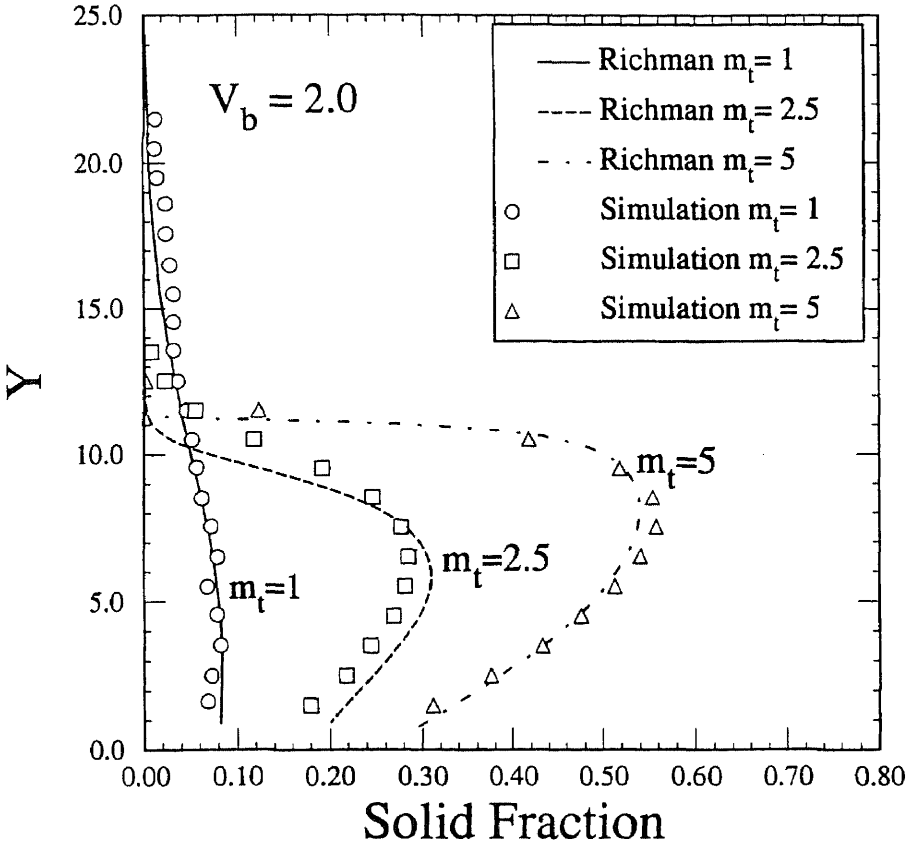

Figure A4.1b Solids fraction depth profiles compared with theoretical predictions of Richman and Martin (46) (dotted and solid lines). $d = 0.1m$, $e = 0.9$, *frq.* = 50 *Hz*, $K_1 = 2.7 \times 10^8$.

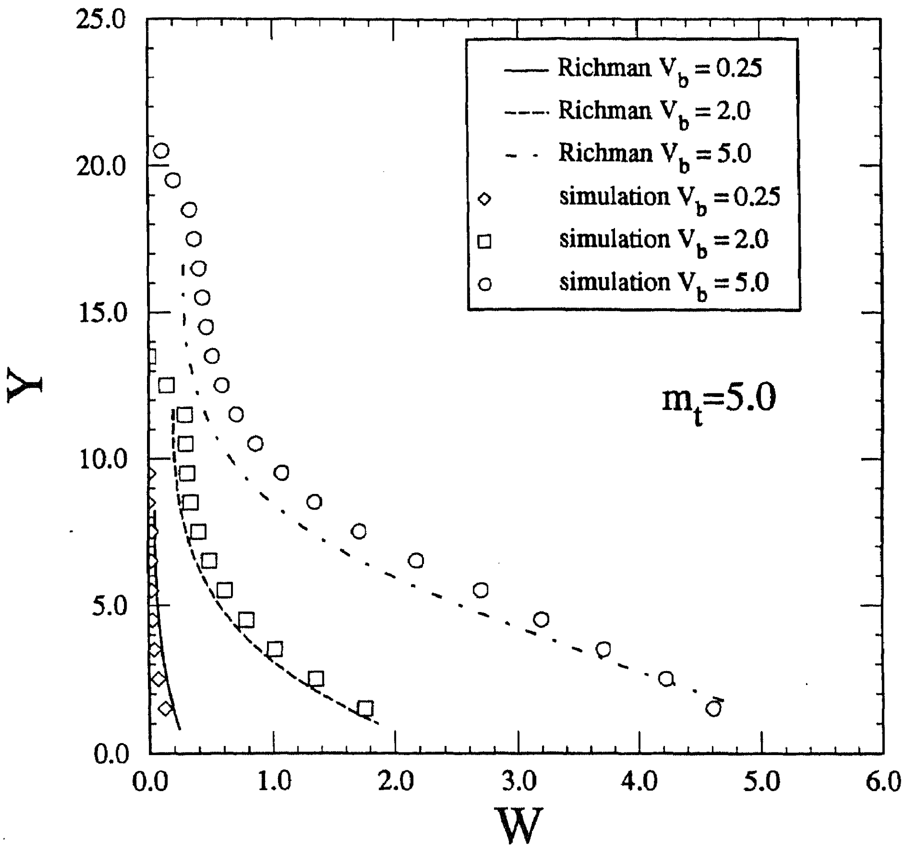

Figure A4.2a Dimensionless granular temperature depth profiles for $m_t = 5.0$ compared with theoretical predictions of Richman and Martin (46).(dotted and solid lines). $d = 0.1m$, $e = 0.9$, $frq. = 50\ Hz$, $K_l = 2.7\times10^8$.

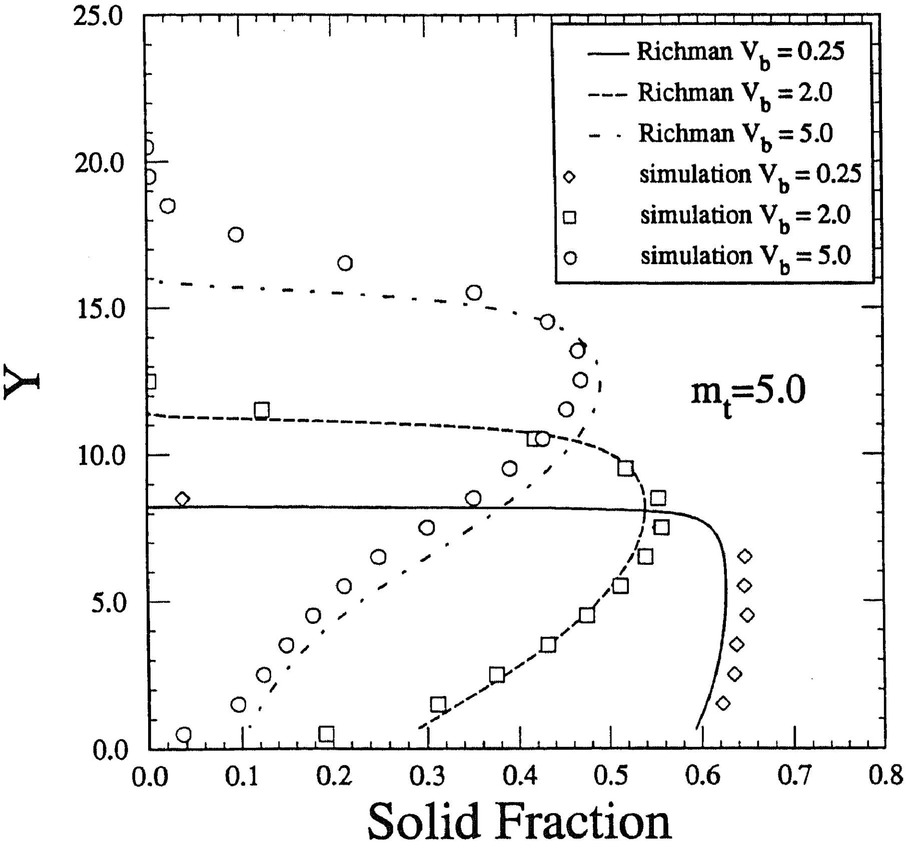

Figure A4.2b Solids fraction depth profiles for m_t = 5.0 compared with theoretical predictions of Richman and Martin (46) (dotted and solid lines). $d = 0.1m$, $e = 0.9$, $frq. = 50\ Hz$, $K_l = 2.7\times10^8$.

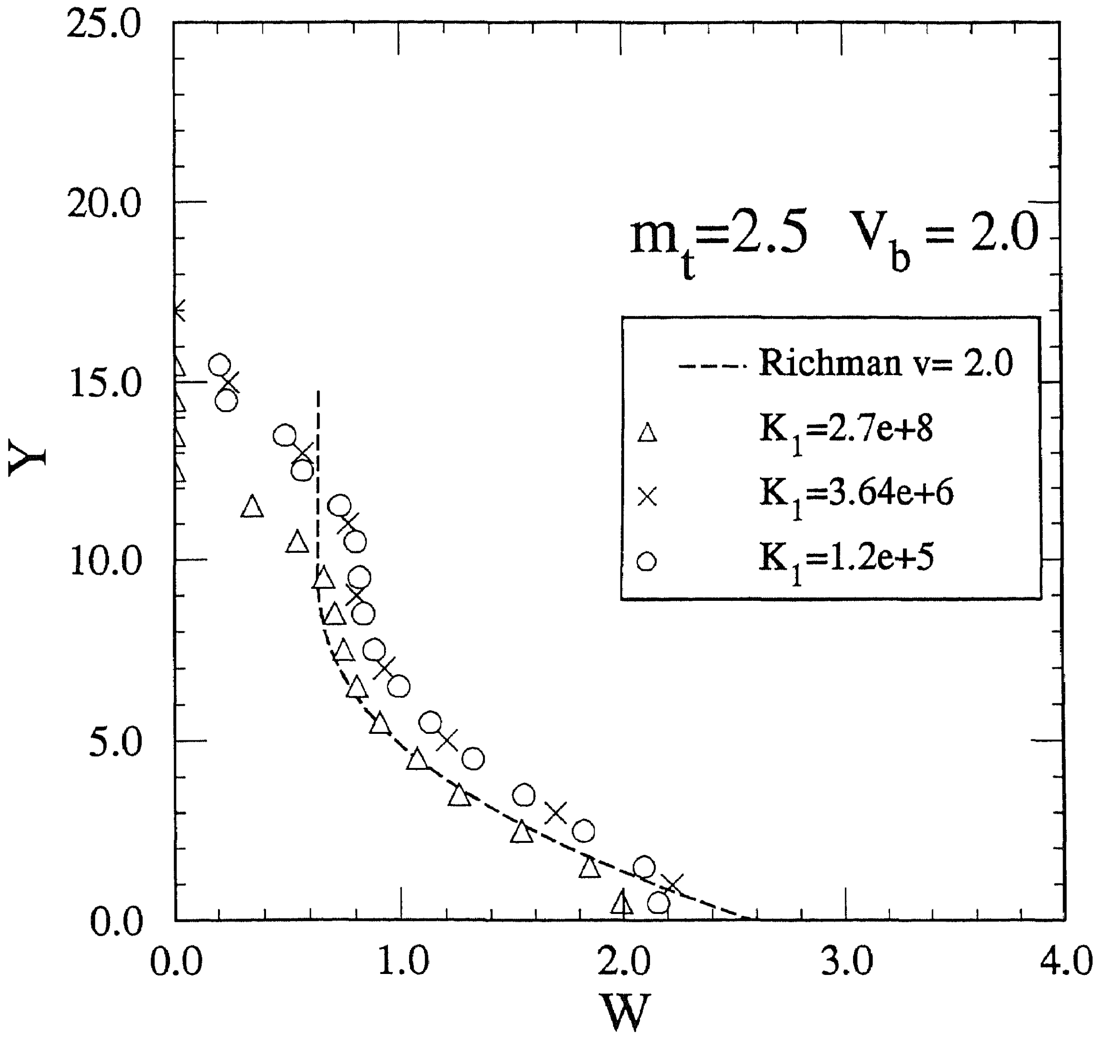

Figure A4.3a Dimensionless granular temperature depth profiles at three different values of normal loading stiffness K_1 and the theoretical predictions of Richman and Martin (46).(dotted line). $d = 0.01m$, $e = 0.9$, *frq.* = 50 *Hz*.

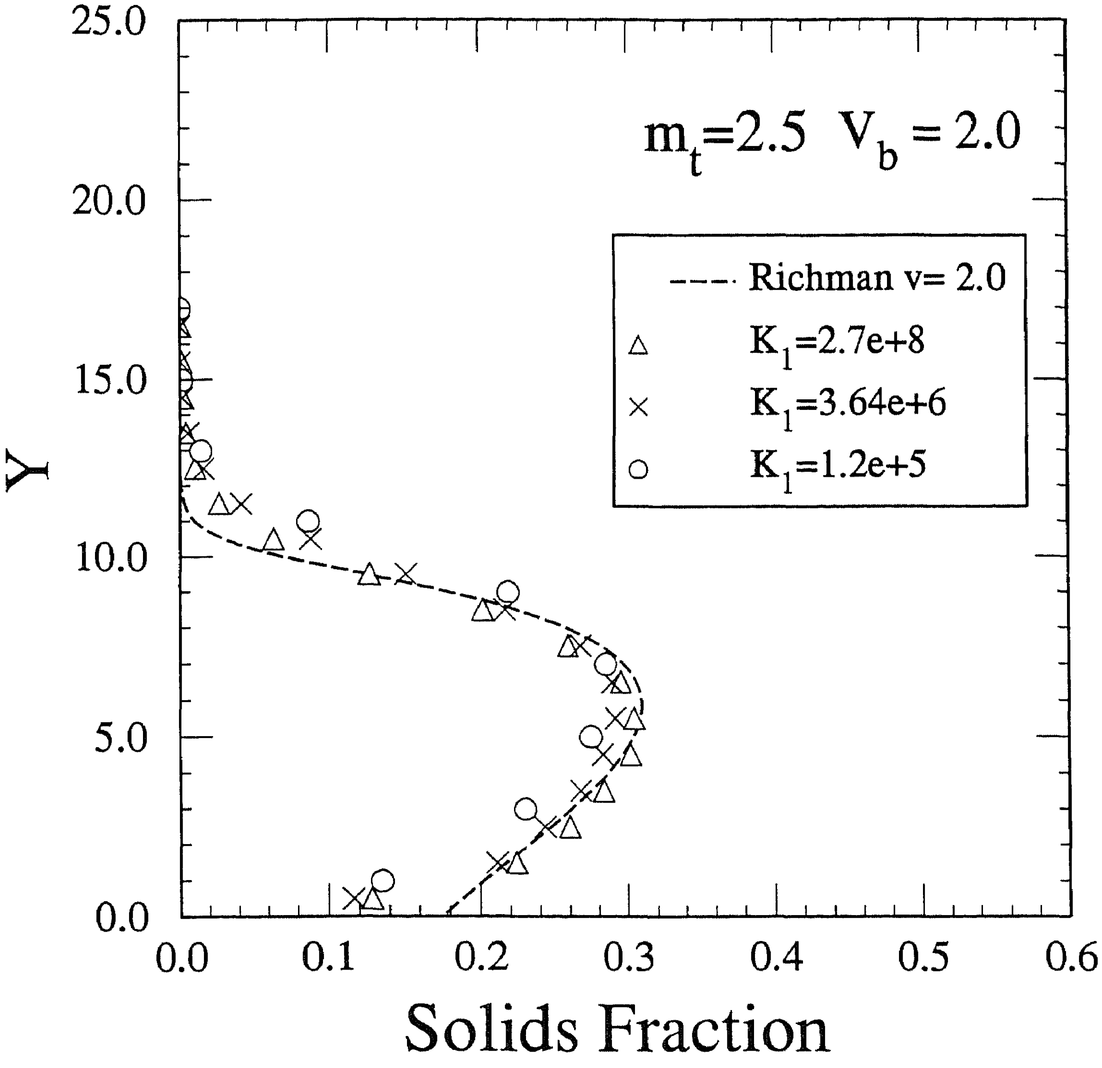

Figure A4.3b Solids fraction depth profiles at three different values of normal loading stiffness K_1 and the theoretical predictions of Richman and Martin (46) (dotted line). $d = 0.01m$, $e = 0.9$, $frq. = 50\ Hz$.

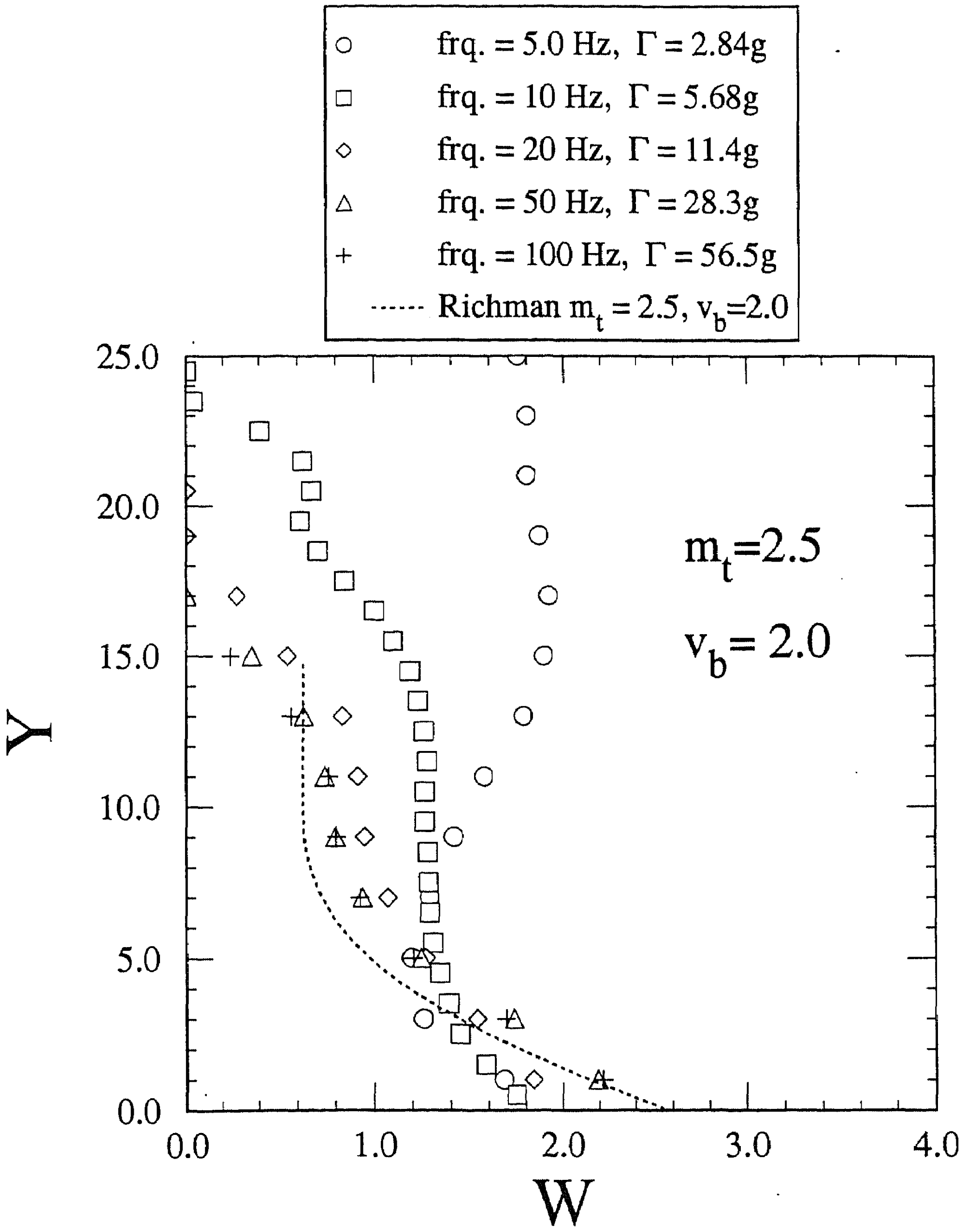

Figure A4.4a Dimensionless granular temperature depth profiles for m_t = 2.5 and V_b = 2.0 over a range of Γ values obtained by varying the frequency of the boundary between 5 and 100 Hz. The dotted line is kinetic prediction of Richman and Martin(46). d = 0.01m, e = 0.9.

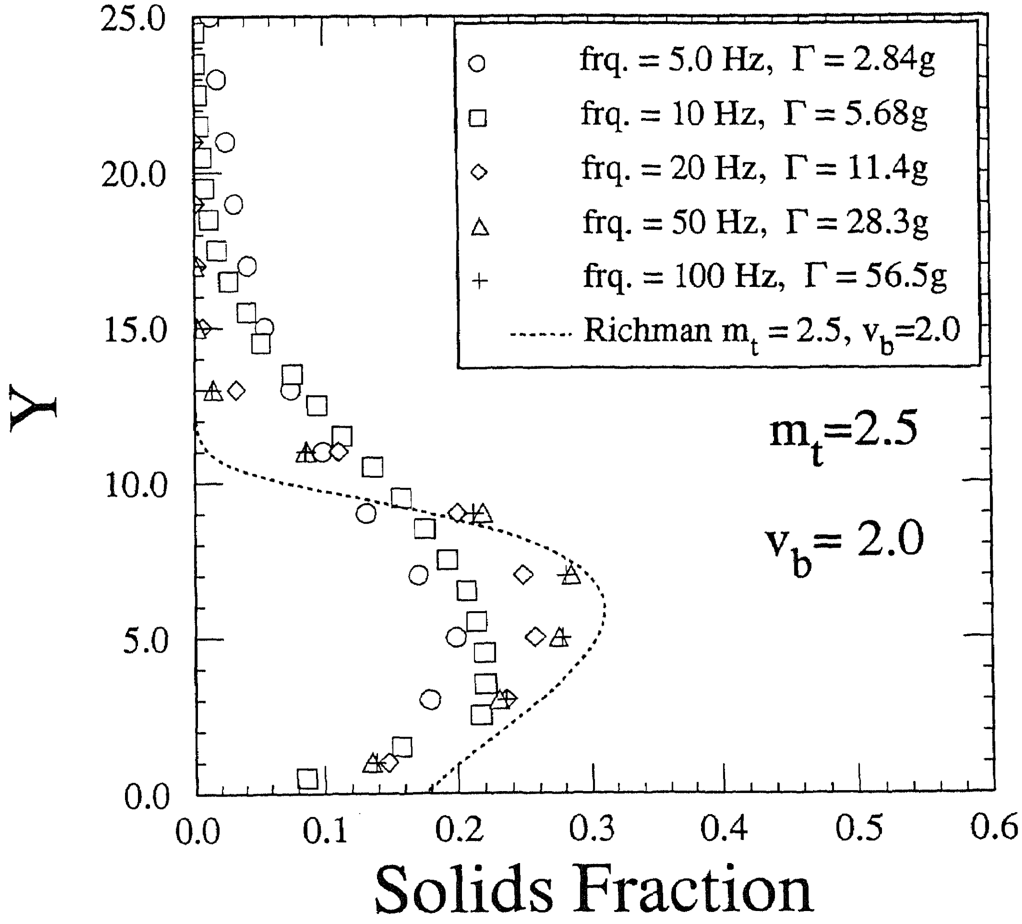

Figure 4.4b Solids fraction depth profiles for $m_t = 2.5$ and $V_b = 2.0$ over a range of Γ values obtained by varying the frequency of the boundary between 5 and 100 Hz.The dotted line is kinetic prediction of Richman and Martin(46). $d = 0.01m$, $e = 0.9$.

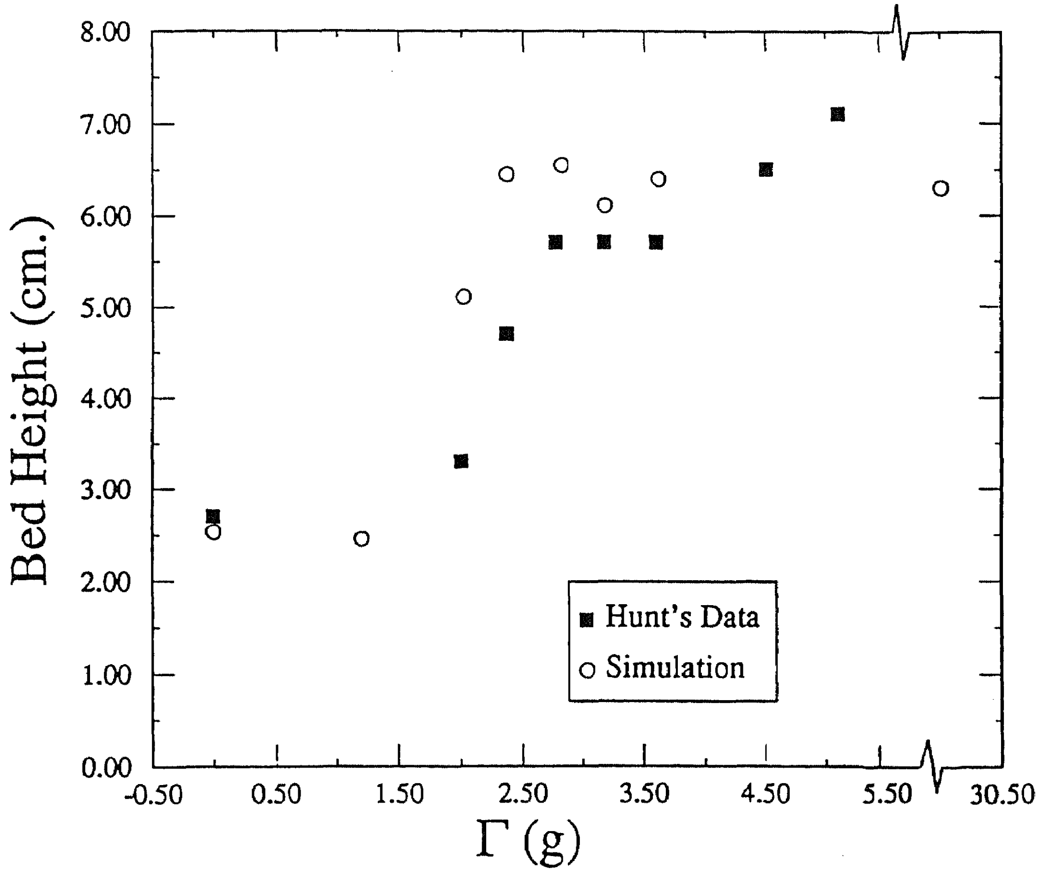

Figure 4.5 Simulated bed height versus Γ compared with experimental results of Hunt et al. (18).

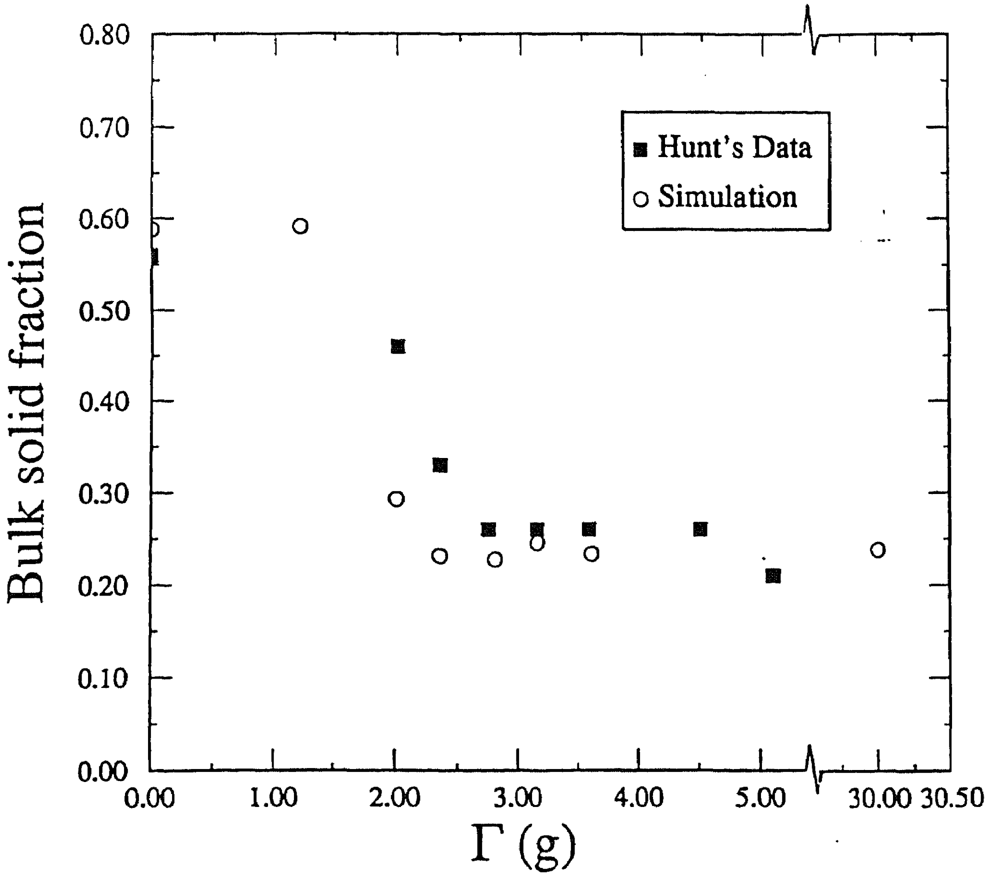

Figure A4.6 Simulated bulk solids fraction versus Γ compared wtih experimental results of Hunt et al. (18).

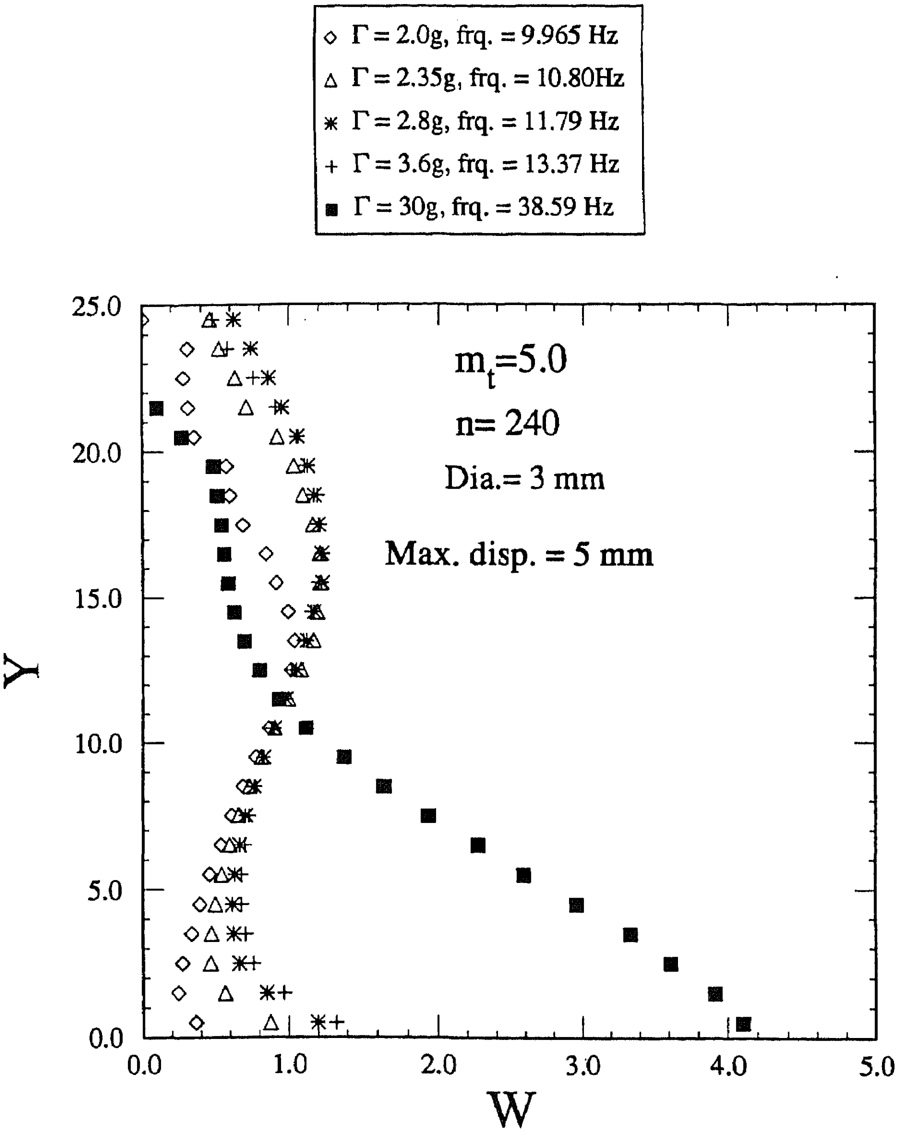

Figure A4.7a Dimensionless granular temperature depth profiles with increasing Γ and a fixed shaking amplitude equal to 1.67*d*. $e = 0.9$.

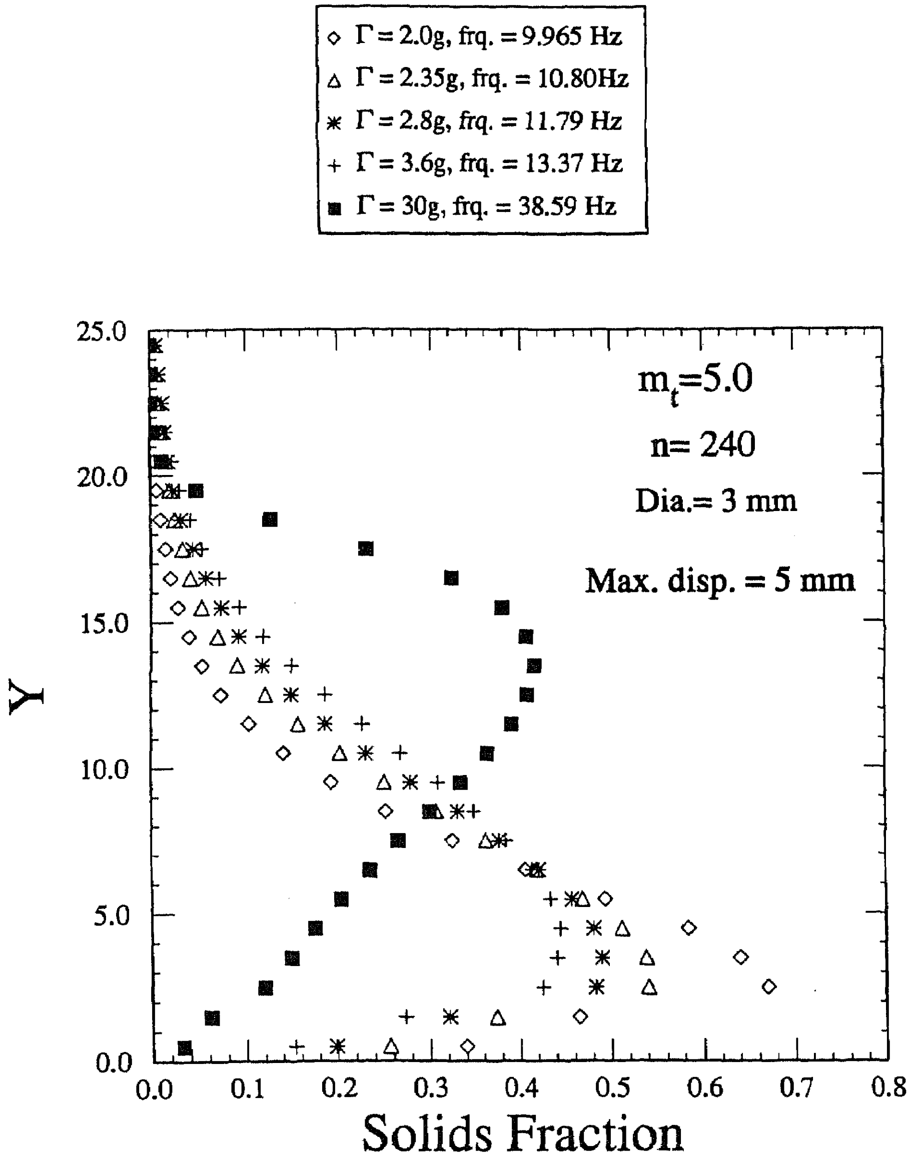

Figure A4.7b Solids fraction depth profiles with increasing Γ and a fixed shaking amplitude equal to 1.67*d*. *e* = 0.9.

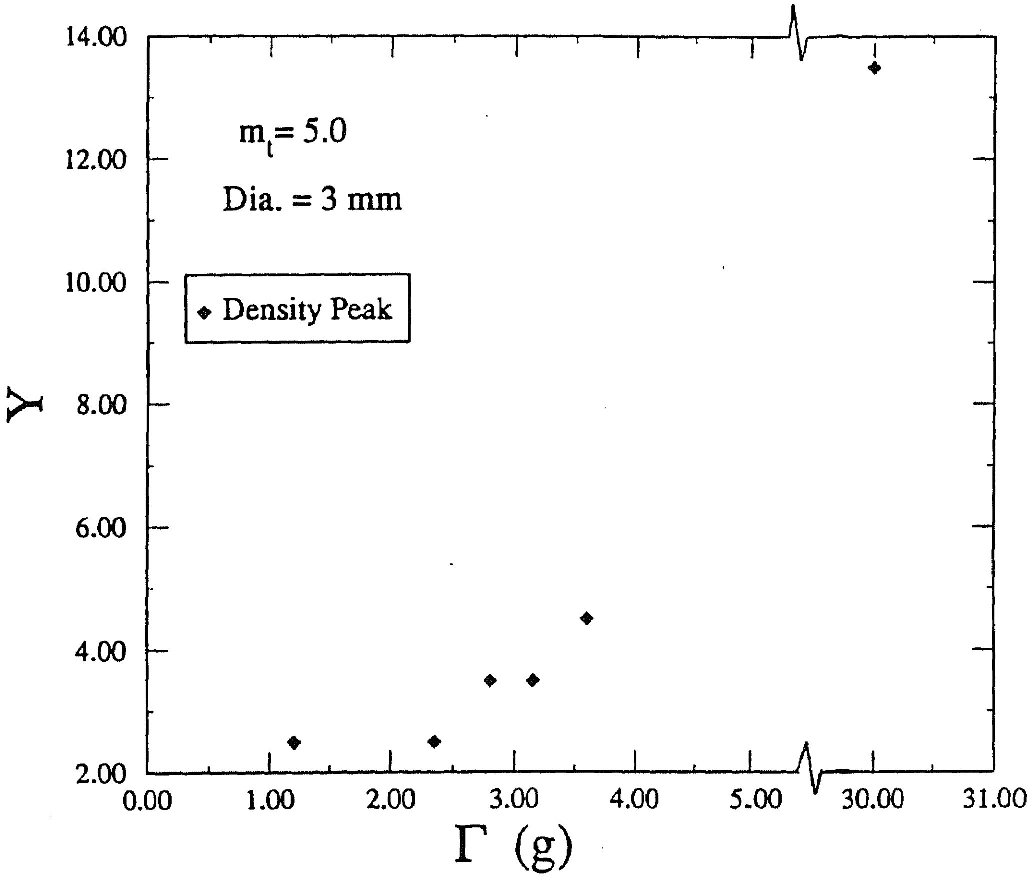

Figure A4.8 Normalized y coordinate ($Y = y/d$) at which peak in solids fraction profile occurs as a function of the acceleration amplitude Γ.

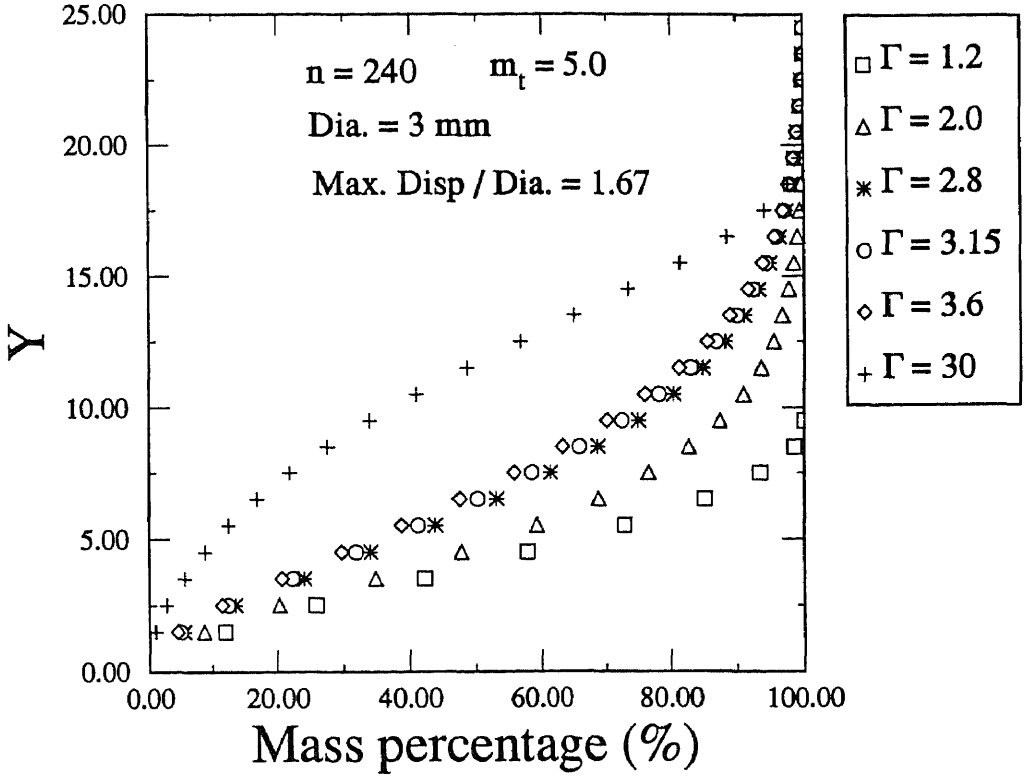

Figure A4.9 Mass percentage below normalized bed location *Y* at different Γ values.

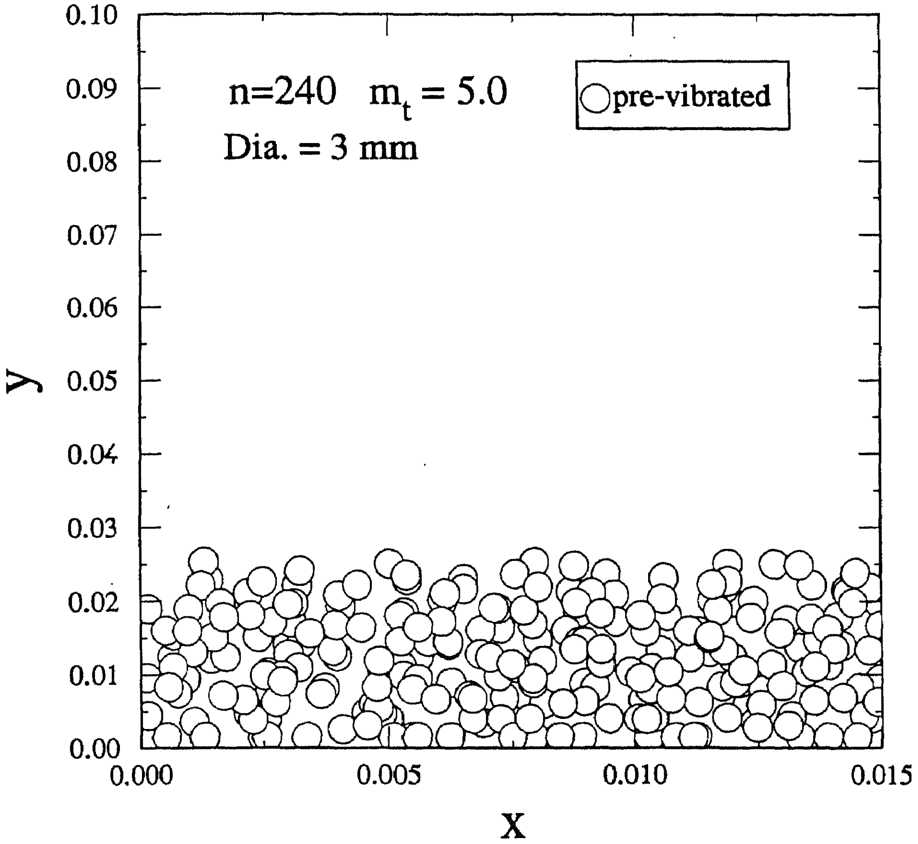

Figure A4.10a Projection of reduced spheres onto *x*-*y* plane before shaking (at t =0).

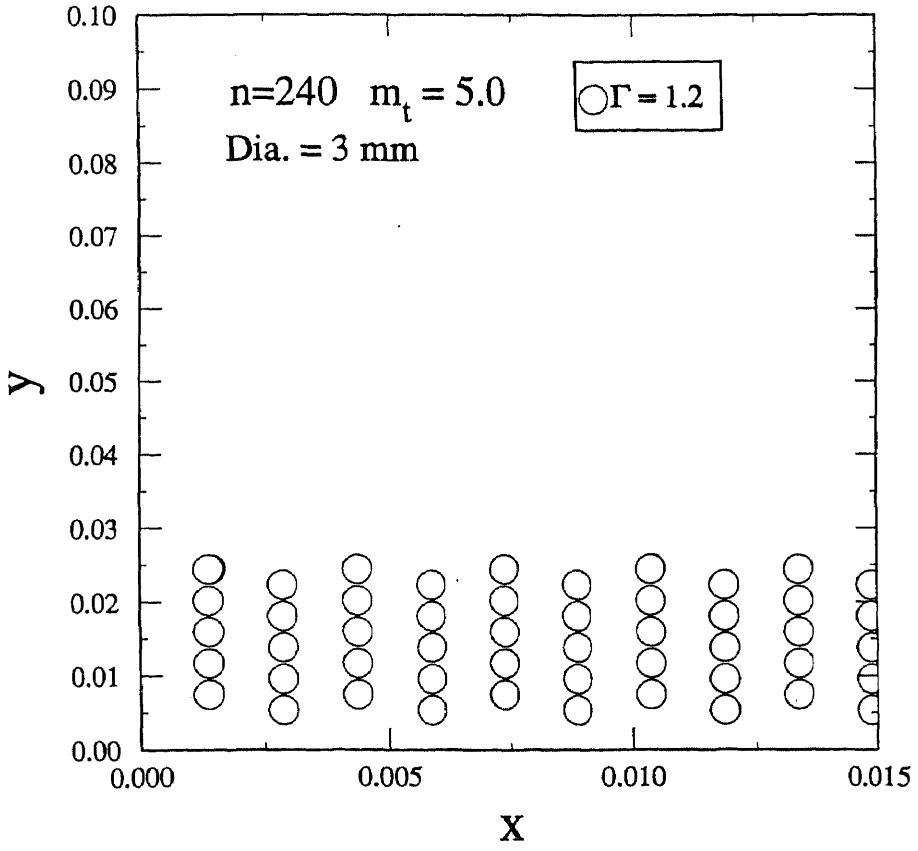

Figure A4.10b Snap of projection of reduced spheres onto *x-y* plane for Γ = 1.2*g*.

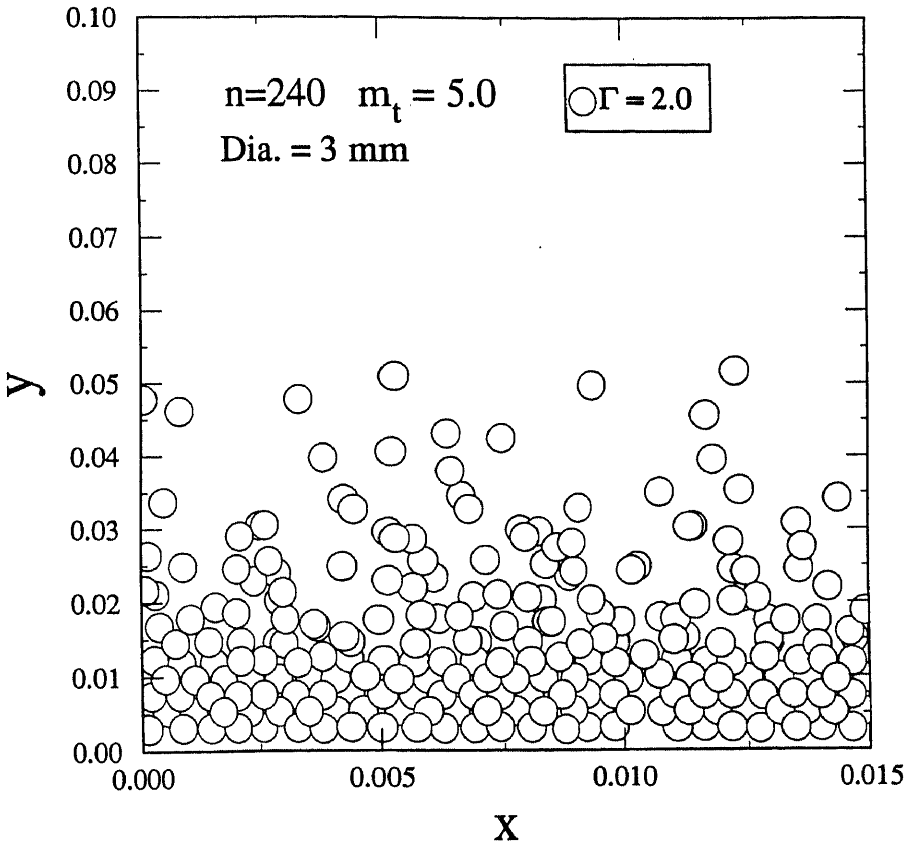

Figure A4.10c Snap of projection of reduced spheres onto x-y plane for $\Gamma = 2g$.

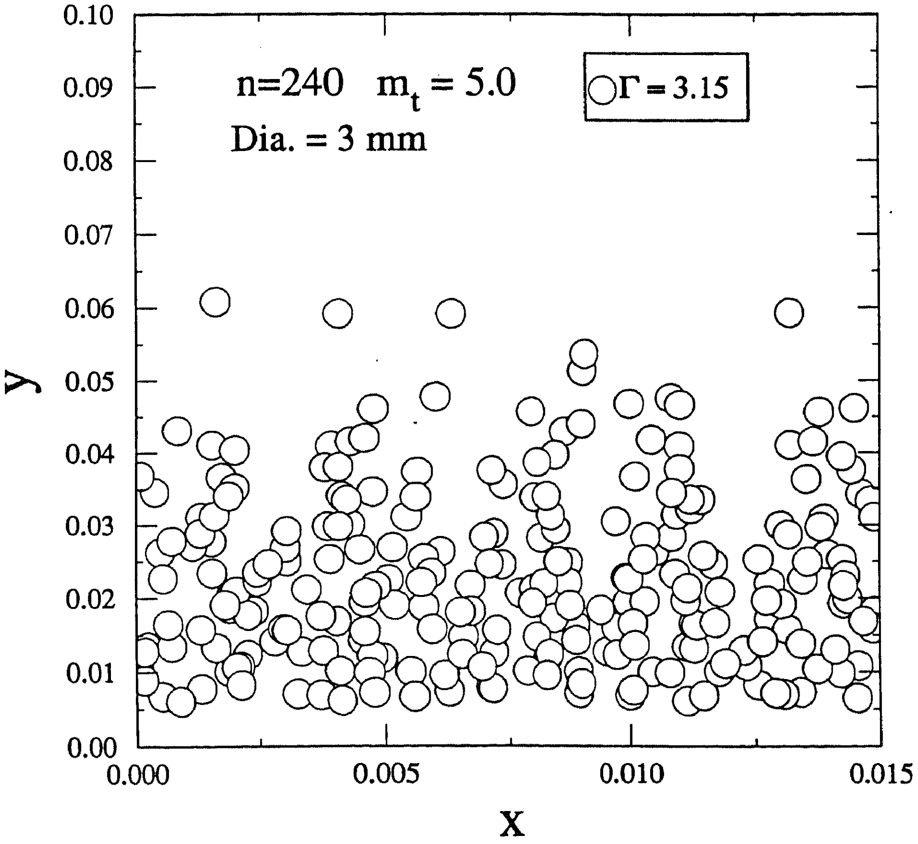

Figure A4.10d Snap of projection of reduced spheres onto x-y plane for $\Gamma = 3.15g$.

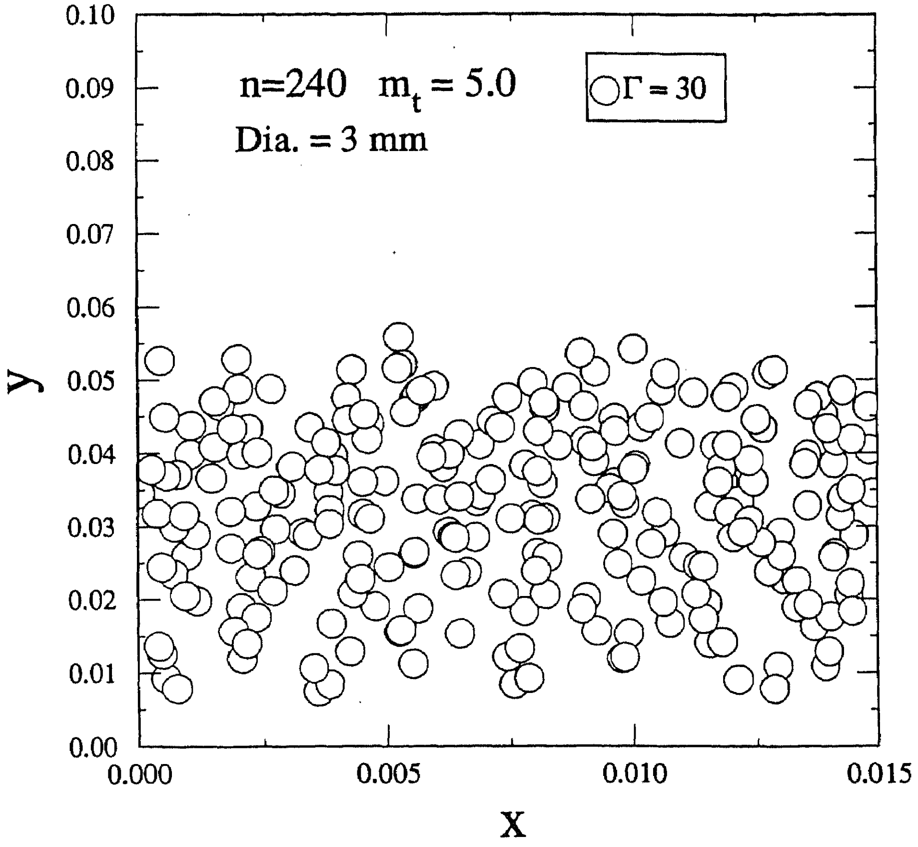

Figure A4.10e Snap of projection of reduced spheres onto *x*-*y* plane for Γ = 30*g*.

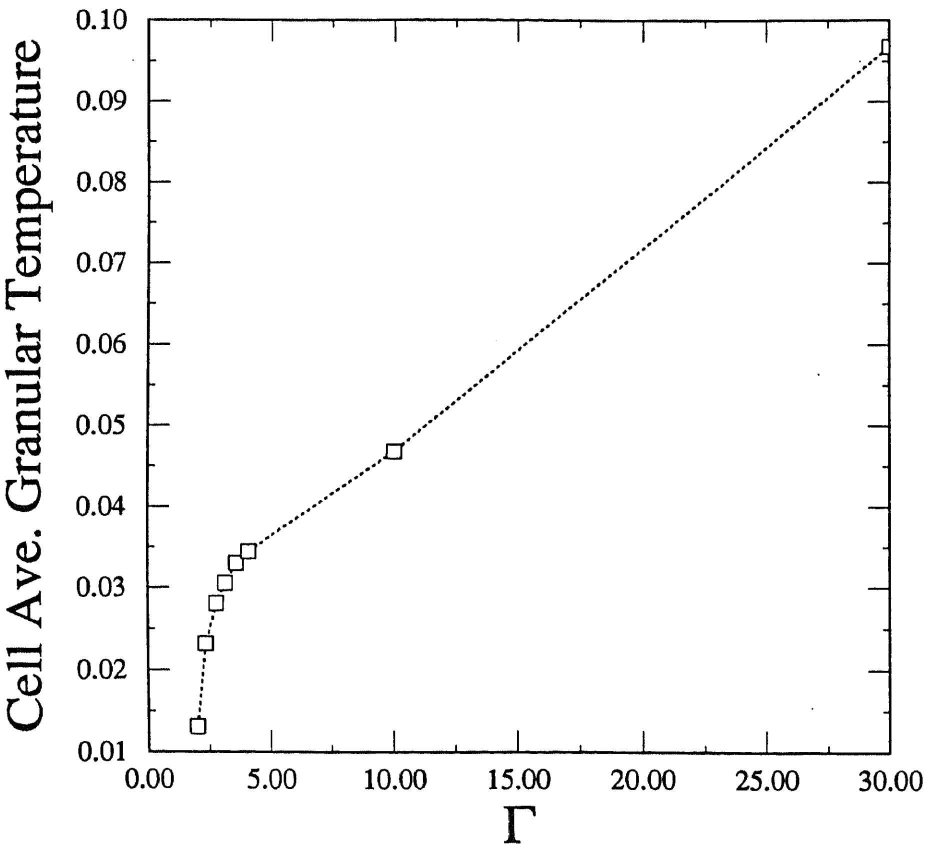

Figure A4.11 Mean granular temperature in primary computation cell versus Γ.(average over 20 seconds after the system reaching a steady state)

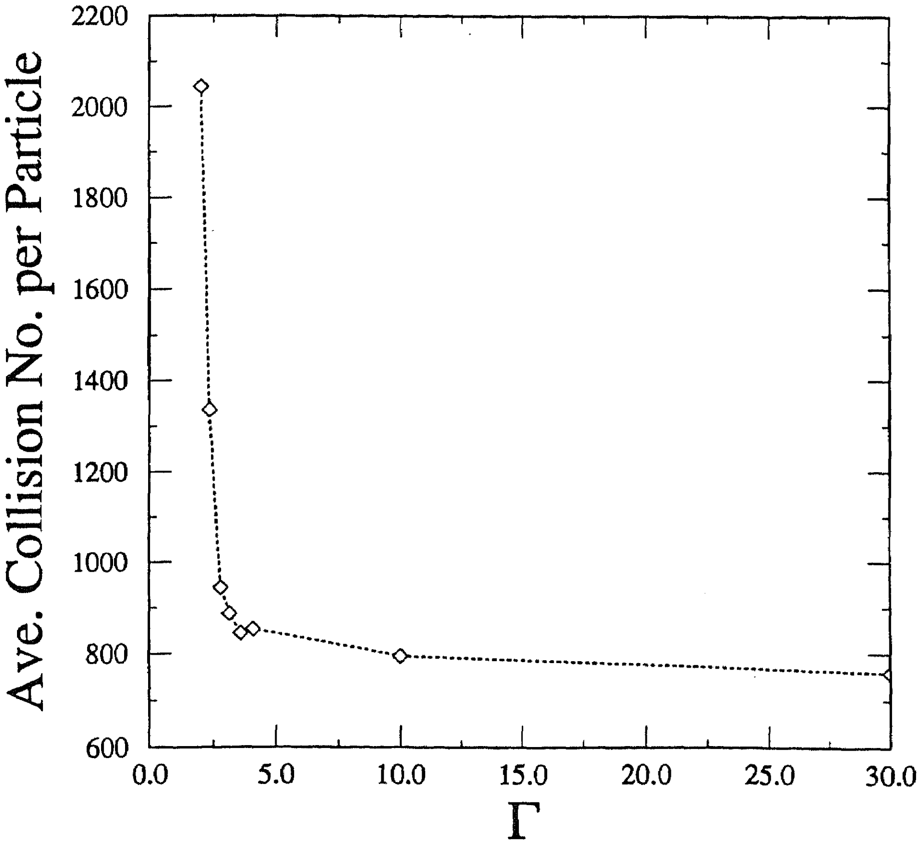

Figure A4.12 Mean collisions per particle versus Γ.(average over 20 seconds after the system reaching a steady state)

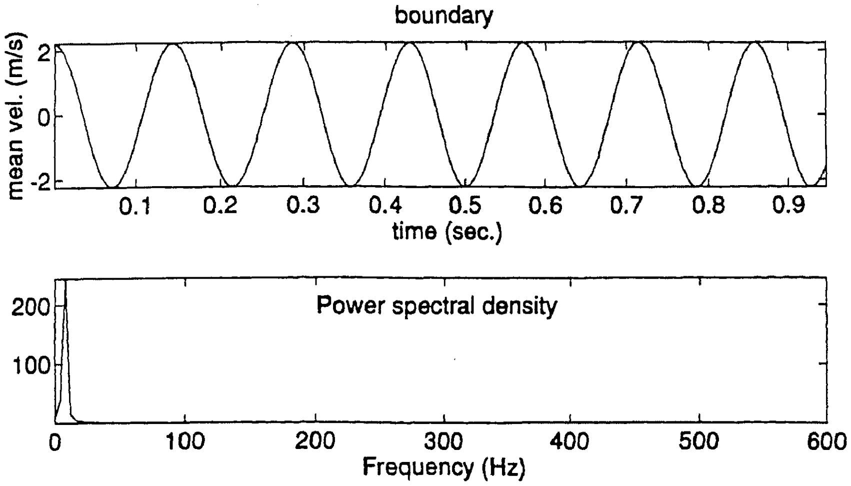

Figure A4.13a Boundary velocity (frq. = 7 Hz) and its spectral density of a system where $m_t = 5$, $\Gamma = 10g$, $d = 0.1m$, displacement amplitude = 0.5d, $\Gamma = 10d$, $e = 0.9$, $K_1 = 2.8 \times 10^6$, $\rho = 1200\ kg/m^3$.

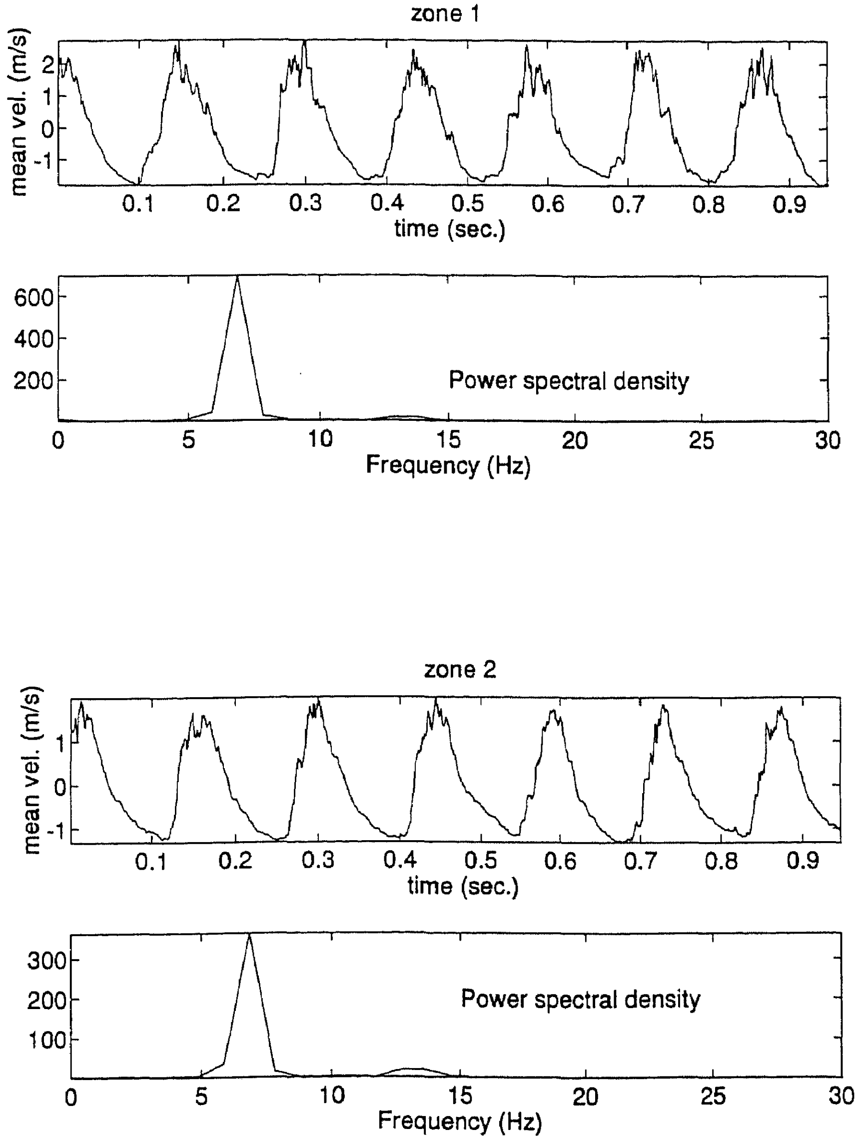

Figure A4.13b Time histories of y-components of the mean zone velocities and their power spectral densities in Zone 1 and 2. Zones are sequentially numbered starting from 1 near the vibrating floor. m_t = 5, d = 0.1m, shaking amplitude = 0.5d, Γ = 10g, e= 0.9, $K_1 = 2.8 \times 10^6$, ρ = 1200 kg/m^3.

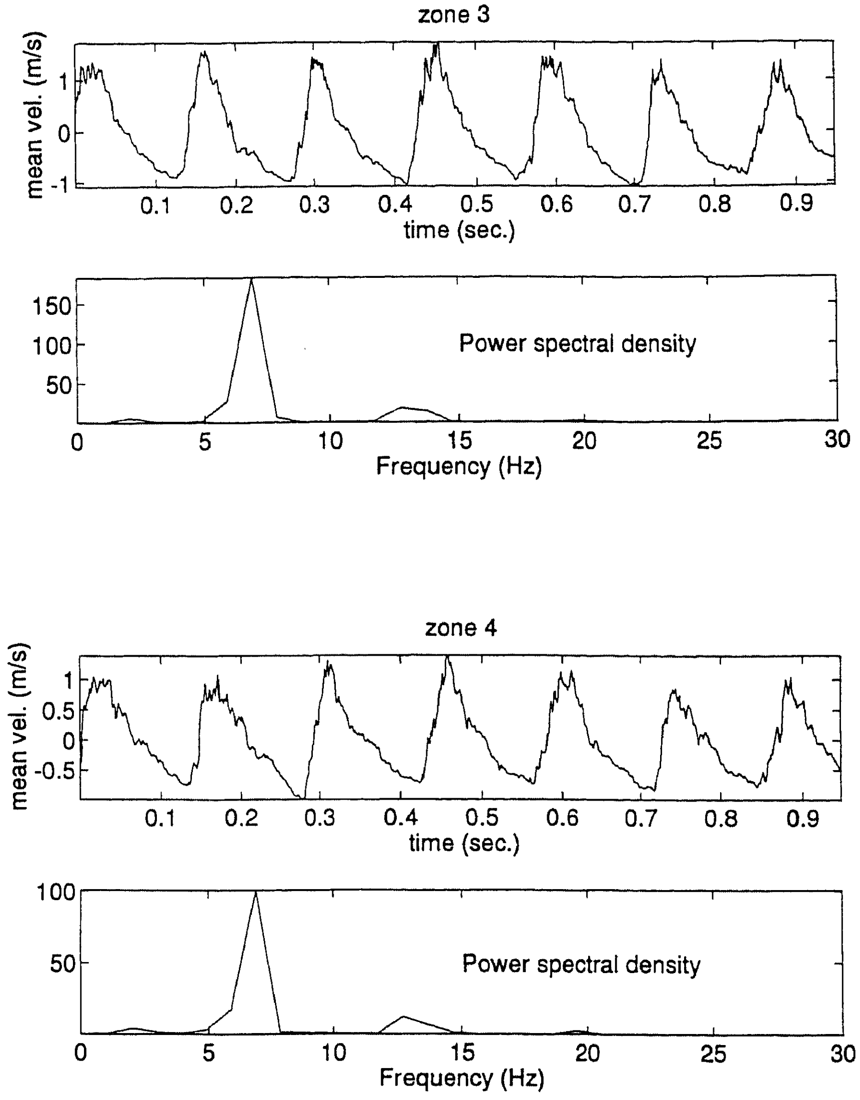

Figure A4.13b Time histories of *y*-components of the mean zone velocities and their power spectral densities in Zone 3 and 4. Zones are sequentially numbered starting from 1 near the vibrating floor. $m_t = 5$, $d = 0.1\text{m}$, shaking amplitude = 0.5d, $\Gamma = 10g$, $e = 0.9$, $K_l = 2.8 \times 10^6$, $\rho = 1200\ kg/m^3$.

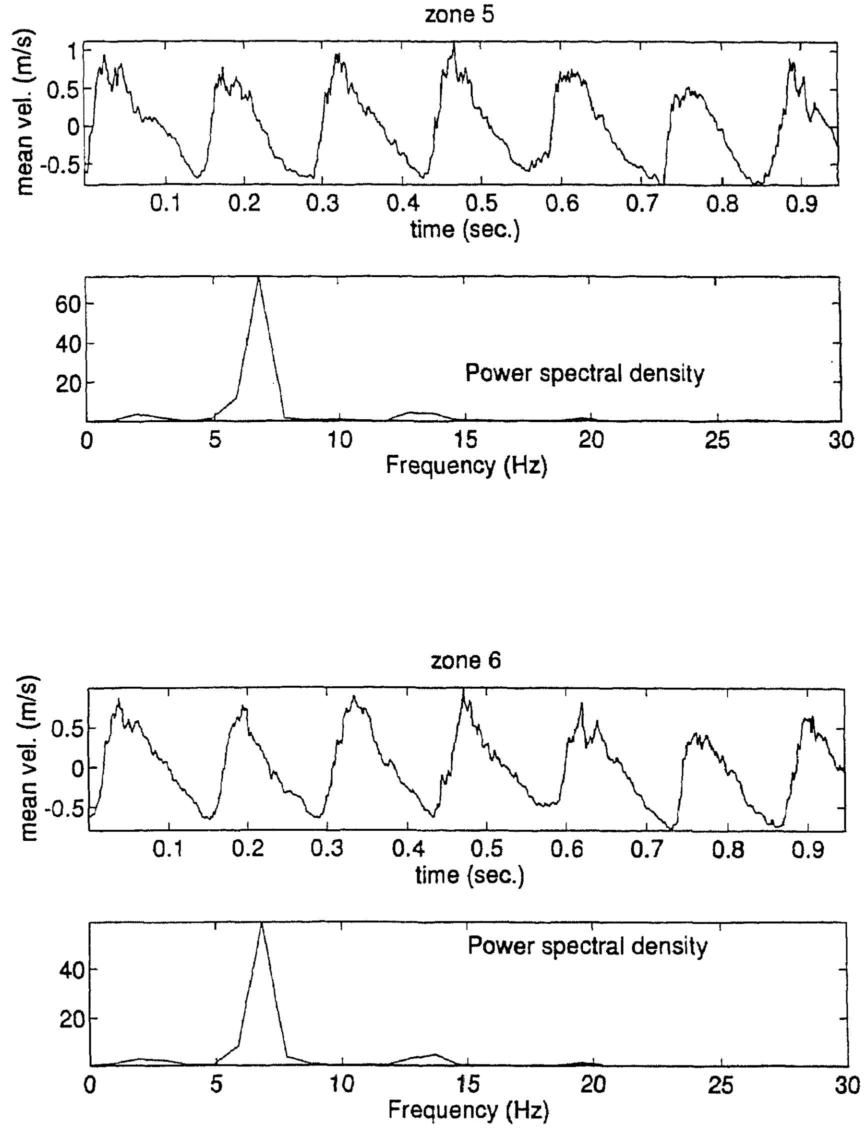

Figure A4.13b Time histories of *y*-components of the mean zone velocities and their power spectral densities in Zone 5. and 6. Zones are sequentially numbered starting from 1 near the vibrating floor. $m_t = 5$, $d = 0.1$m, shaking amplitude =.5d, $\Gamma = 10$g, $e = 0.9$, $K_1 = 2.8 \times 10^6$, $\rho = 1200\ kg/m^3$.

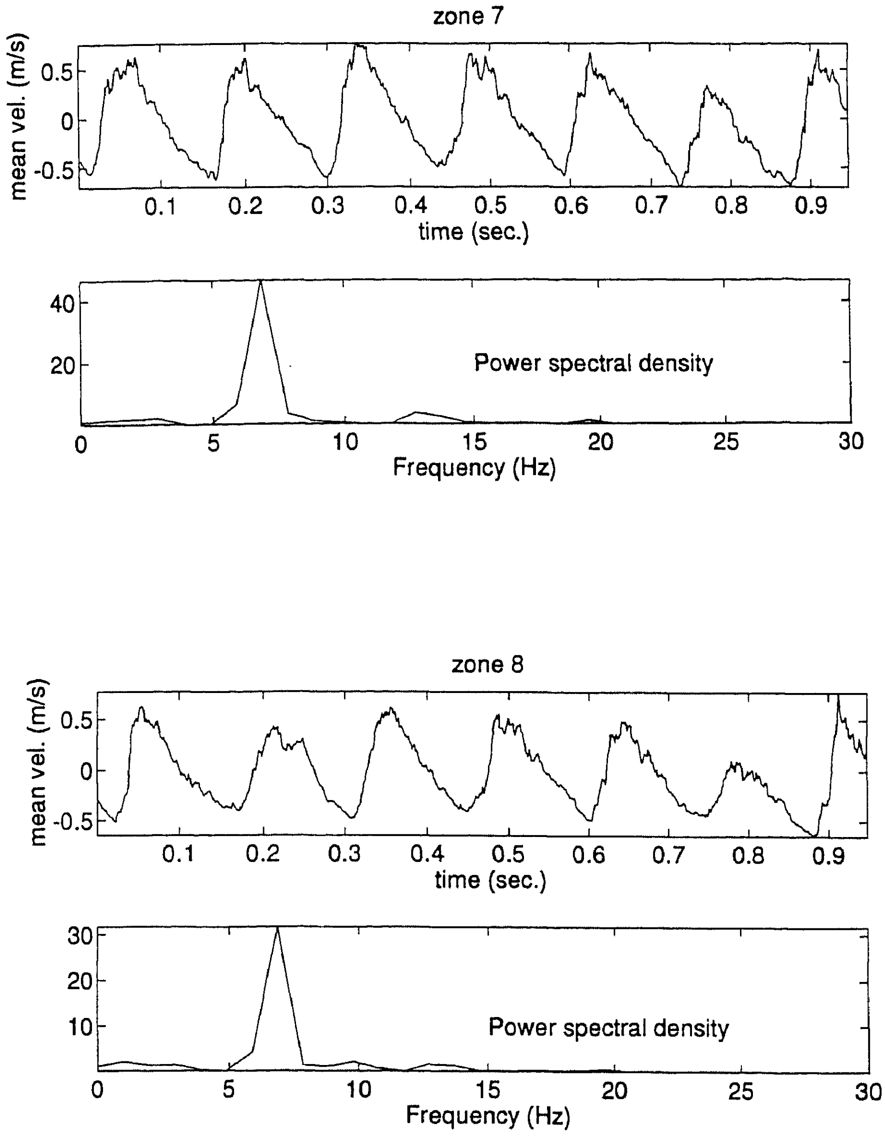

Figure A4.13b Time histories of y-components of the mean zone velocities and their power spectral densities in Zone 7 and 8. Zones are sequentially numbered starting from 1 near the vibrating floor. $m_t = 5$, $d = 0.1$m, shaking amplitude =.5d, $\Gamma = 10g$, $e = 0.9$, $K_1 = 2.8 \times 10^6$, $\rho = 1200\ kg/m^3$.

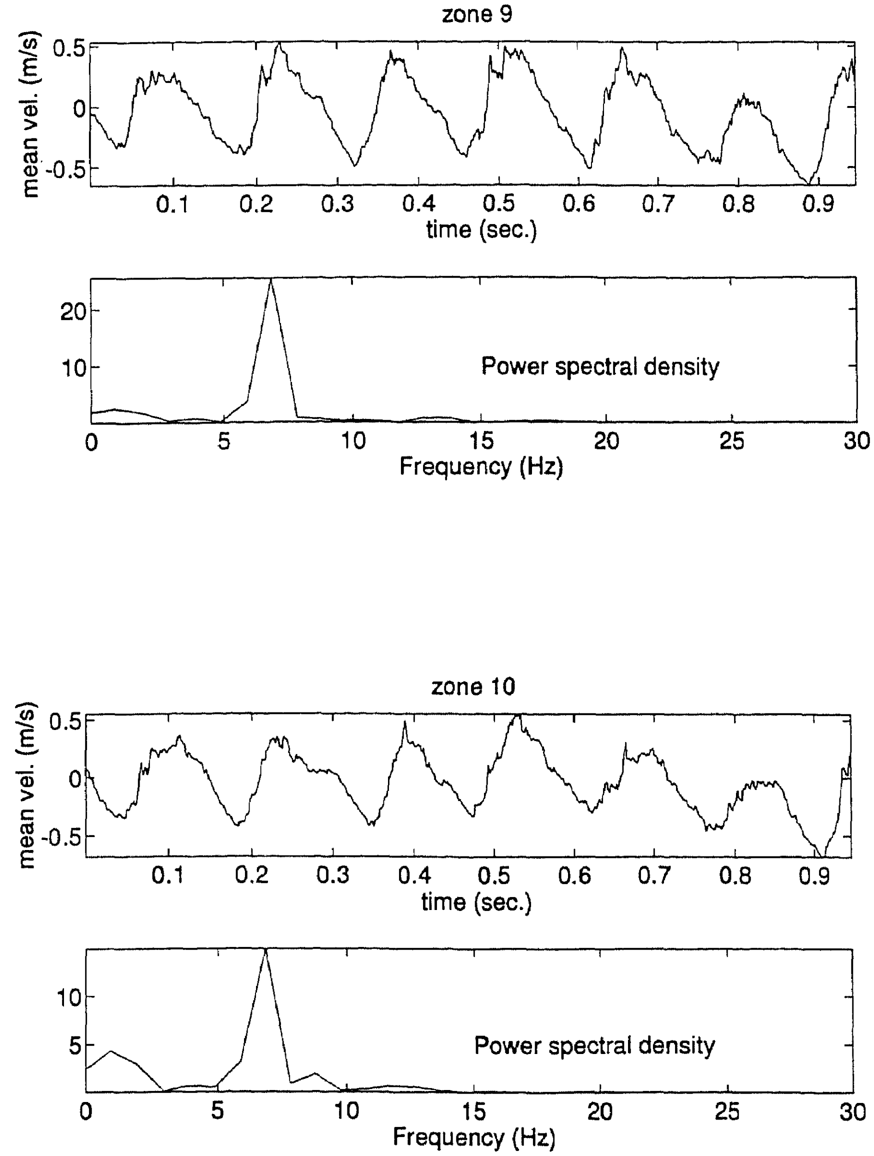

Figure A4.13b Time histories of y-components of the mean zone velocities and their power spectral densities in Zone 9 and 10. Zones are sequentially numbered starting from 1 near the vibrating floor. $m_t = 5$, $d = 0.1$m, shaking amplitude =.5d, $\Gamma = 10g$, $e = 0.9$, $K_l = 2.8 \times 10^6$, $\rho = 1200\ kg/m^3$.

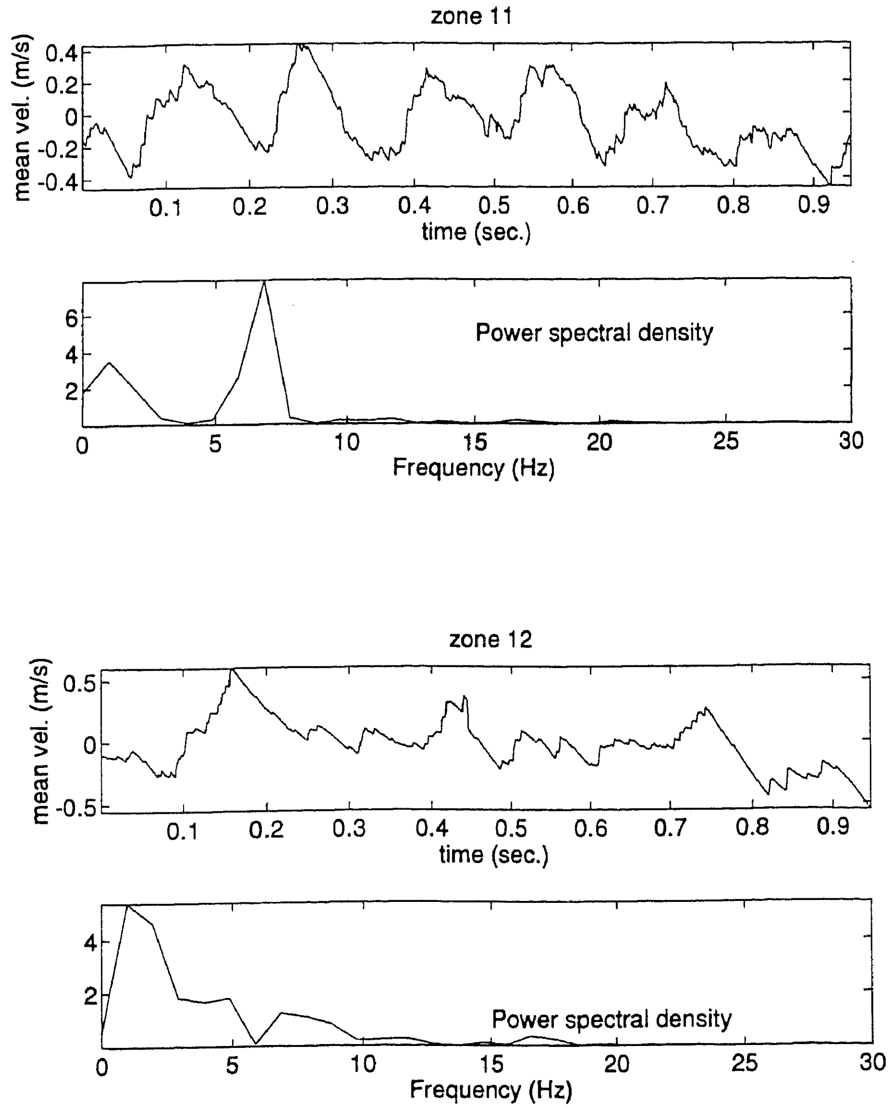

Figure A4.13b Time histories of y-components of the mean zone velocities and their power spectral densities in Zone 11 and 12. Zones are sequentially numbered starting from 1 near the vibrating floor. $m_t = 5$, $d =$ 0.1m, shaking amplitude =.5d, $\Gamma = 10g$, $e= 0.9$, $K_1 = 2.8 \times 10^6$, $\rho = 1200$ kg/m^3.

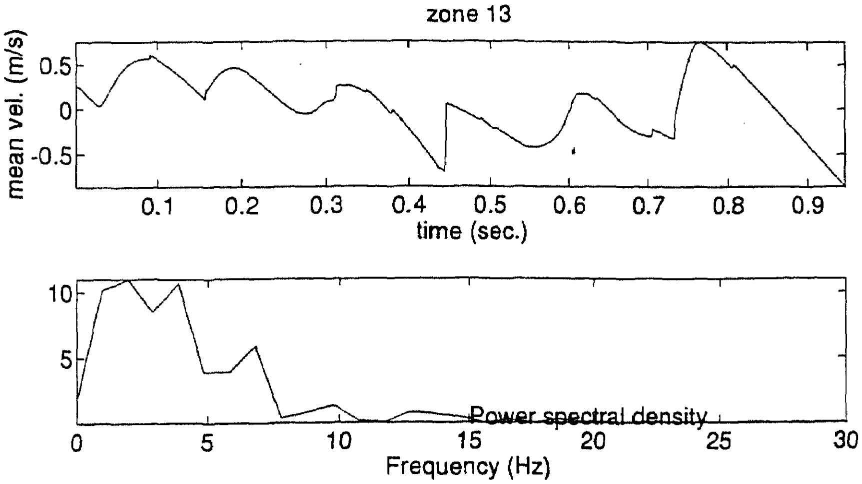

Figure A4.13b Time histories of y-components of the mean zone velocity and its power spectral density in Zone 13. Zones are sequentially numbered starting from 1 near the vibrating floor. $m_t = 5$, $d = 0.1$m, shaking amplitude =.5d, $\Gamma = 10g$, $e = 0.9$, $K_1 = 2.8 \times 10^6$, $\rho = 1200\ kg/m^3$.

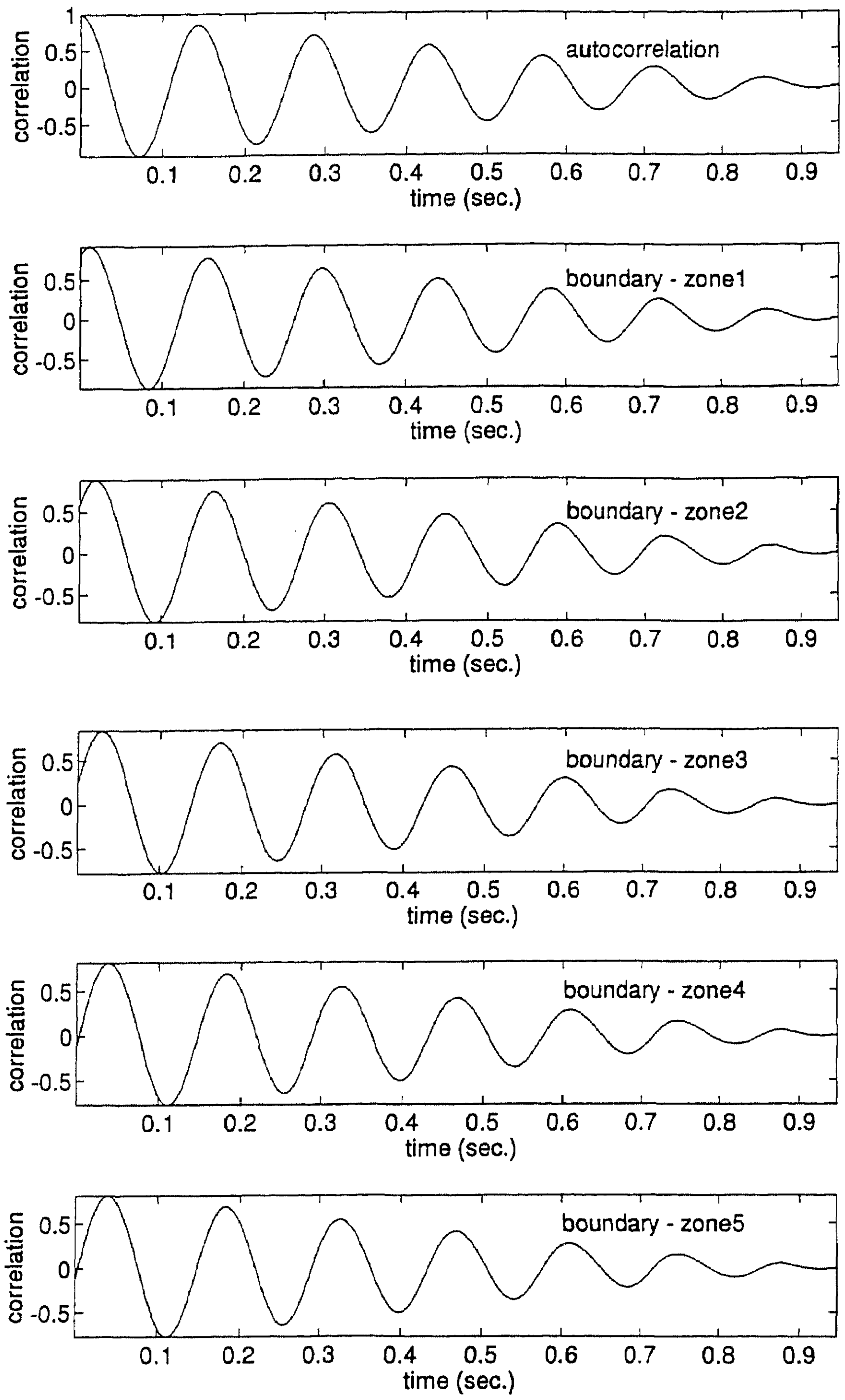

Figure A4.14 Autocorrelation of boundary velocity and cross correlations between the boundary velocity and the y-components of the mean velocity in zone 1 ~zone 5 in a system where $m_t = 5$, $d = 0.1$m, shaking amplitude =.5d, $\Gamma = 10$g, $e= 0.9$, $K_l = 2.8 \times 10^6$, $\rho = 1200$ kg/m^3.

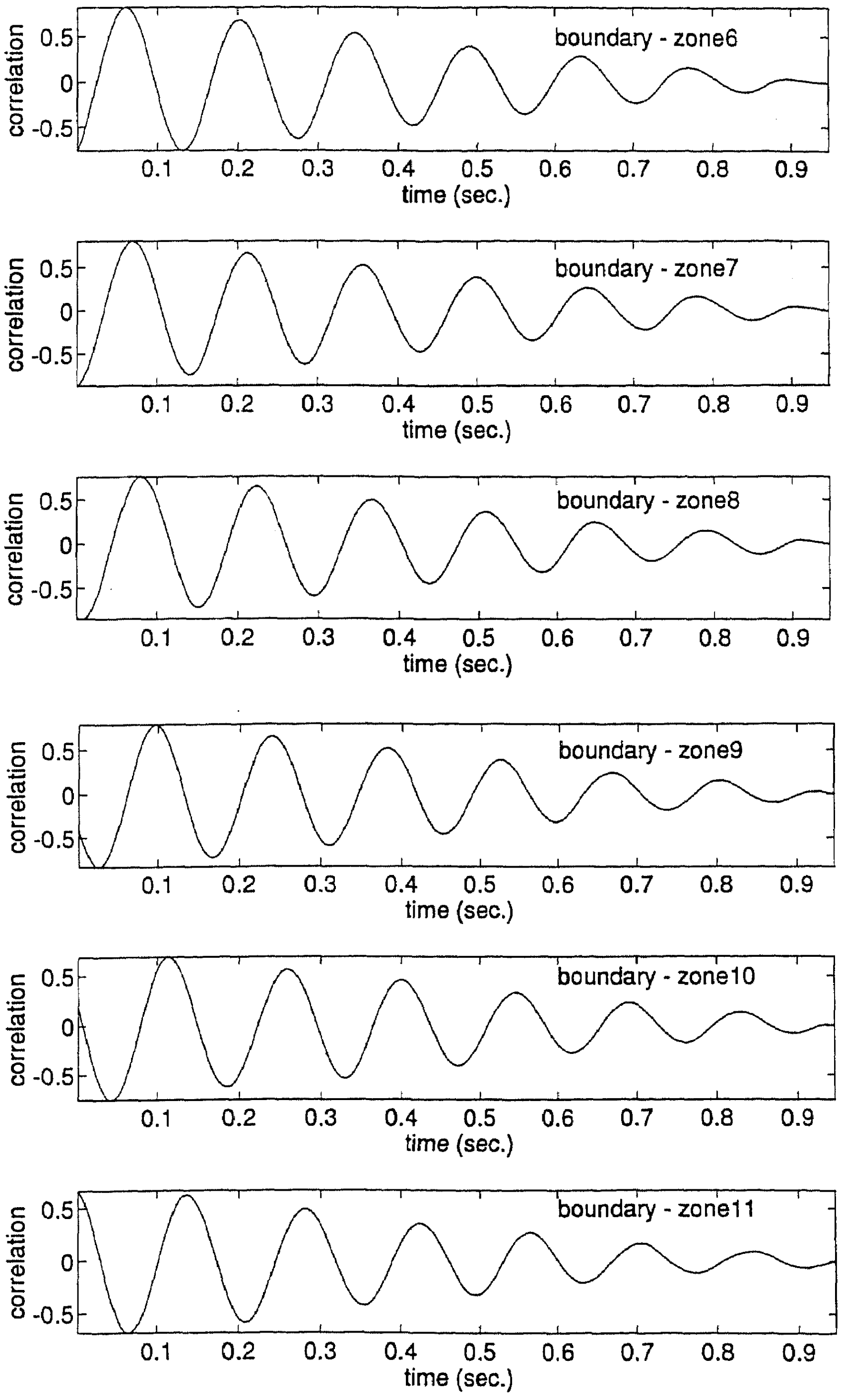

Figure A4.14 Cross correlations between the boundary velocity and the y-components of the mean velocity in zone 6 ~ zone 11 in a system where $m_t = 5$, $d = 0.1\text{m}$, shaking amplitude =.5d, $\Gamma = 10g$, $e = 0.9$, $K_l = 2.8 \times 10^6$, $\rho = 1200\ kg/m^3$.

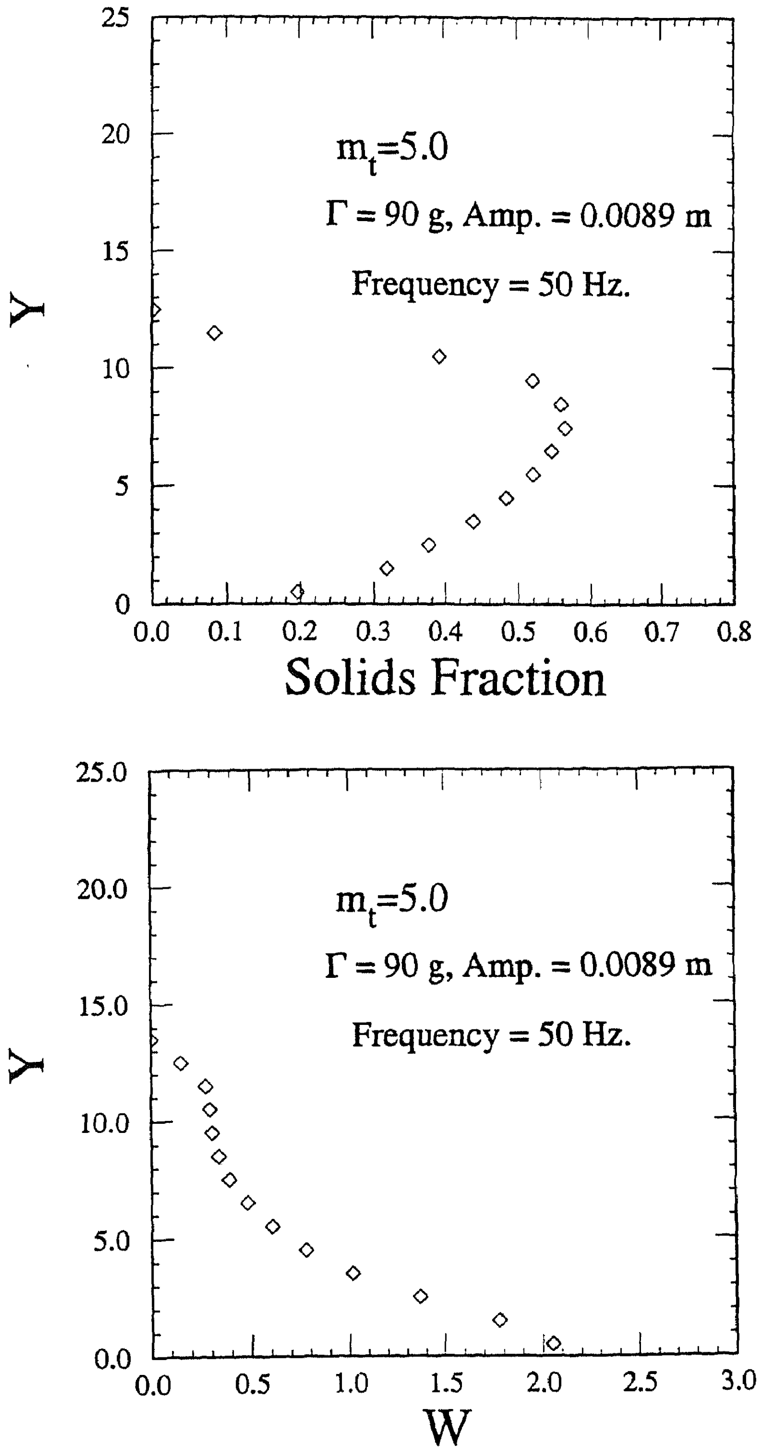

Figure A4.15a Dimensionless granular temperature and solids fraction depth profiles at $\Gamma = 90g$ and amplitude $a \cong 0.1d$ for a system where $m_t = 5$, $d = 0.1$m, $e = 0.9$, $K_1 = 2.7 \times 10^8$, $\rho = 1200\ kg/m^3$.

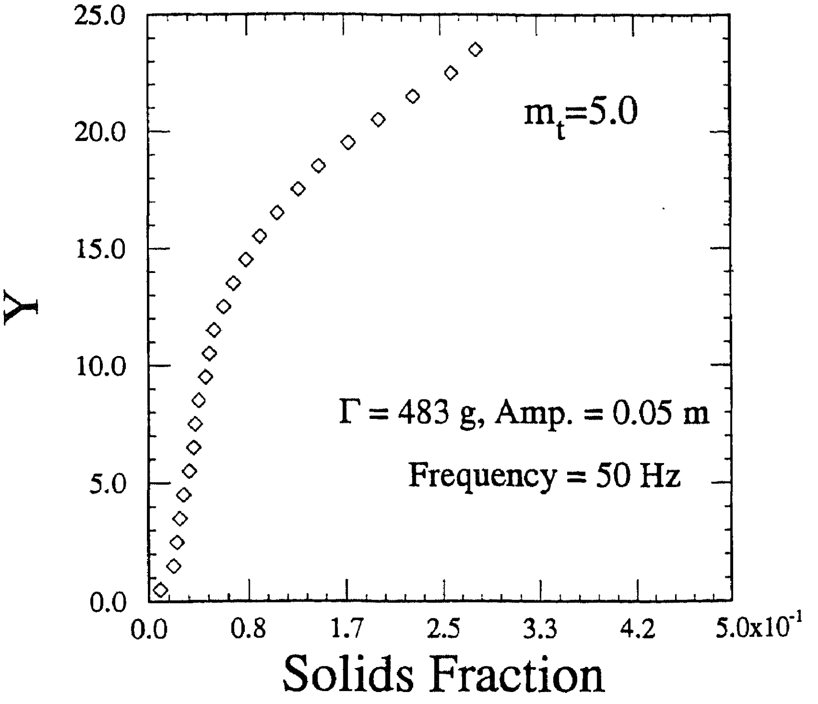

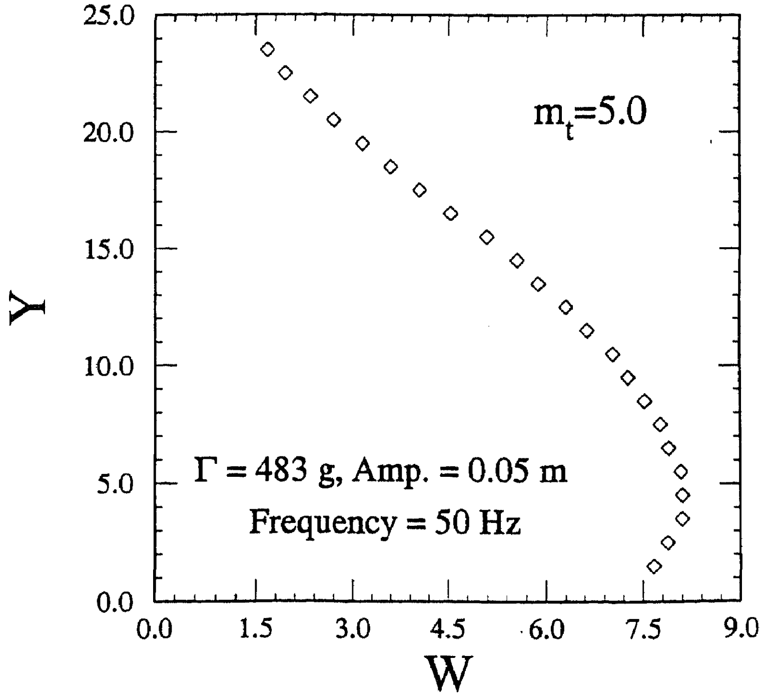

Figure A4.15b Dimensionless granular temperature and solids fraction depth profiles at $\Gamma = 483g$ and amplitude $a = d/2$, for a system where. $m_t = 5$, $d = 0.1$m, $e = 0.9$, $K_1 = 2.8 \times 10^6$, $\rho = 1200\ kg/m^3$.

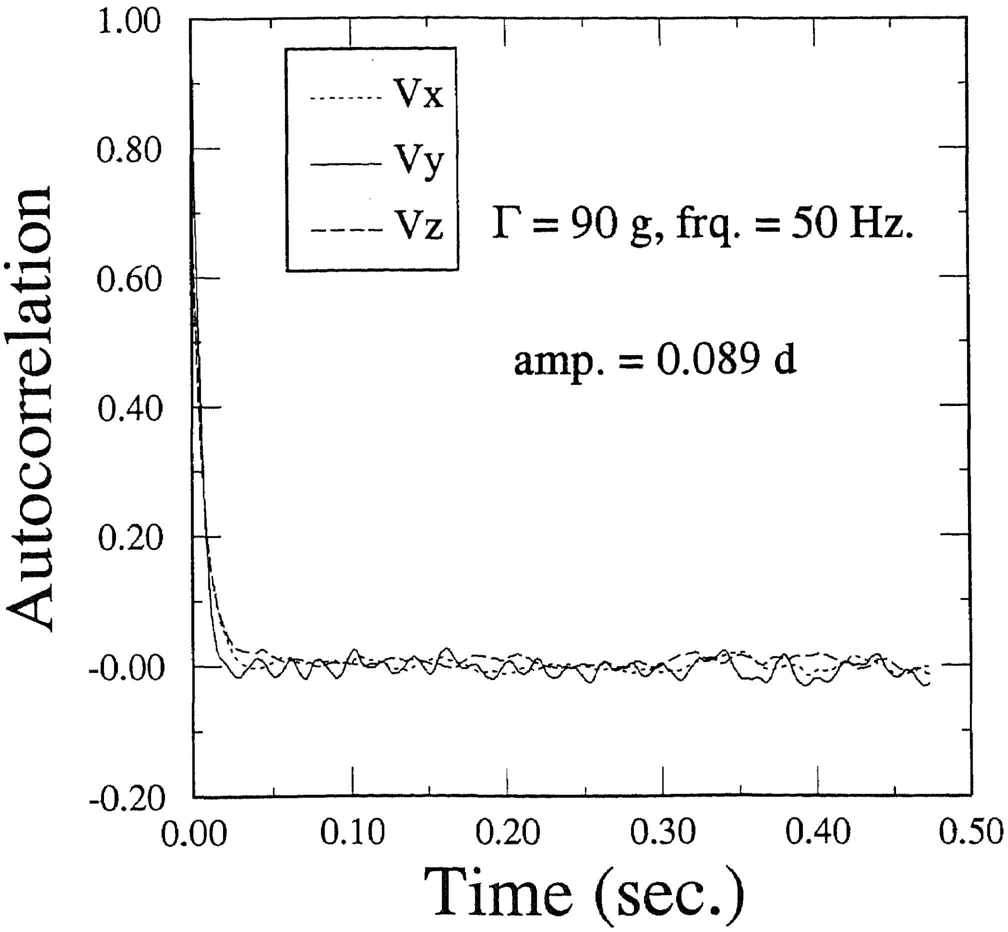

Figure A4.16 Components of the velocity autocorrelation function for $\Gamma = 90g, f = 50$ Hz and amplitude $a \cong 0.1d$.($m_t = 5$, $d = 0.1$m, $e= 0.9$, $K_1 = 2.7 \times 10^8$, $\rho= 1200\ kg/m^3$)

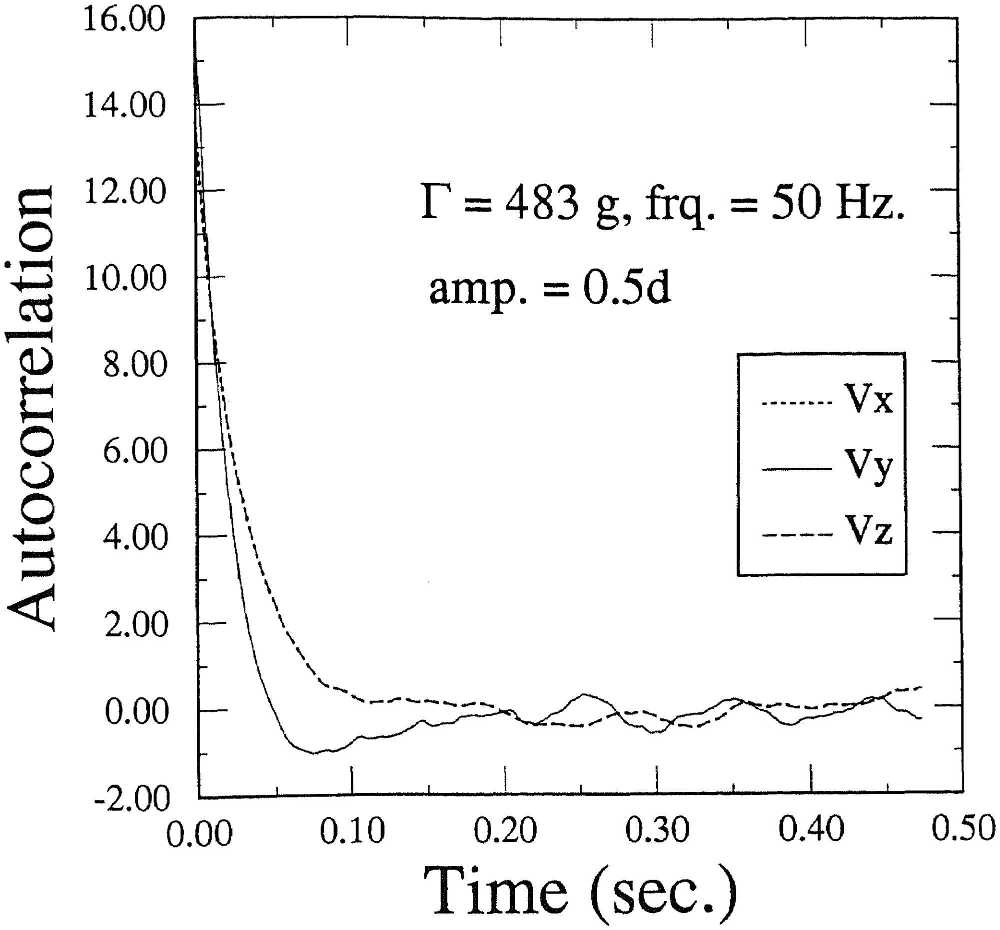

Figure A4.17 Components of the velocity autocorrelation function for Γ = $483g, f$ = 50 Hz and amplitude $a = d/2$.(m_t = 5, d = 0.1m, e= 0.9, K_l = 2.8×10^6, ρ = 1200 kg/m^3)

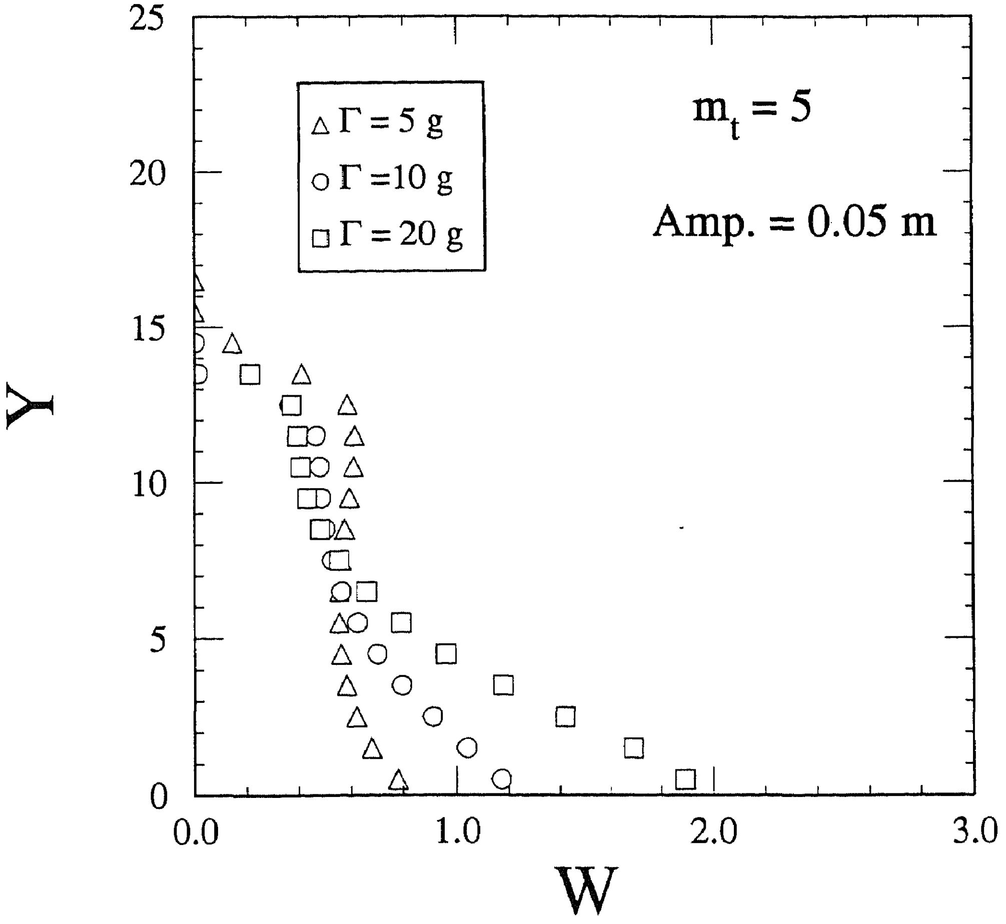

Figure A4.18 Dimensionless granular temperature profiles for a fixed shaking amplitude $a = d/2$ and $\Gamma = 5g$, $10g$ and $20g$. ($m_t = 5$, $d = 0.1$m, $e = 0.9$, $K_1 = 2.7 \times 10^8$, $\rho = 1200\ kg/m^3$)

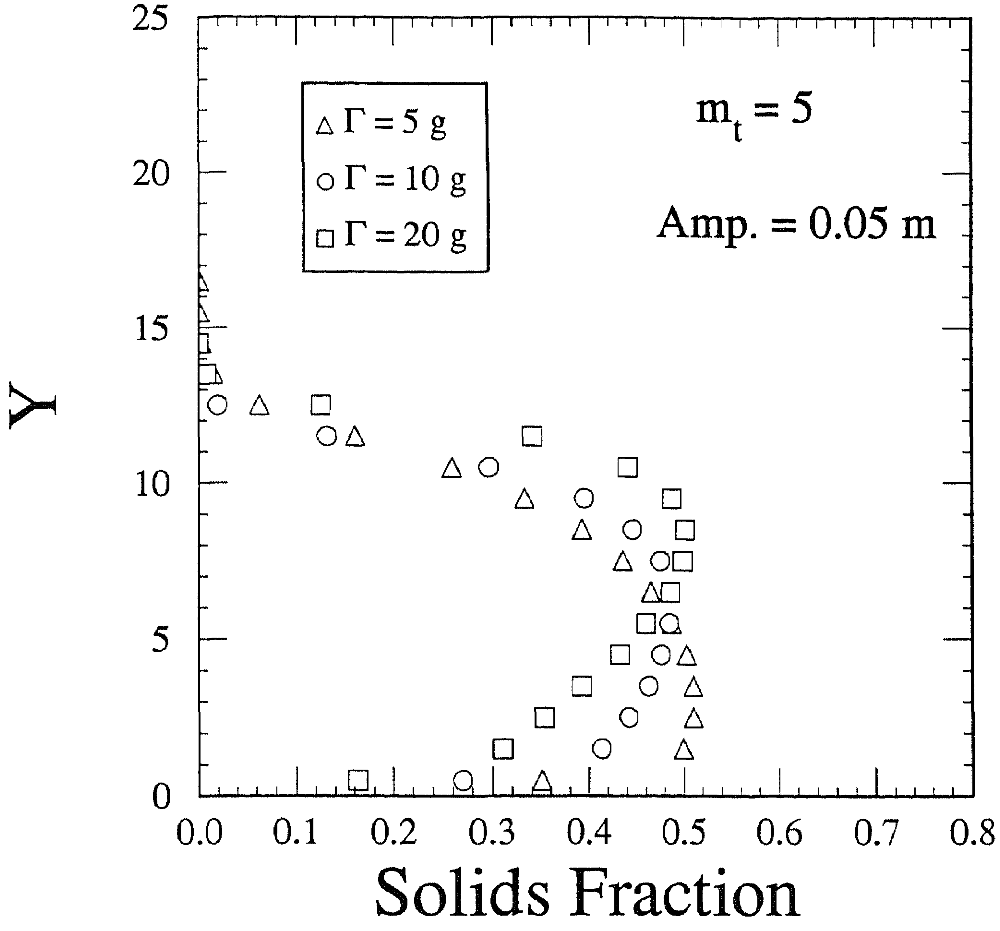

Figure A4.19 Solids fraction depth profiles for a fixed shaking amplitude $a = d/2$ and $\Gamma = 5g$, $10g$ and $20g$.($m_t = 5$, $d = 0.1$m, $e = 0.9$, $K_1 = 2.7 \times 10^8$, $\rho = 1200\ kg/m^3$)

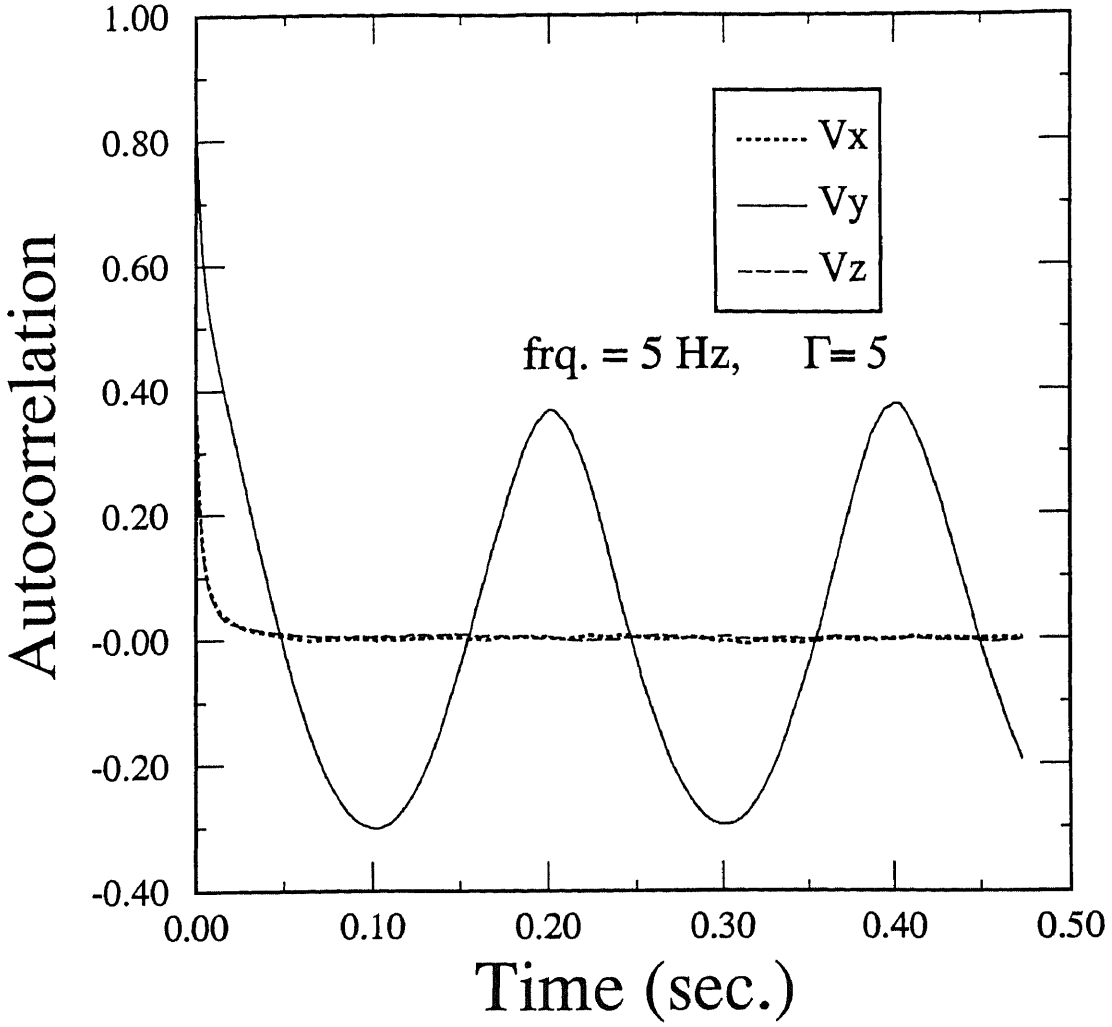

Figure A4.20 Velocity autocorelation function for $a = d/2$ and $\Gamma = 5g$ whose dimensionless granular temperature and solids fraction depth profiles are shown in Figure A4.18 and A4.19.

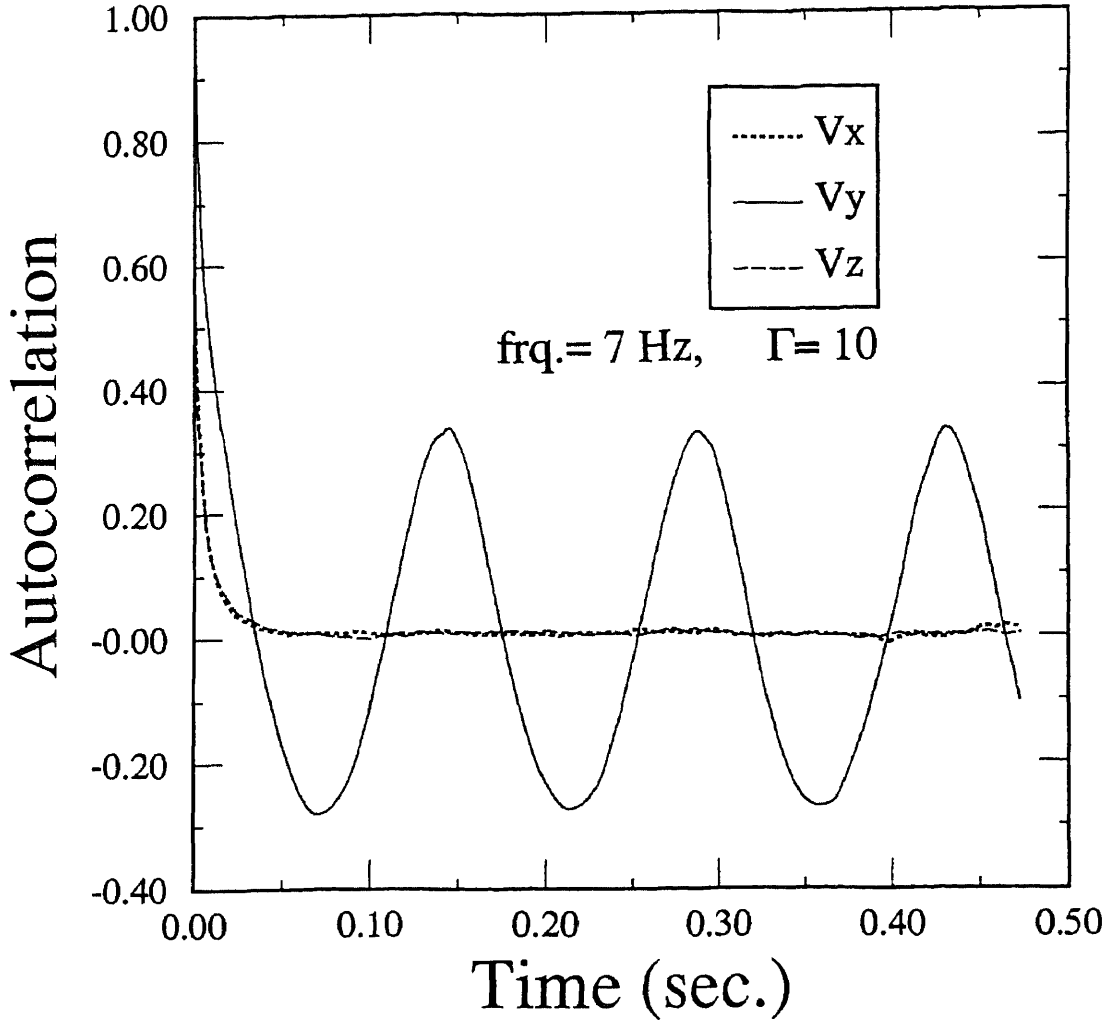

Figure A4.21 Velocity autocorelation function for $a = d/2$ and $\Gamma = 10g$ whose dimensionless granular temperature and solids fraction depth profiles are shown in Figure A4.18 and A4.19.

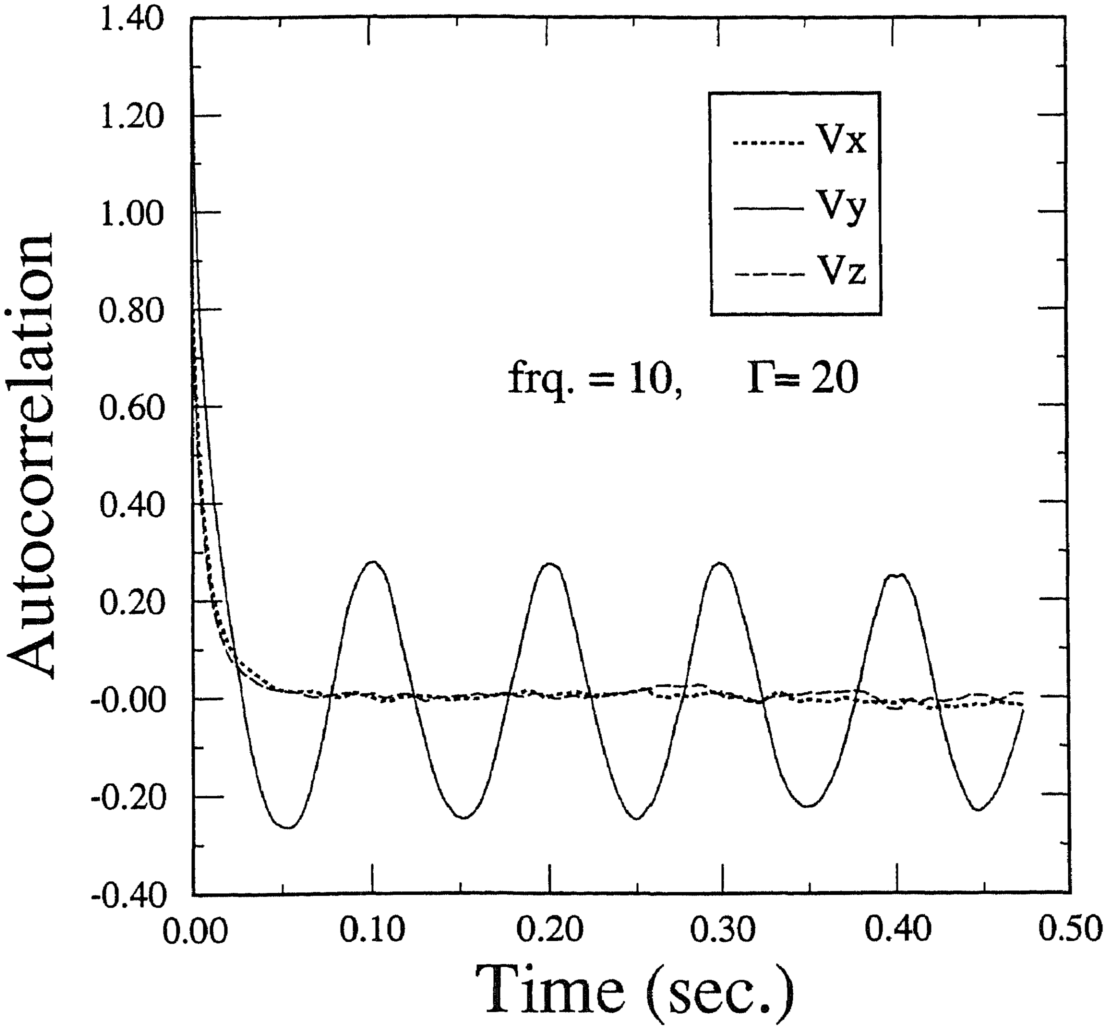

Figure A4.22 Velocity autocorelation function for $a = d/2$ and $\Gamma = 20g$ whose dimensionless granular temperature and solids fraction depth profiles are shown in Figure A4.18 and A4.19.

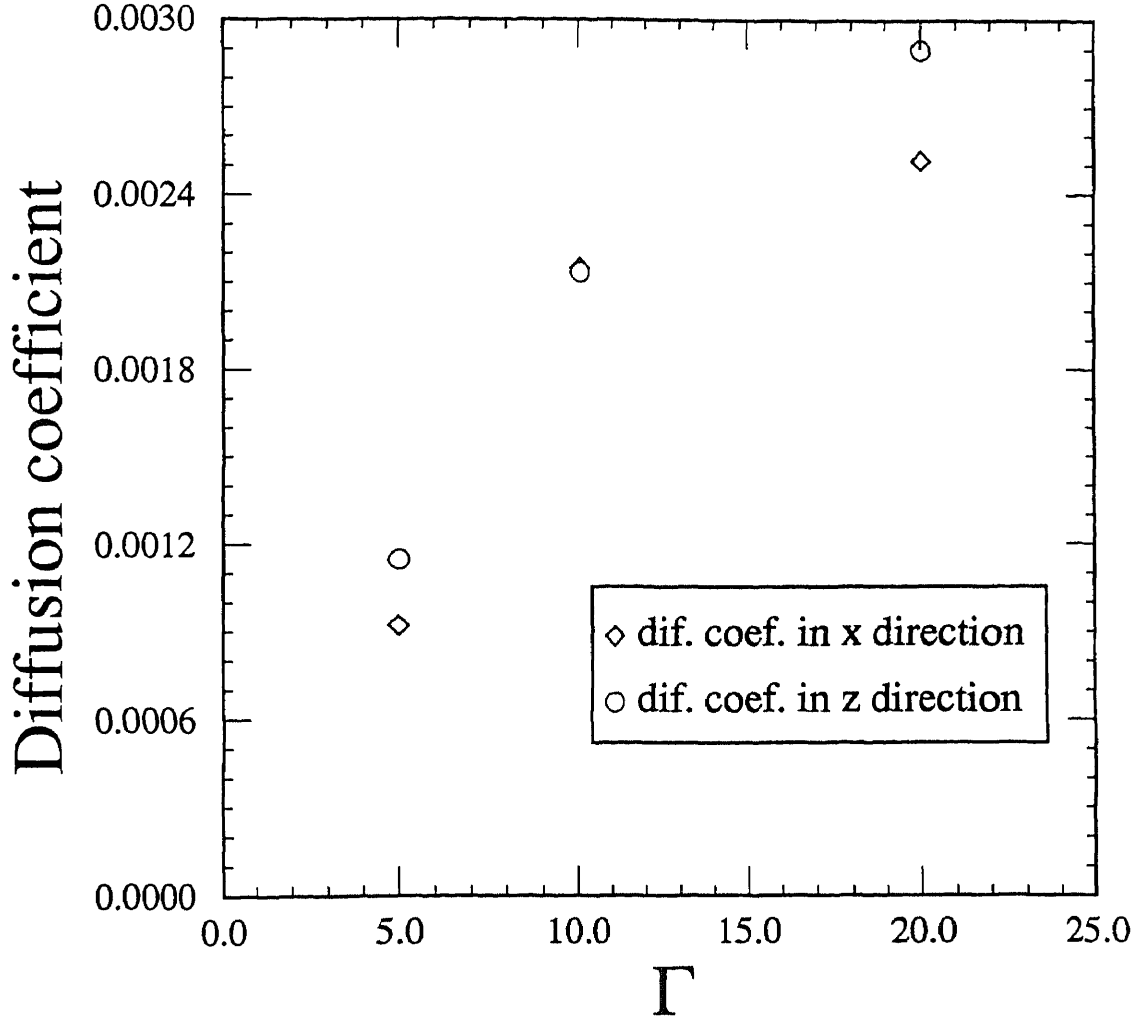

Figure A4.23 Self-diffusion components D_x and D_z versus Γ for the systems whose temperature and solids fraction have been discussed in Figure A4.18 and A4.19.

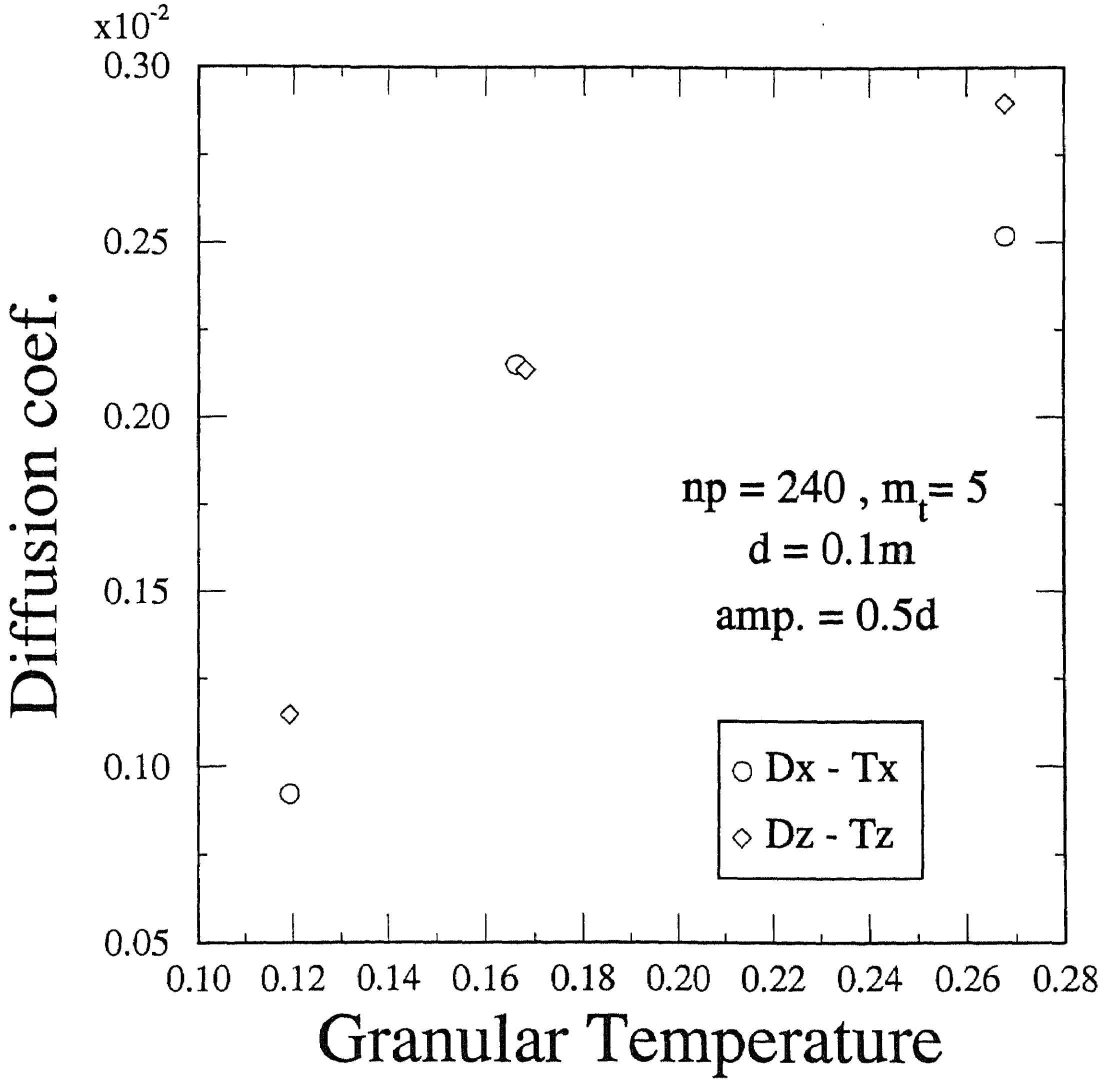

Figure A4.24 Self-diffusion components D_x and D_z versus granular temperature T_x and T_z, respectively.

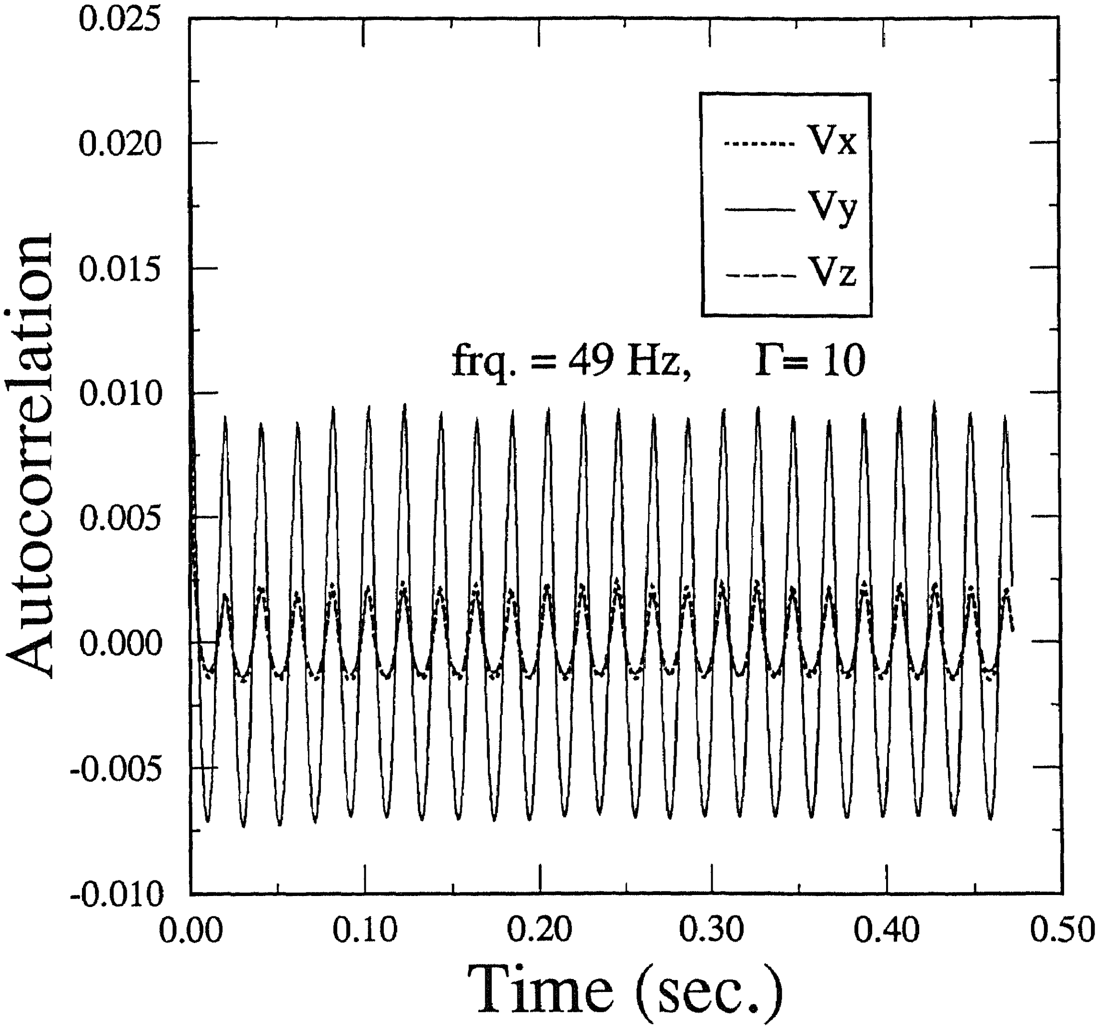

Figure A4.25 Components of the velocity autocorrelation function for f = 50 Hz, Γ = 10g and amplitude a = 0.01d.

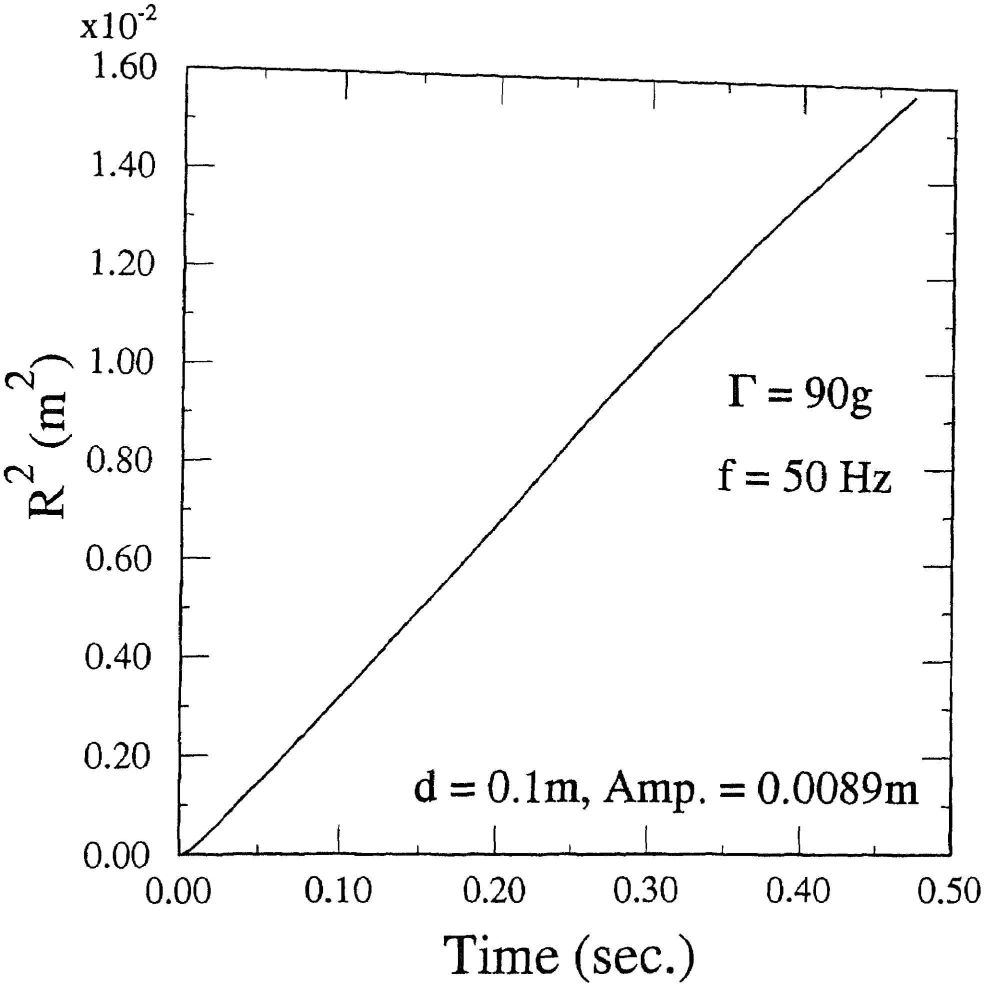

Figure A4.26 The mean square displacement $\left\langle |\mathbf{r}|^2 \right\rangle$.for a case where Γ = 90g, f = 50 Hz d = 0.1m, amp.≅ 0.1d. The liming slope of this curve is used to compute the diffusion coefficient D^*

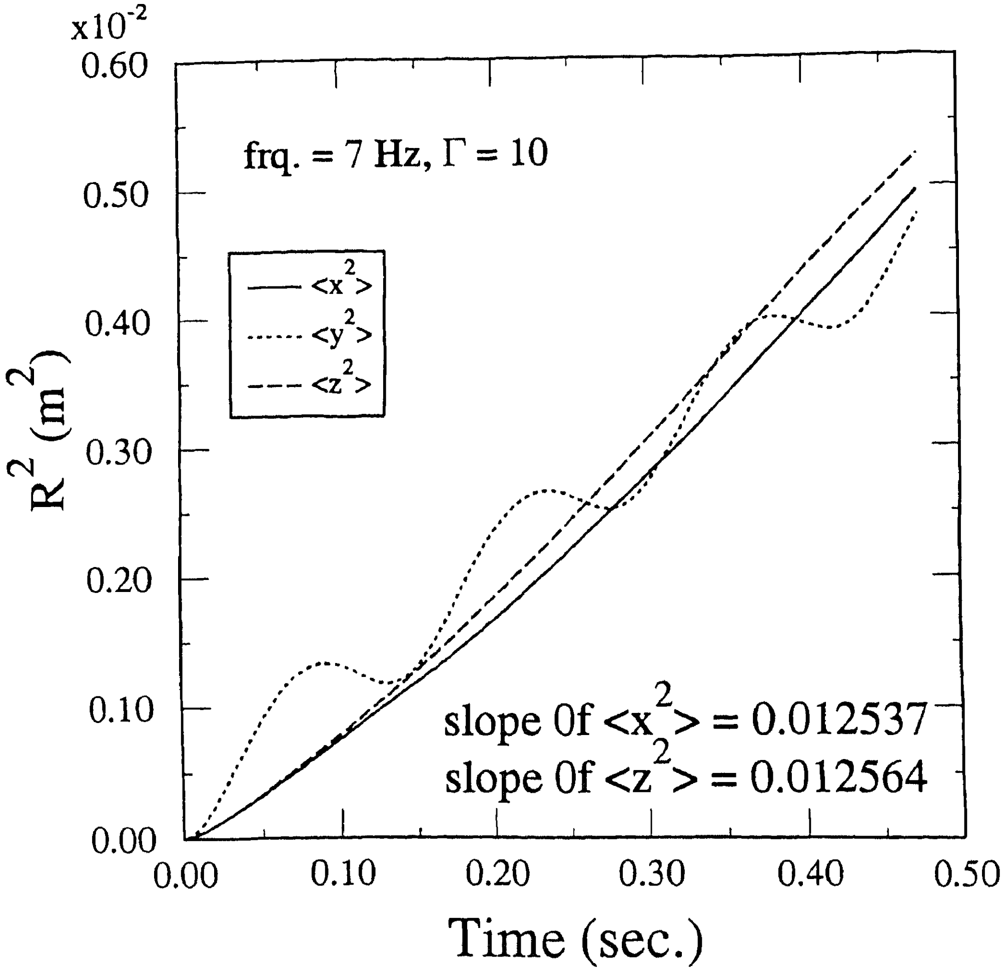

Figure A4.27 The x, y and z components of the mean square displacement. The limiting slopes of these curves are used to compute the D_x^* and D_z^*.

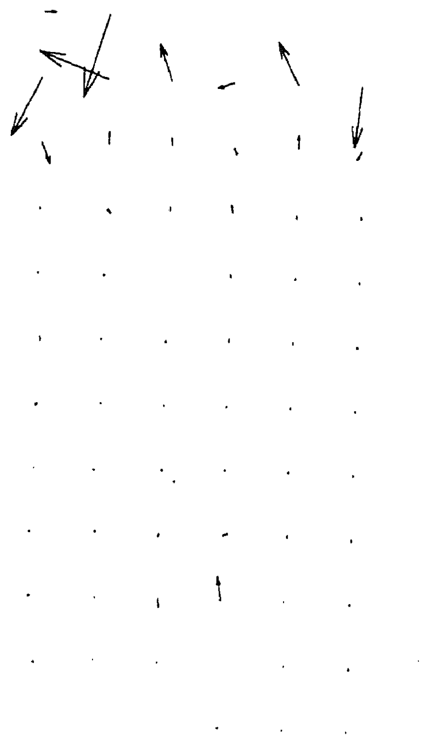

Amplitude = 0.25 d.

Figure A5.1a Mean velocity field for the case where $\Gamma = 10g$, $f = 9.996$ Hz, $d = 0.1$m , amplitude = 0.25*d*., and friction coefficient for both particles and boundaries are 0.8.

Amplitude = 0.3 d.

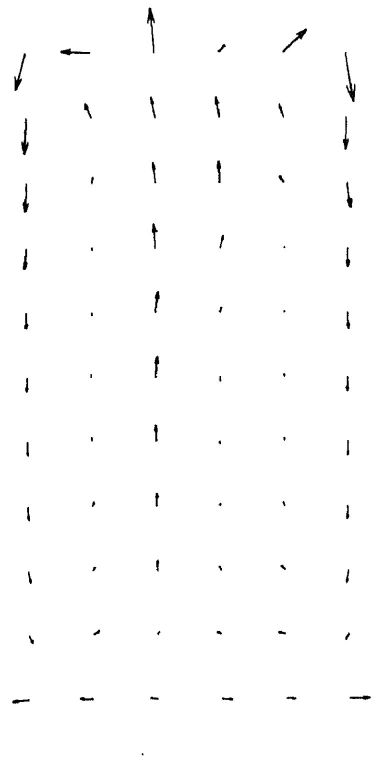

Figure A5.1b Mean velocity field for the case where Γ = 10g, f = 7.878 Hz . d = 0.1m , amplitude = 0.3d., and friction coefficient for both particles and boundaries are 0.8.

Amplitude = 0.5d.

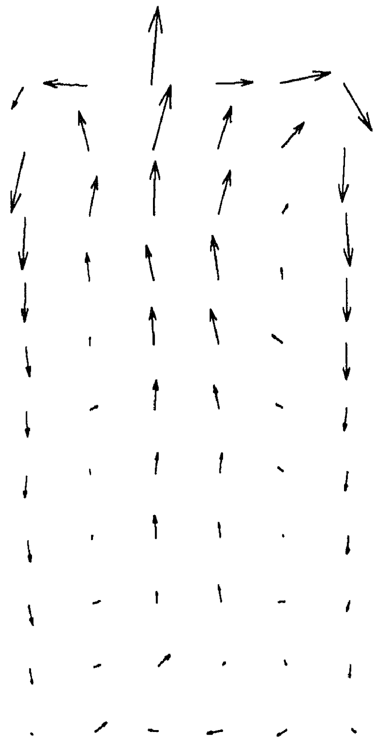

Figure A5.1c Mean velocity field for the case where $\Gamma = 10g$, $f = 7$ Hz, $d = 0.1$m , amplitude = $0.50d$., and friction coefficient for both particles and boundaries are 0.8.

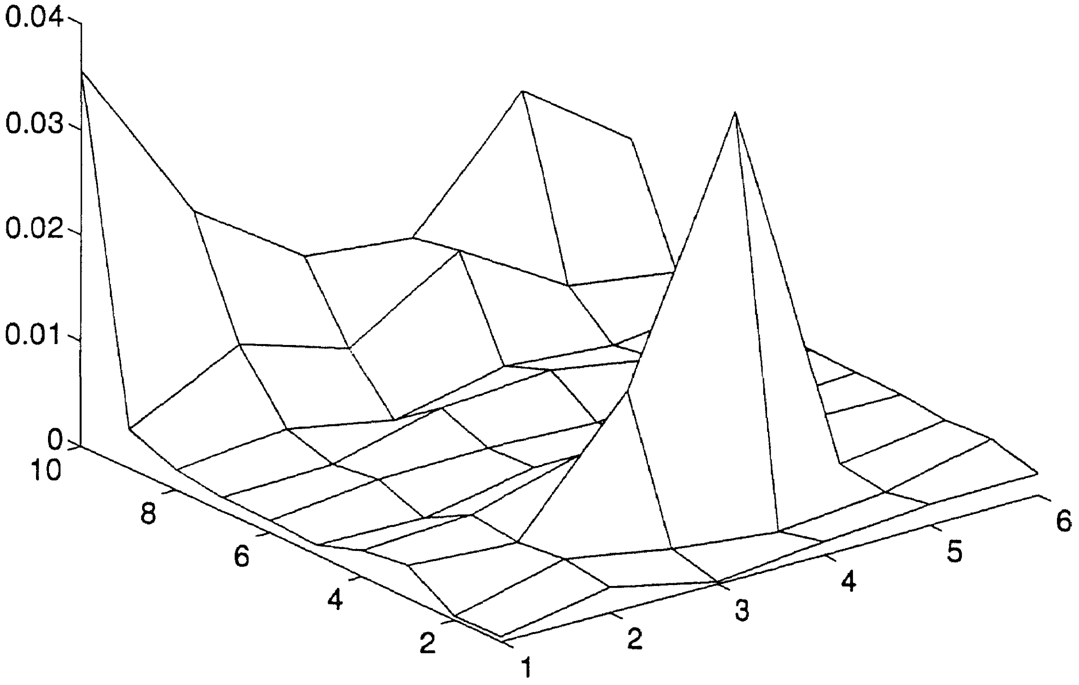

Figure A5.2a Magnitudes of mean velocity vectors for the case shown in Figure A5.1a plotted as coordinates along the vertical axis. The horizontal axes describe coordinates. along the convection plane (.i.e, the *y*-*z* plane) normalized by the particle diameter.

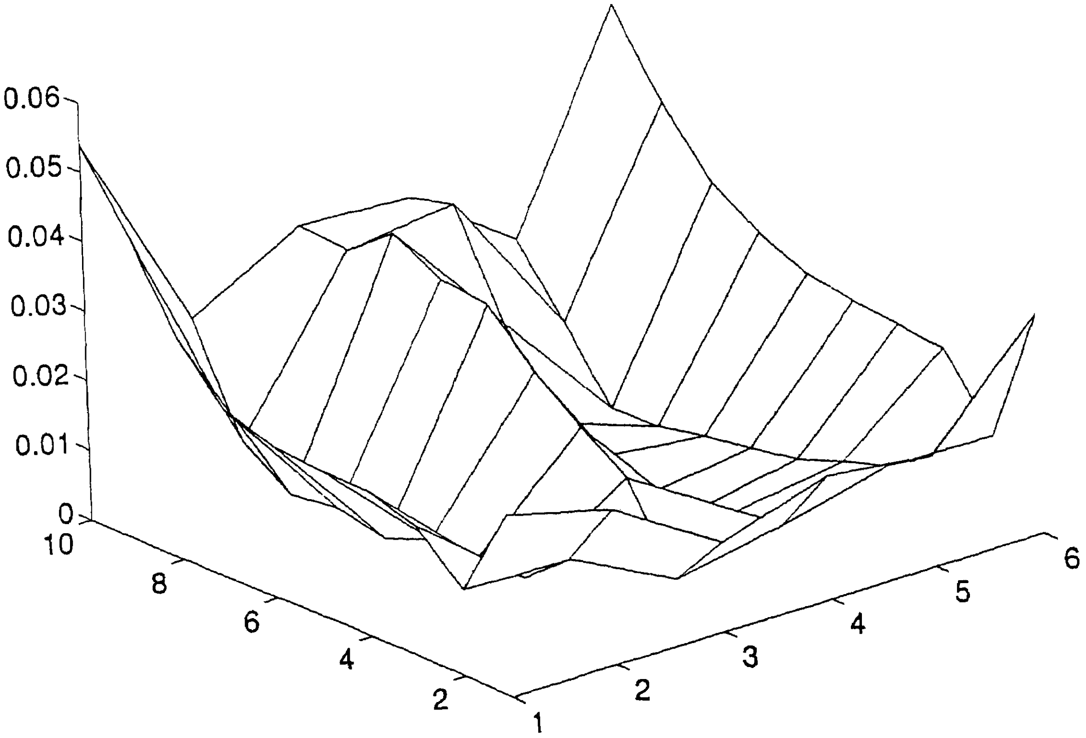

Figure A5.2b Magnitudes of mean velocity vectors for the case shown in Figure A5.1b plotted as coordinates along the vertical axis. The horizontal axes describe coordinates along the convection plane (.i.e, the y-z plane) normalized by the particle diameter.

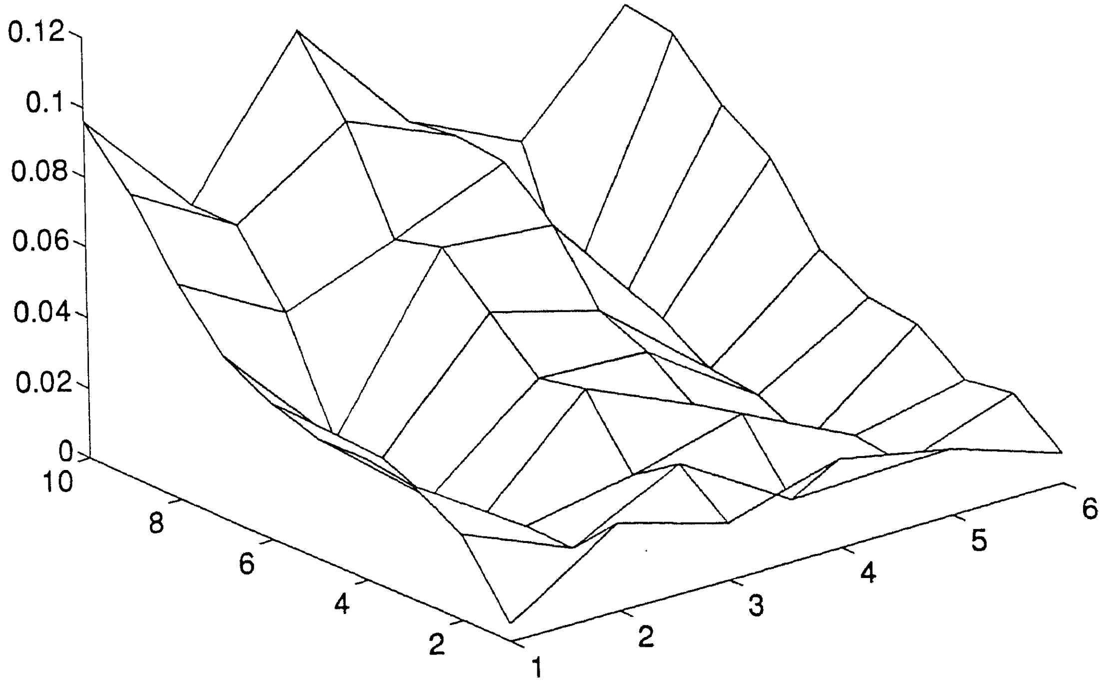

Figure A5.2c Magnitudes of mean velocity vectors for the case shown in Figure A5.1c plotted as coordinates along the vertical axis. The horizontal axes describe coordinates along the convection plane (.i.e, the *y*-*z* plane) normalized by the particle diameter.

fmu = fmub = 0.8

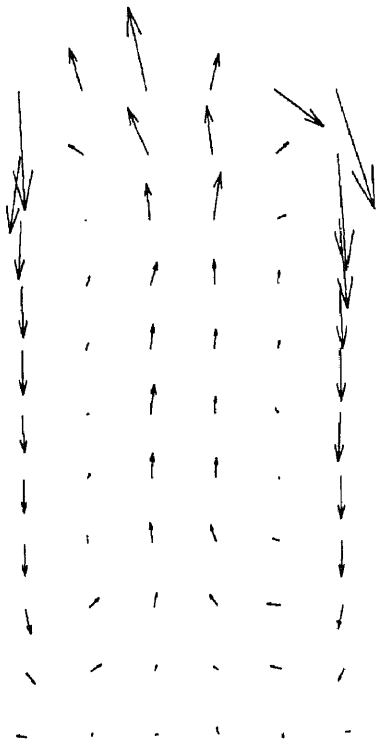

Figure A5.3 Mean velocity vector field in a $6d \times 3d$ cell where the particle and wall friction coefficients are equal, i.e. *fmu* = *fmub* = *0.8*. (Γ= 10g, d = 0.1m, amplitude = 0.5d and f = 7 Hz.)

fmu = 0.8 fmub = 0.2,

Figure A5.4 Mean velocity vector field in a $6d \times 3d$ cell where *fmu = 0.8*, *fmub = 0.2*.(Γ= 10g, d = 0.1m, amplitude = 0.5d and f = 7 Hz.)

Figure A5.5 Mean velocity vector field in a $6d \times 3d$ cell where *fmu = 0.8, fmub =0.*(Γ= 10g, d = 0.1m, amplitude = 0.5d and f = 7 Hz.)

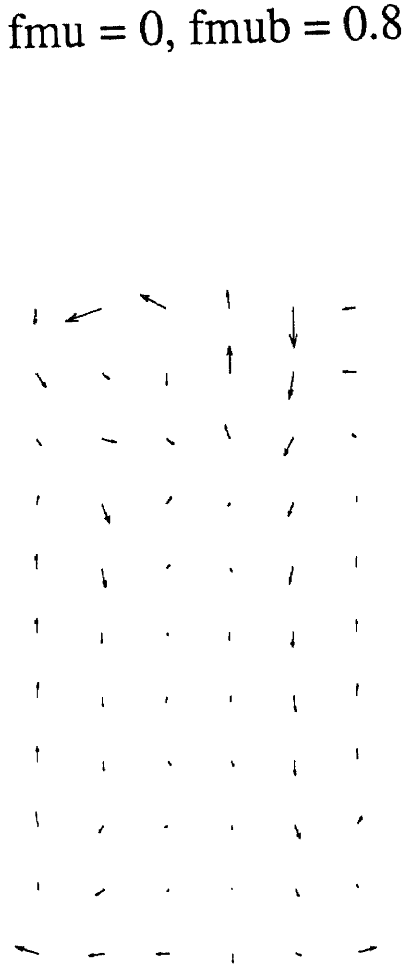

Figure A5.6 Mean velocity vector field in a 6*d* ×3*d* cell where *fmu = 0.0, fmub =0.8*. (Γ= 10g, *d* = 0.1m, amplitude = 0.5*d* and *f* = 7 Hz.)

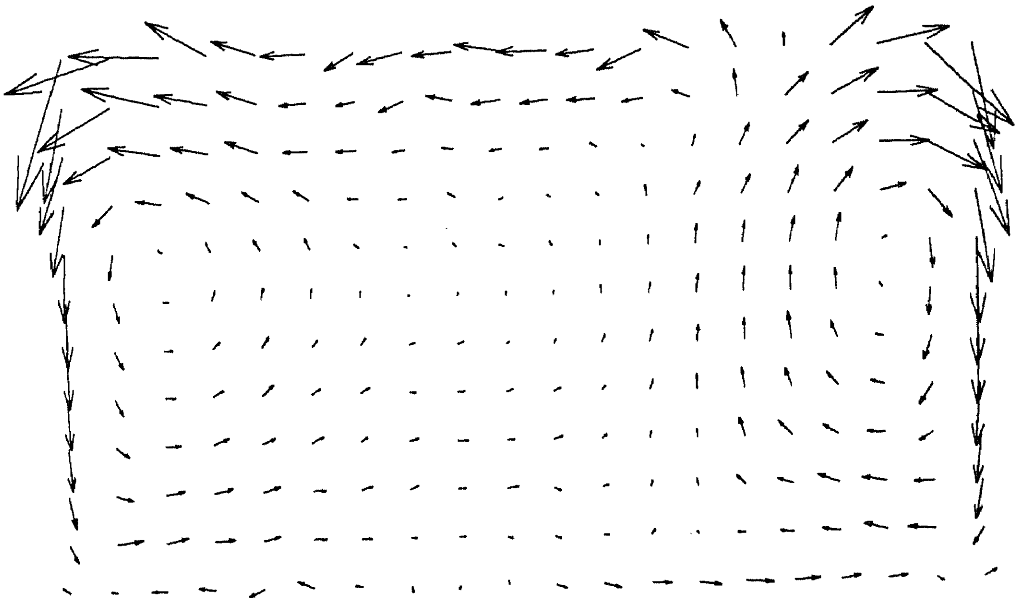

Figure A5.7 Mean velocity vector field for a primary computational cell of length × width = 20*d*×3*d*. where *fmu = 0.8, fmub =0.8*.(Γ= 10g, *d* = 0.1m, amplitude = 0.5*d* and *f* = 7 Hz.)

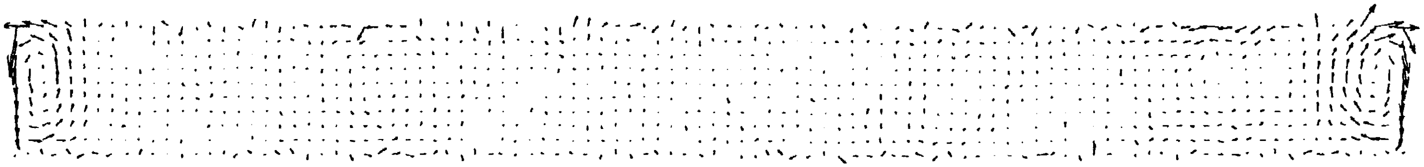

Figure A5.8a Mean velocity vector field for a primary computational cell of length × width = 100*d*×1*d*, where *fmu* = *0.8*, *fmub* =*0.8*.(Γ= 10g, *d* = 0.1m, amplitude = 0.5*d* and *f* = 7 Hz.)

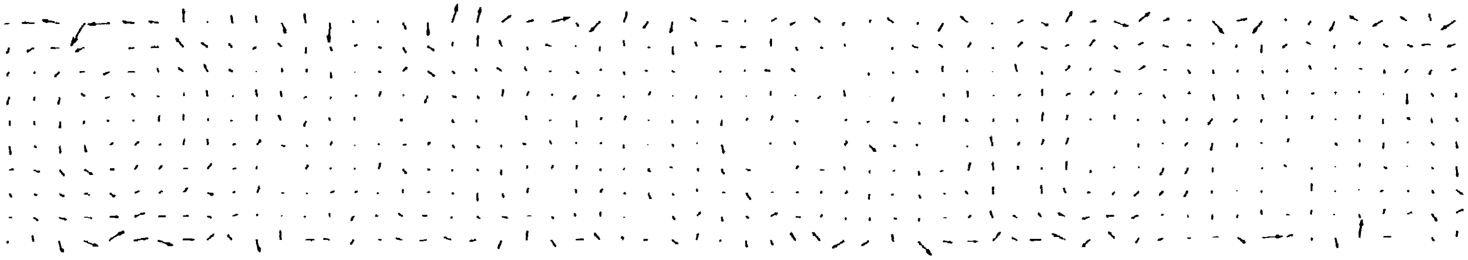

Figure A5.8b Enlarged mean velocity vector field for a central region of the primary computational cell of length × width = 100d×1d.

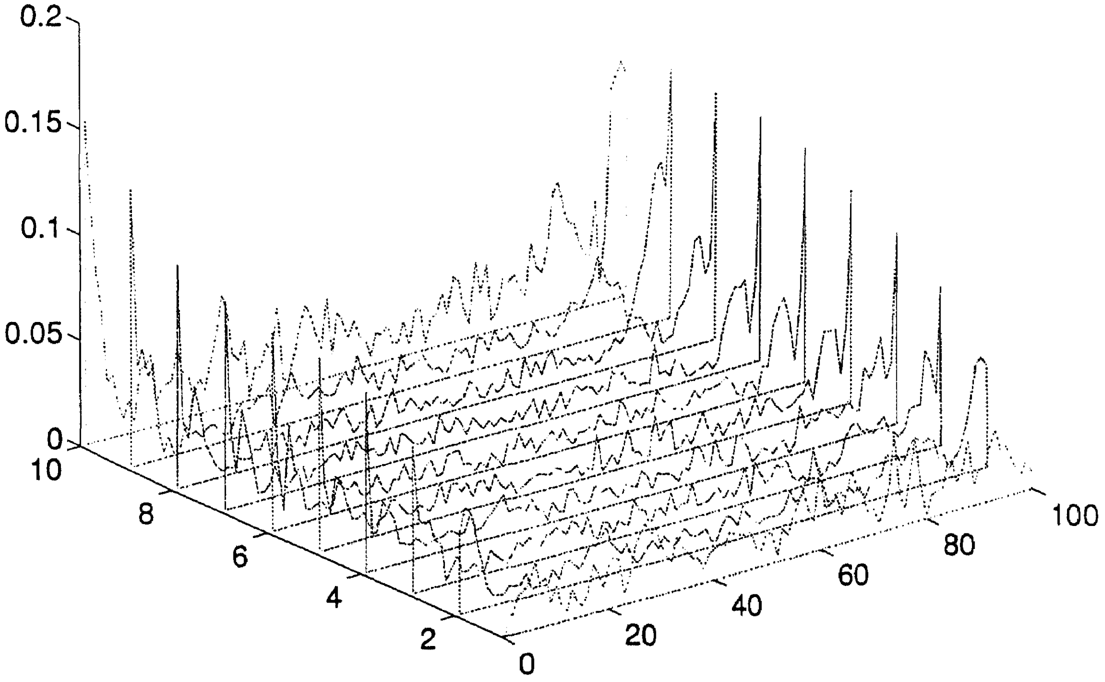

Figure A5.9 Magnitudes of mean velocity vectors for the case shown in Figure A5.8a plotted as coordinates along the vertical axis. The horizontal axes describe coordinates along the convection plane (.i.e, the y-z plane) normalized by the particle diameter.

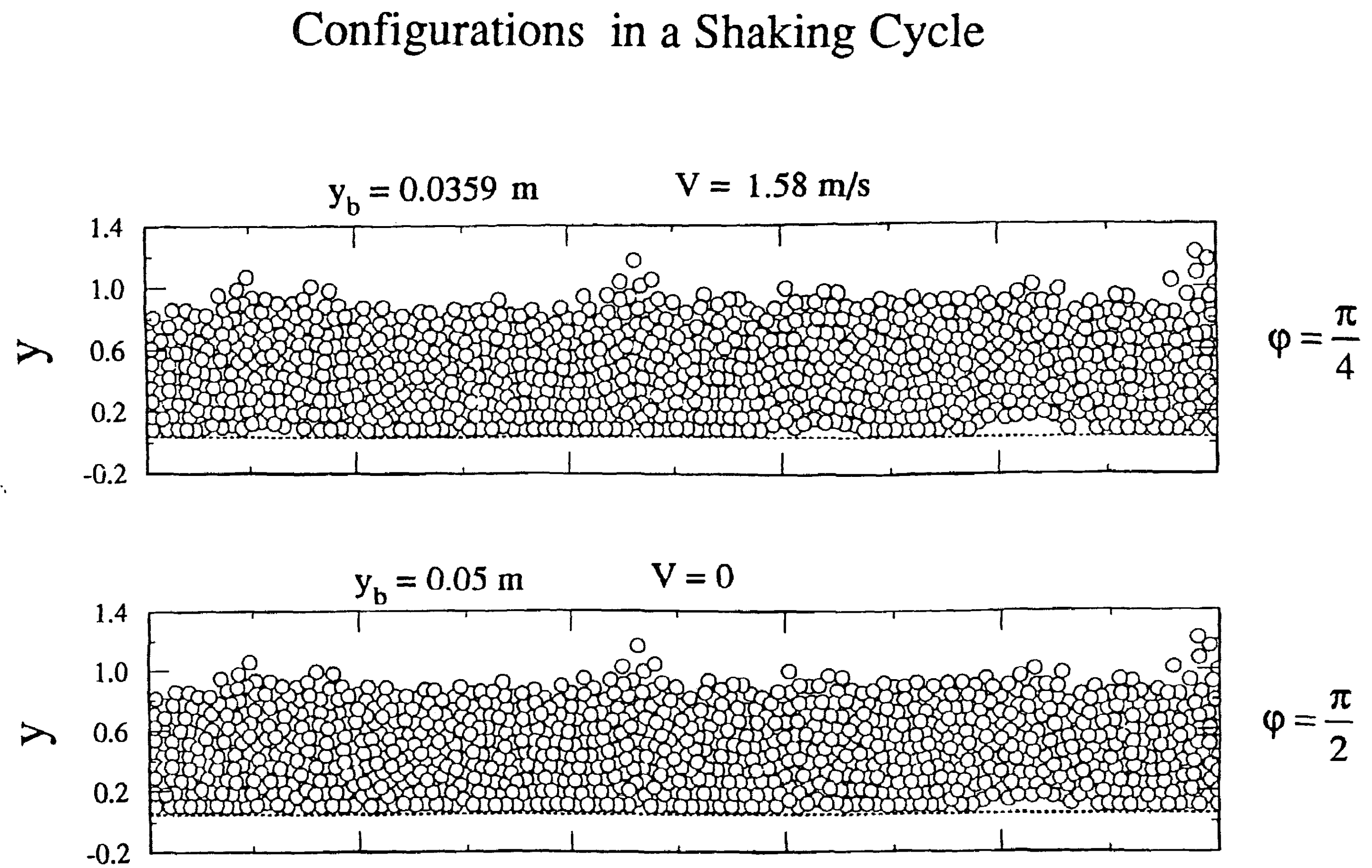

Figure A5.10a *Y-Z* sphere projection plots, for phases $\pi/4$ ($y_b = 0.0359$m, $v = 1.58$ m/s) and $\pi/2$ ($y_b = 0.05$m, $v = 0$). (Primary computational cell dimensions length × width = $100d \times 1d$)

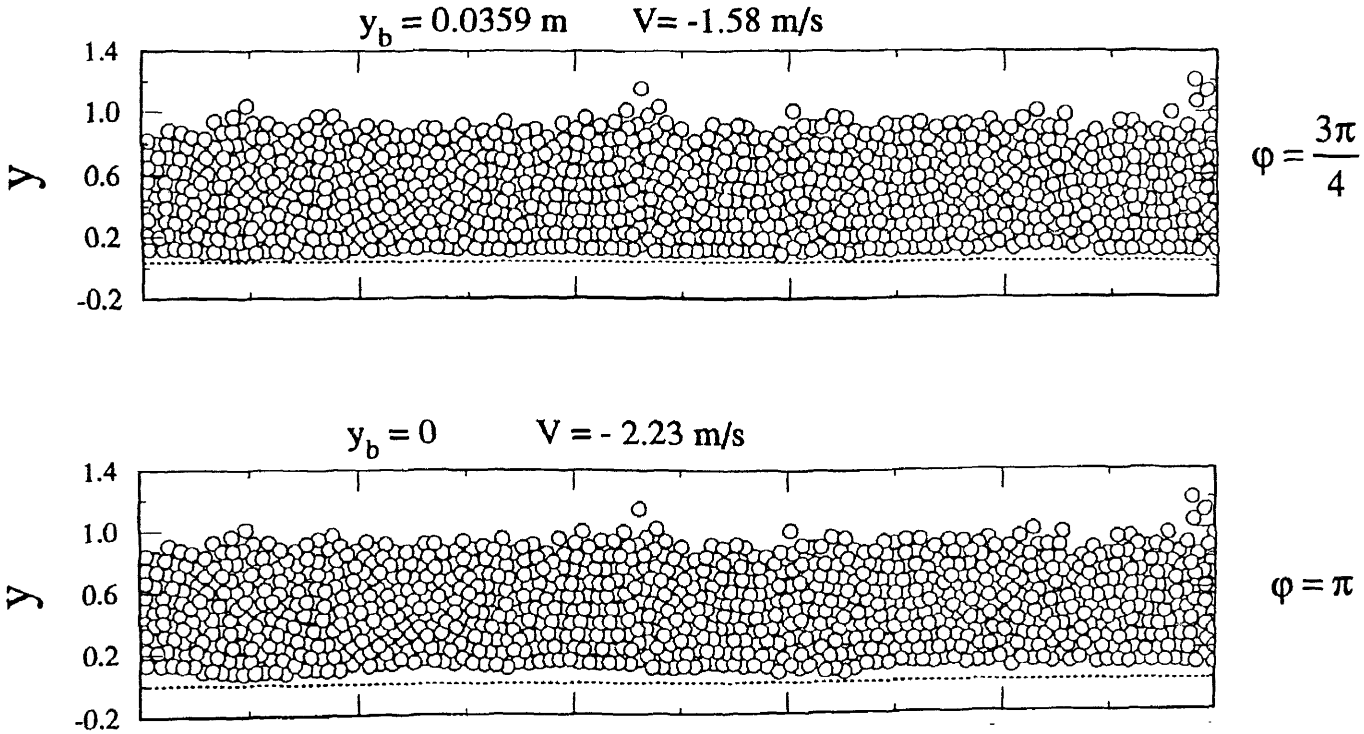

Figure A5.10b *Y-Z* sphere projection plots for phases $3\pi/4$ ($y_b = 0.0359$m, $v = -1.58$ m/s) and π ($y_b = 0.$m, $v = -2.23$m/s). (Primary computational cell dimensions length × width = $100d \times 1d$

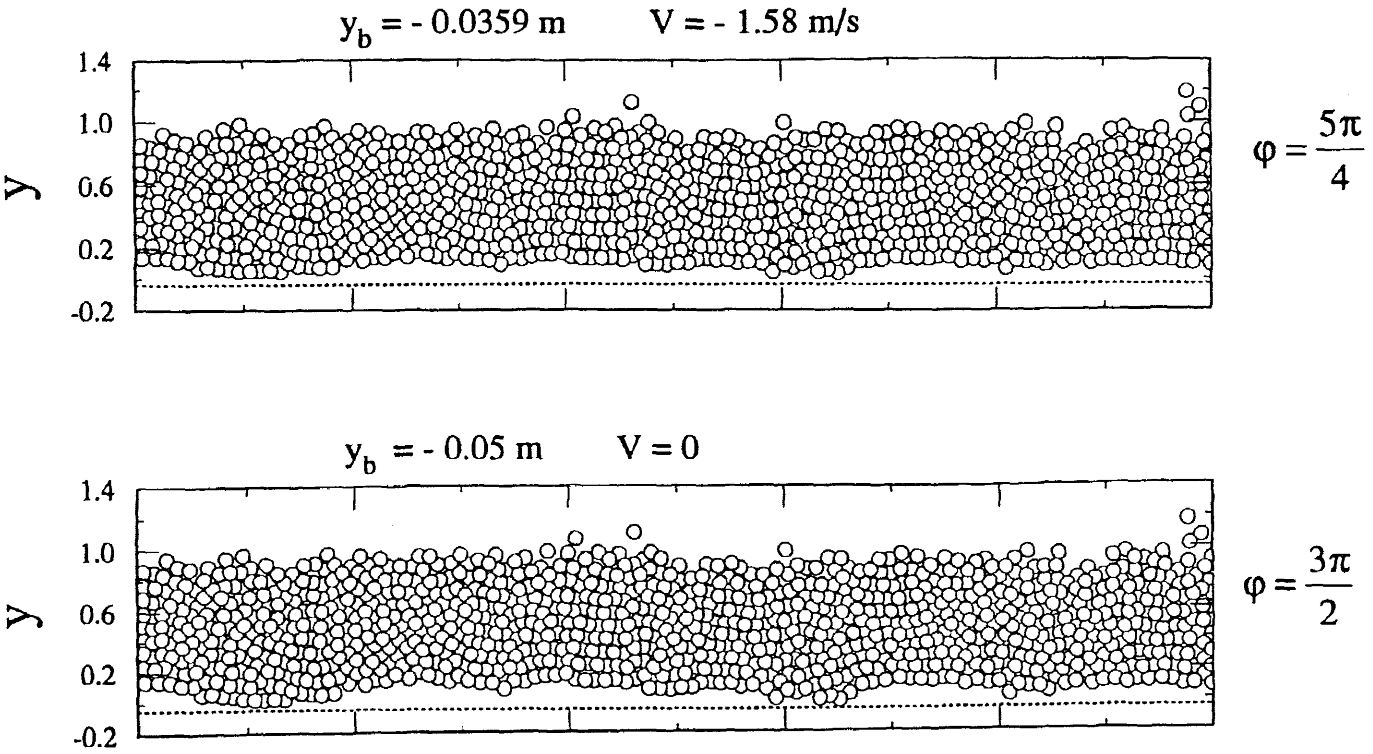

Figure A5.10c *Y*-*Z* sphere projection plots for phase $5\pi/4$ (y_b= -0.0359m, v = - 1.58 m/s) and $3\pi/2$ (y_b = - 0.05m, v = 0). (Primary computational cell dimensions length × width = $100d\times1d$

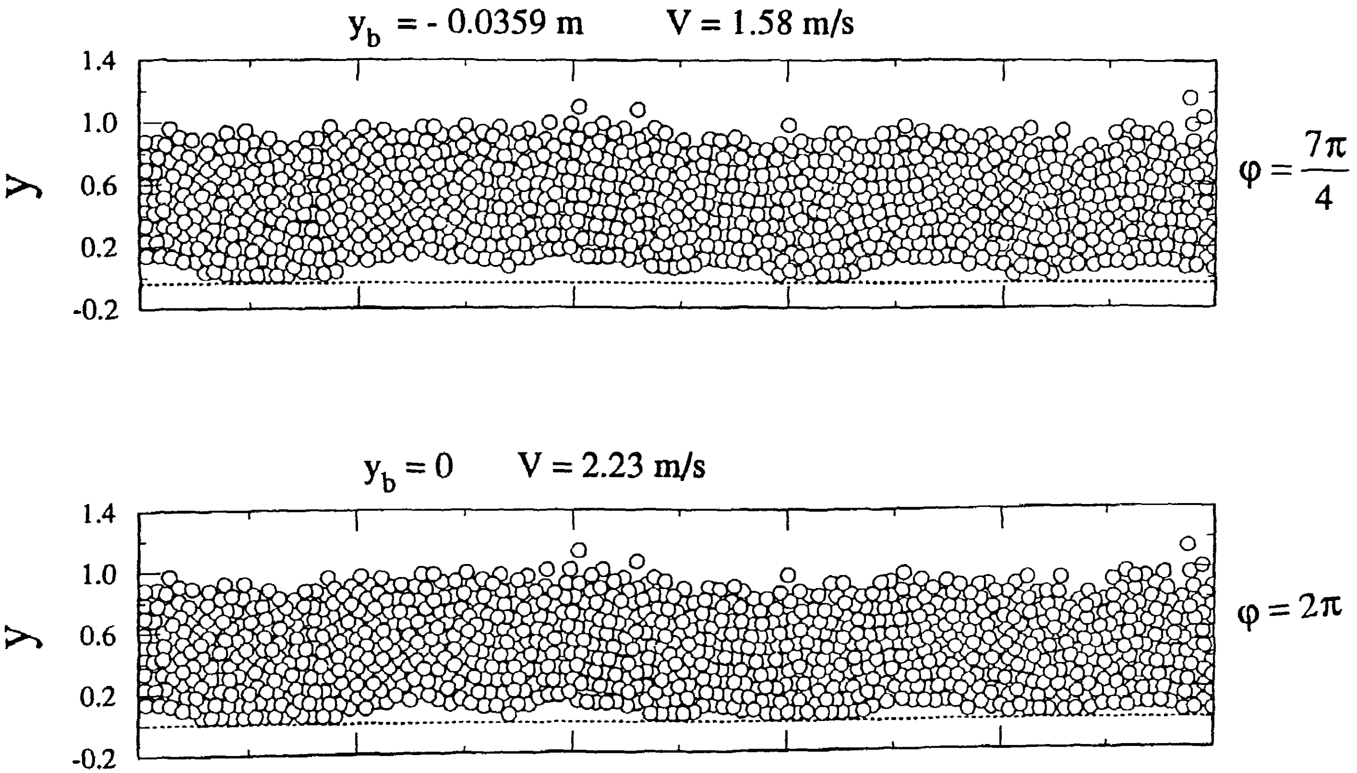

Figure A5.10d *Y-Z* sphere projection plots for the the phases $7\pi/4$ (y_b = -0.0359m, v = 1.58 m/s) and 2π (y_b = 0.0m, v = 2.23m/s). (Primary computational cell dimensions length × width = $100d \times 1d$

Velocity Field in a Shaking Cycle

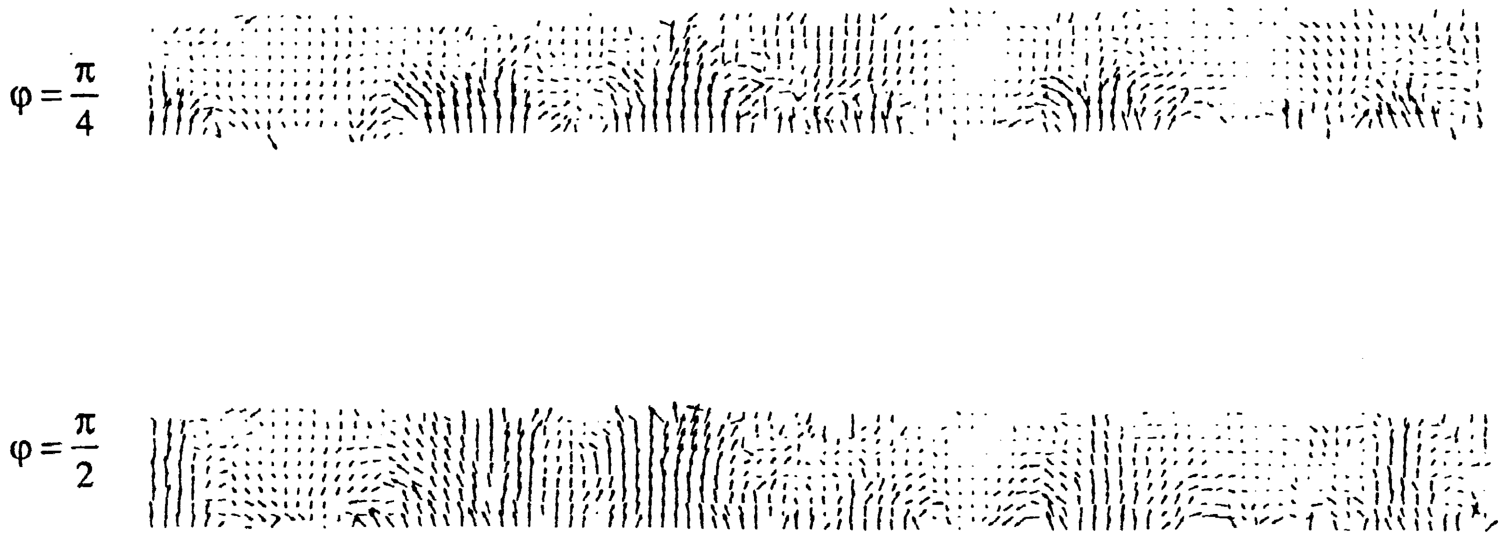

Figure A5.11a Mean velocity fields for phases $\pi/4$ ($y_b = 0.0359$m, v= 1.58 m/s) and $\pi/2$ ($y_b = 0.05$ m, v= 0). (Primary computational cell dimensions length×width = $100d \times 1d$)

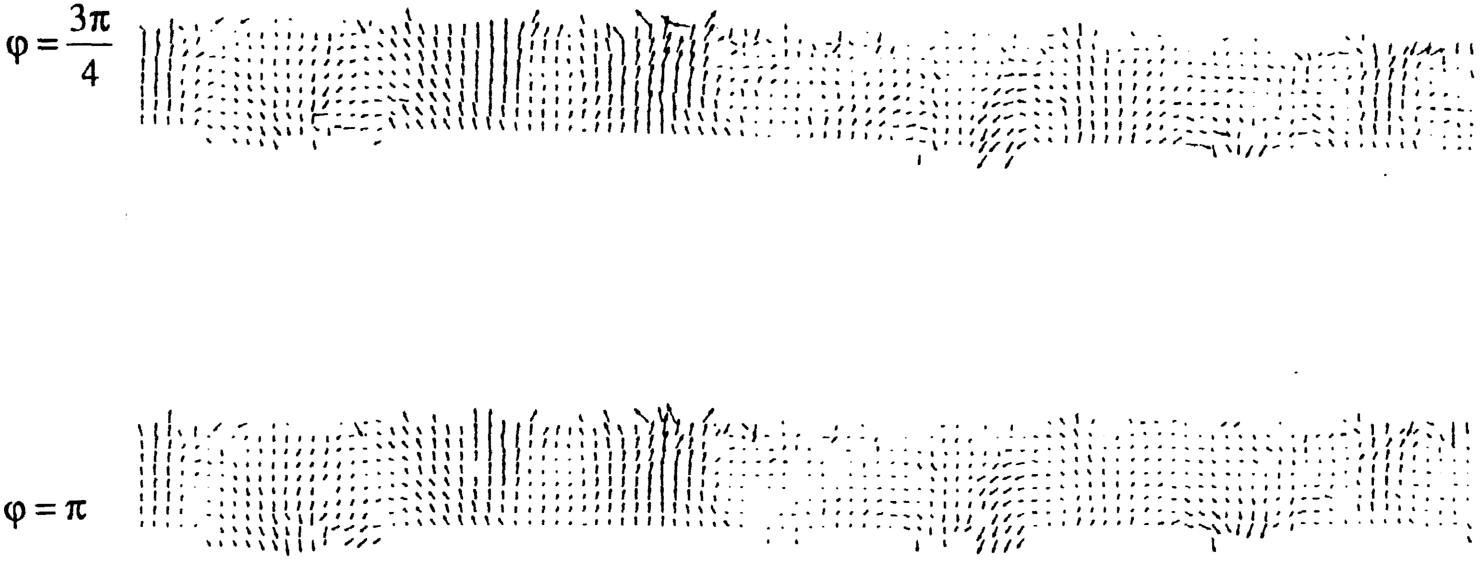

Figure A5.11b Mean velocity vector fields for phases $3\pi/4$ ($y_b = 0.0359$m, v = -1.58 m/s) and π ($y_b = 0.$m, v = -2.23m/s). (Primary computational cell dimensions length × width = $100d\times1d$

Velocity Field in a Shaking Cycle

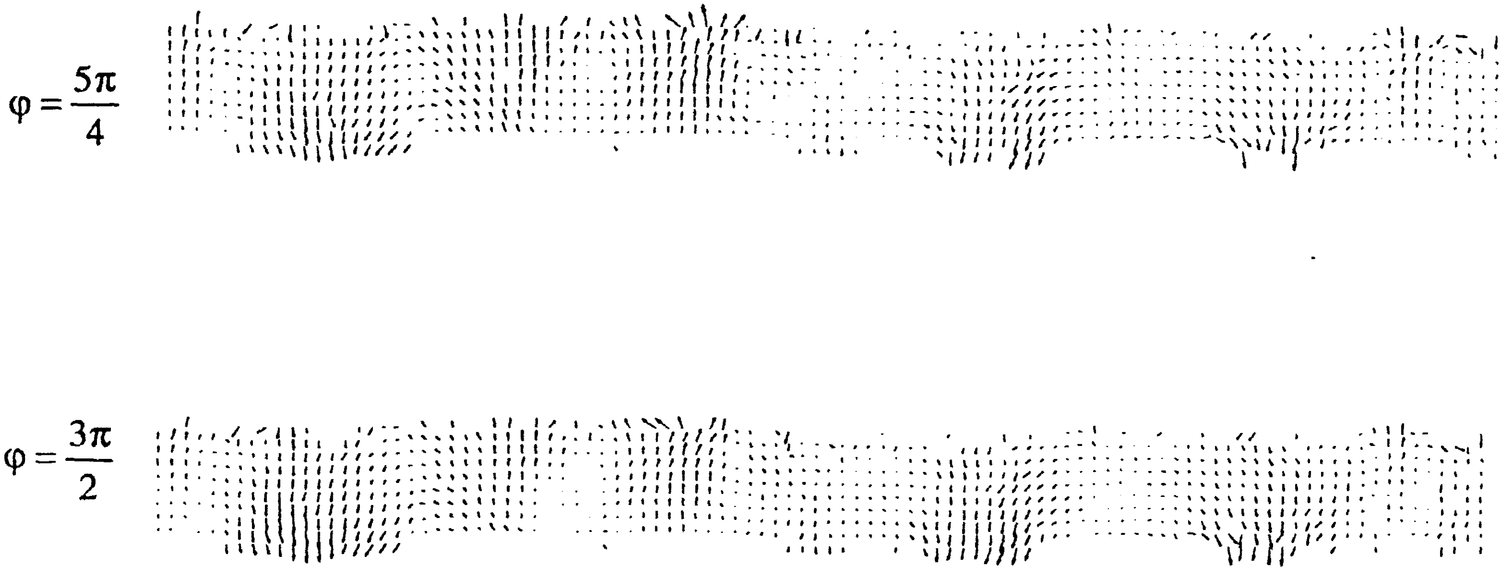

Figure A5.11c Mean velocity vector fields for phases $5\pi/4$ (y_b= -0.0359m, v = - 1.58 m/s) and $3\pi/2$ (y_b = - 0.05m, v = 0). (Primary computational cell dimensions length × width = $100d\times1d$

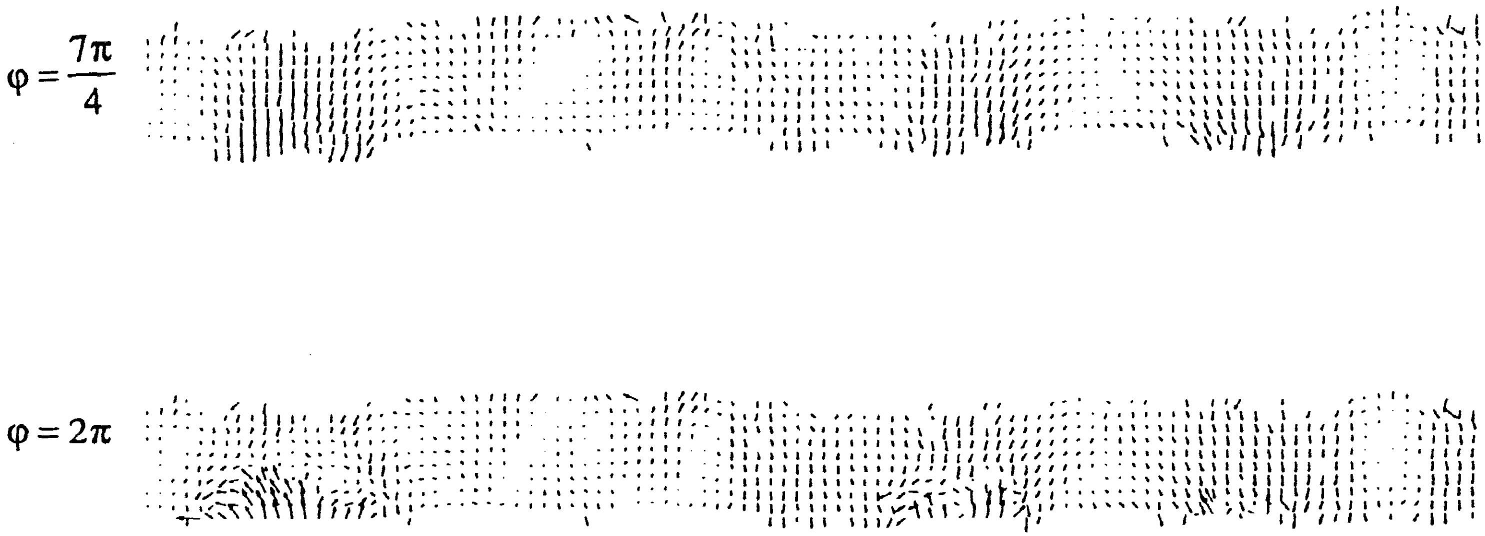

Figure A5.11d Mean velocity vector fields for phases $7\pi/4$ (y_b = -0.0359m, v = 1.58 m/s) and 2π (y_b = 0.0m, v = 2.23m/s). (Primary computational cell dimensions length × width = $100d \times 1d$

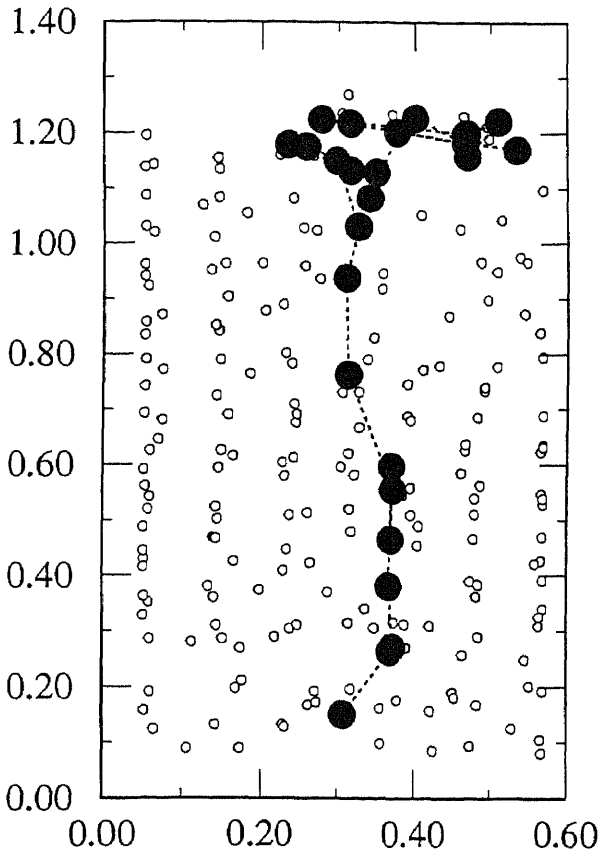

Figure A5.12 Trajectory a single large sphere of diameter D = 0.3m in a vibrated bed of small spheres d = 0.1m for a 6d×3d cell, f = 7 Hz, *amplitude* = $d/2$.

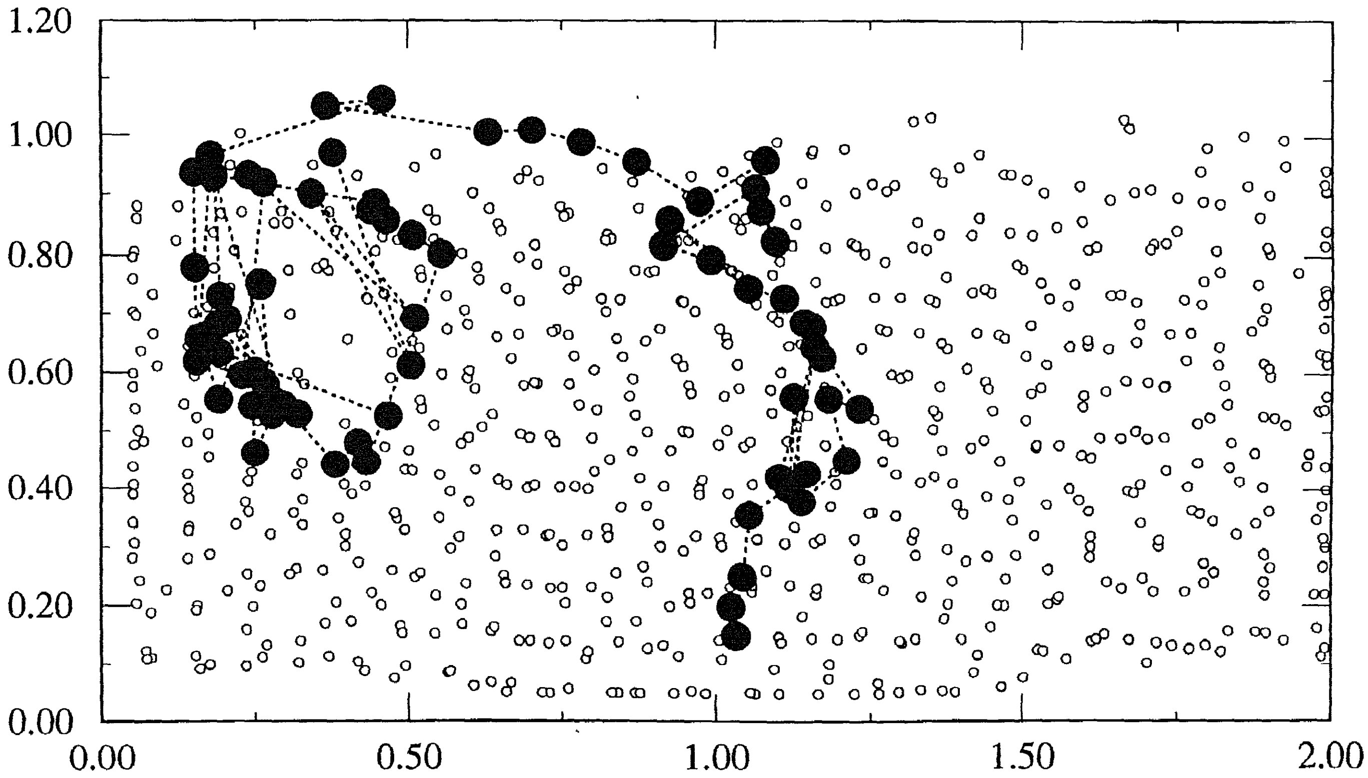

Figure A5.13 Trajectory a single large sphere of diameter D = 0.3m in a vibrated bed of small spheres d = 0.1m for a $20d \times 3d$ cell, f = 7 Hz, *amplitude* = $d/2$, and $\Gamma = 10g$.

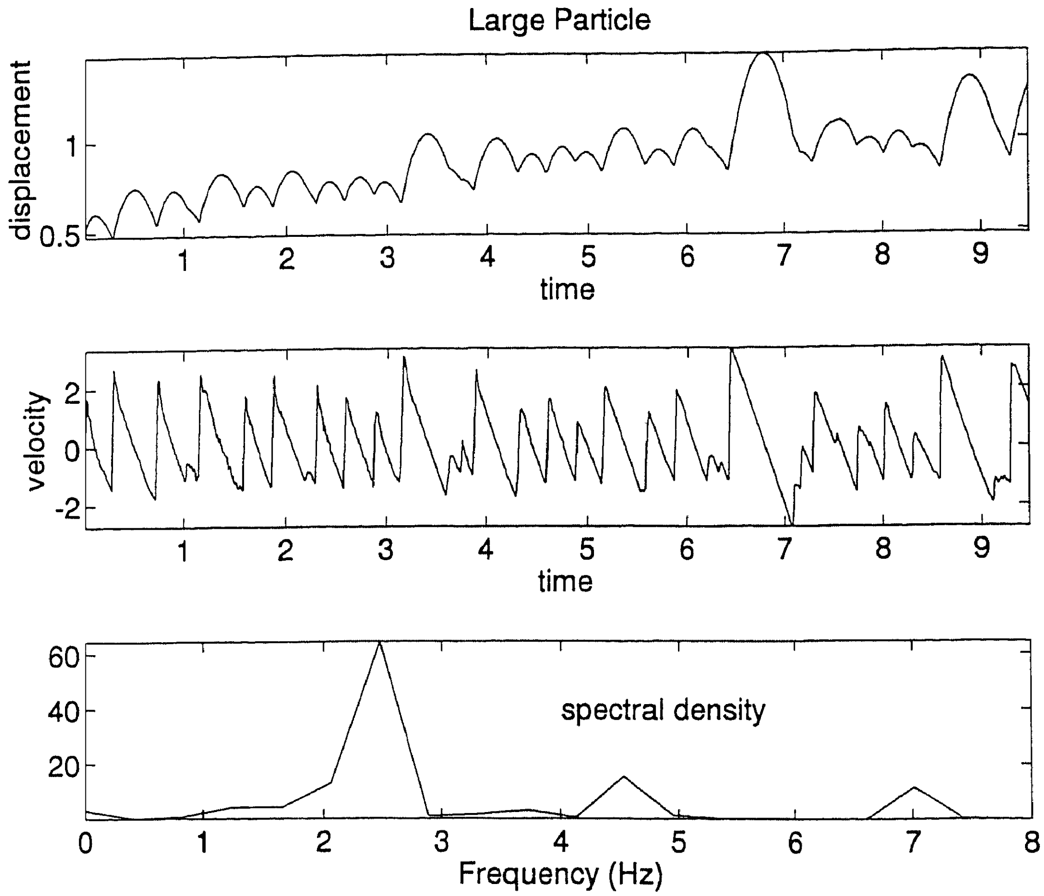

Figure A5.14a Displacement and velocity history and spectral density of a single large sphere initially placed in the center of the primary computational cell (*6d×3d)* for the case $D/d = 3$, $f = 7$ Hz, *amplitude* $= d/2$ and $\Gamma = 10g$.

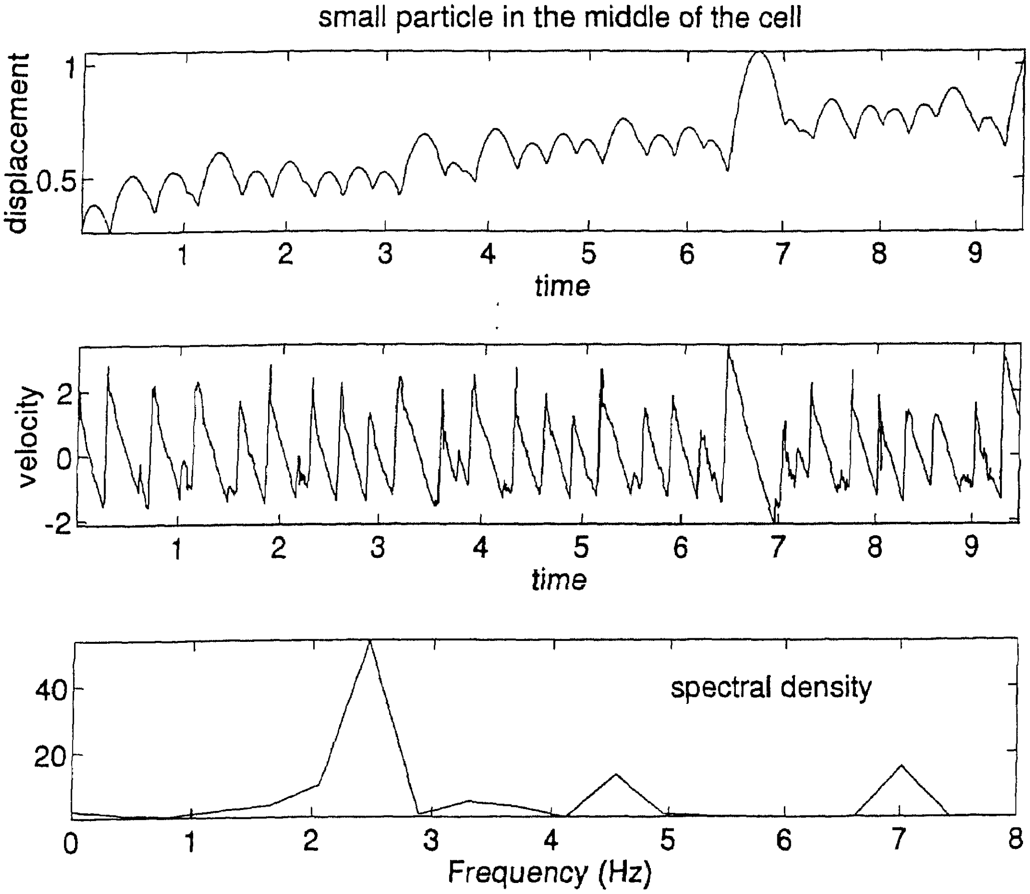

Figure A5.14b Displacement and velocity history and spectral density of a single bed sphere of diameter *d* beneath the large sphere for the case shown in Figure A5.14a where $D/d = 3$, $f = 7$ Hz, *amplitude* = $d/2$ and $\Gamma = 10g$.

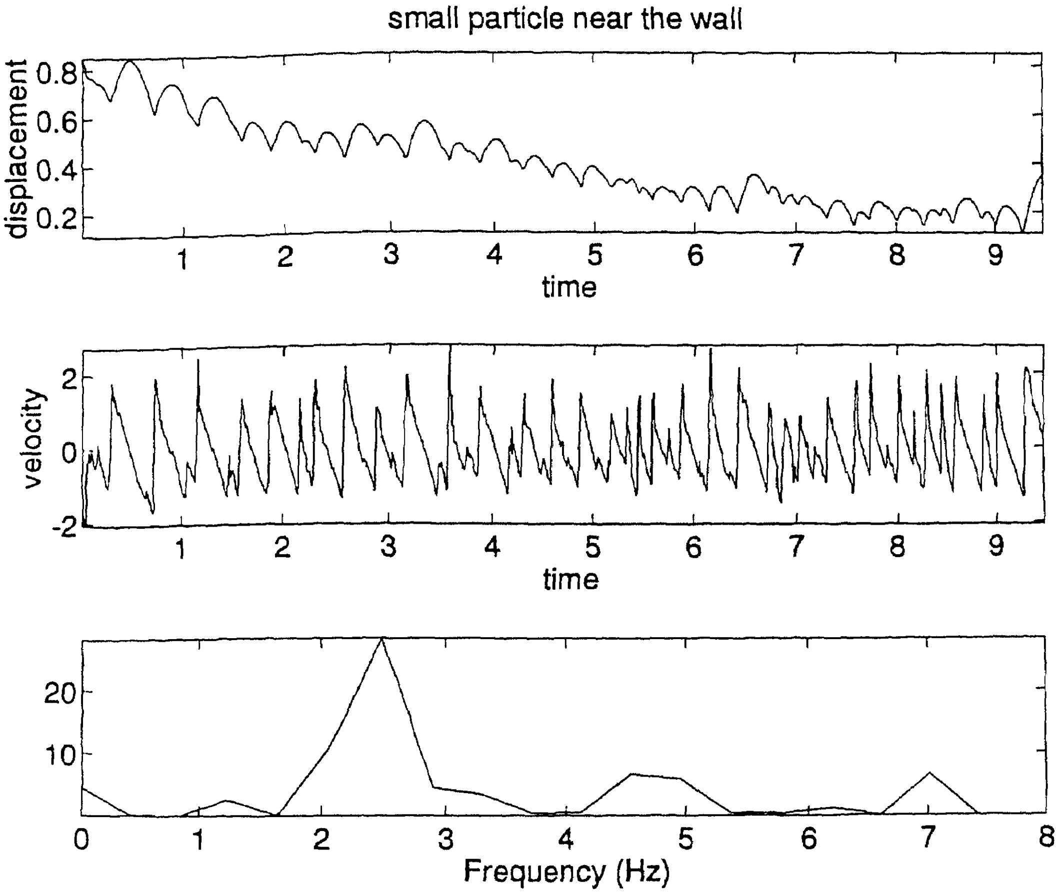

Figure A5.14c Displacement and velocity history and spectral density of a single bed sphere of diameter *d* adjaced to the side wall for the case shown in Figure A5.14a where $D/d = 3$, $f = 7$ Hz, *amplitude* = $d/2$ and $\Gamma = 10g$.

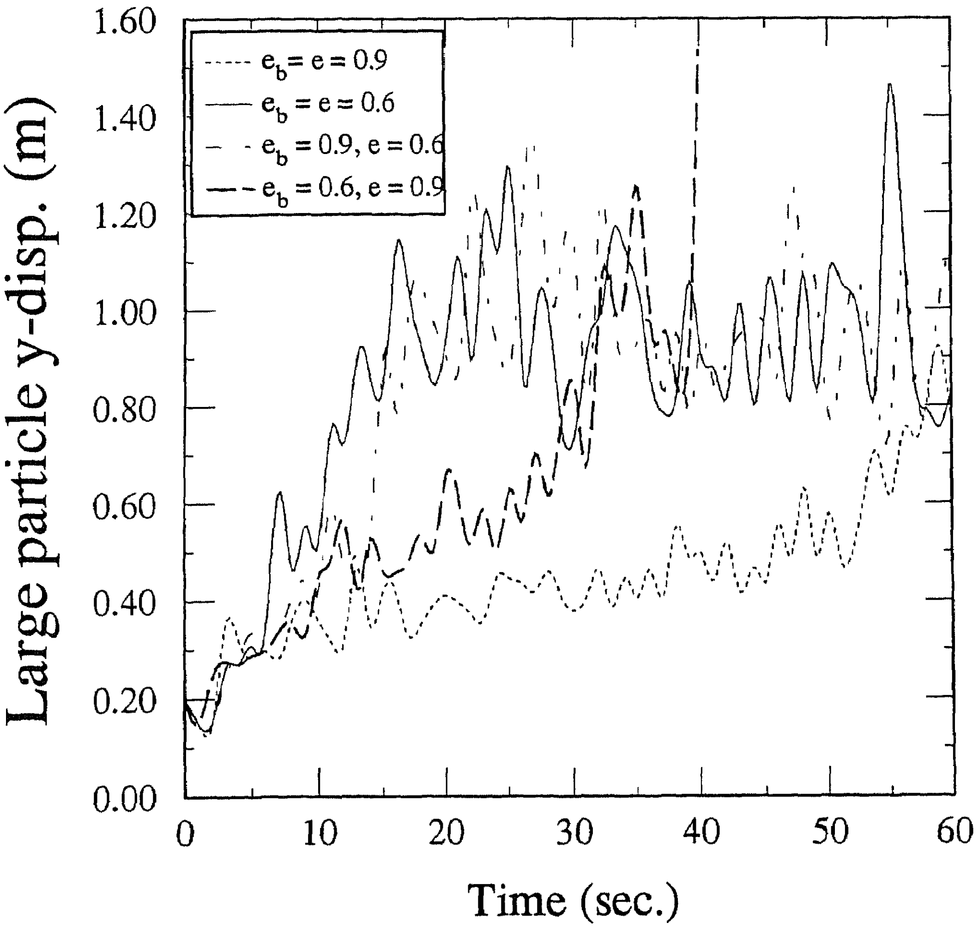

Figure A5.15 Vertical displacement history of a single large sphere of diameter D for different normal restitution coefficient pairs (e_b, e) $f = 7$ Hz, *amplitude* = $d/2$ and $\Gamma = 10g$

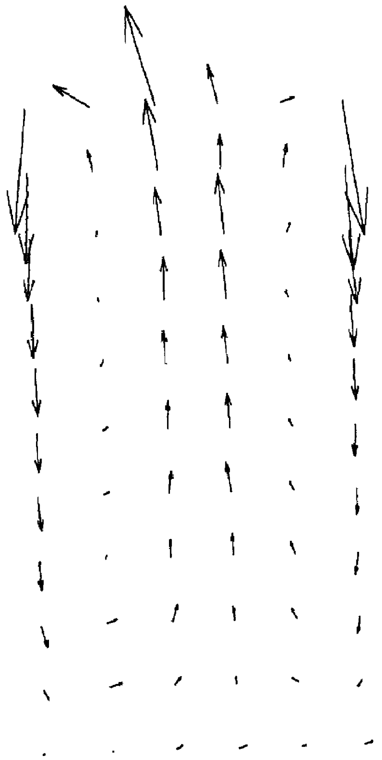

Figure A5.16a Mean velocity vector field for (e_b, e) = *(0.6, 0.6)* for the case where $f = 7$ Hz, *amplitude* = *d*/2 and $\Gamma = 10g$.

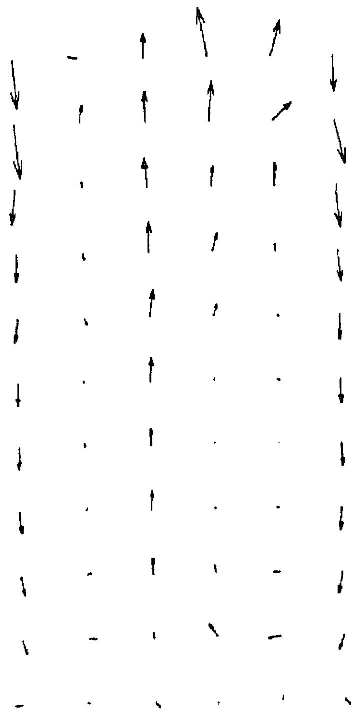

Figure A5.16b Mean velocity vector field for $(e_b, e) = (0.9, 0.9)$ for the case where $f = 7$ Hz, *amplitude* = $d/2$ and $\Gamma = 10g$.

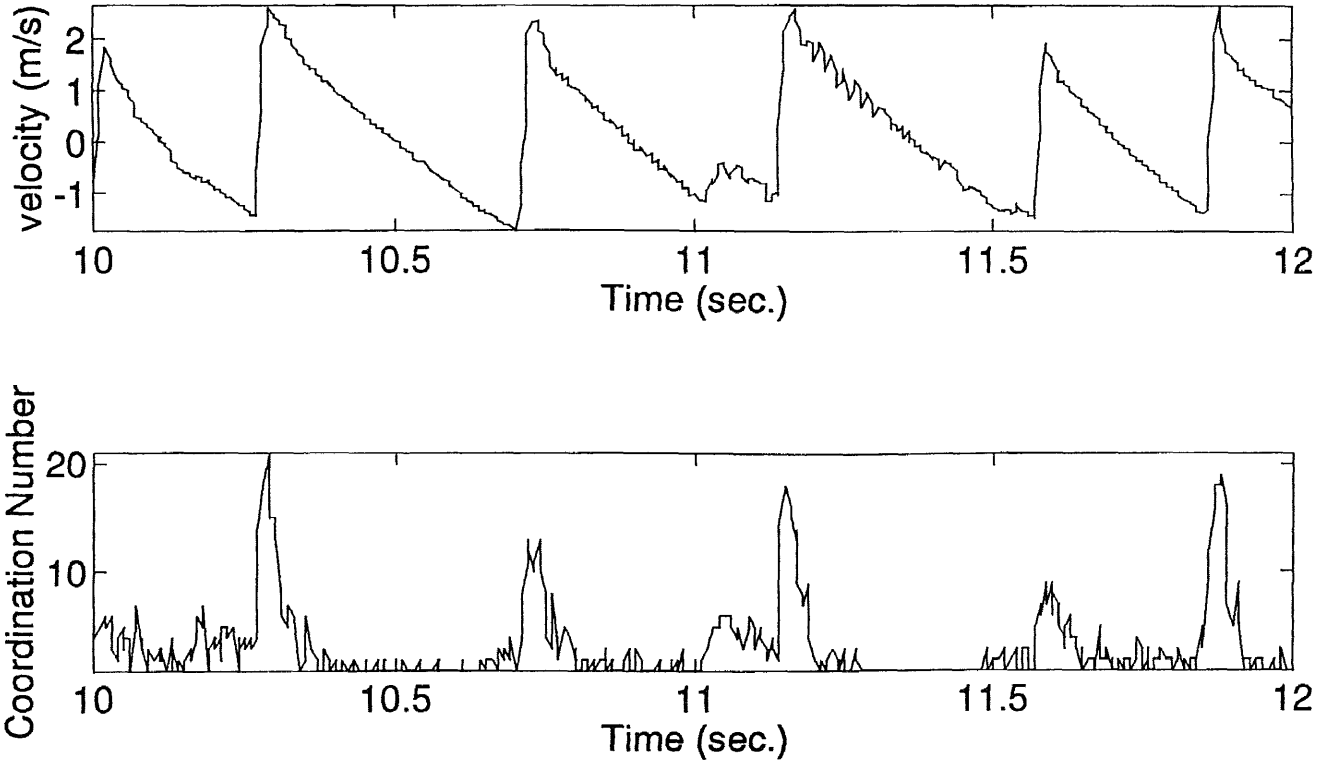

Figure A5.17 Coordination number and velocity (m/s) time histories of a single largesphere where $D/d = 3$ and $f = 7$ Hz, *amplitude* = $d/2$ and $\Gamma = 10g$.

REFERENCES

1. Savage, S. B. "Streaming Motions in a bed of Vibrationally Fluidized Dry granular Material." *J. Fluid Mech.* 194 (1988): 457-478.

2. Rosato, A.D., K. Strandburg, F. Prinz, and R. Swendsen. "Why the Brazil Nuts Are on Top: Size Segregation of Particulate matter by Shaking." *Phys. Rev Let.* 58 (1987): 38-1040.

3. Faraday, M., "On a Peculiar Class of Acoustical Figures Assumed by Groups of Particles upon Vibrating elastic Surface." *Phil. Trans. R. Soc. London,* 52 (1831): 299-340.

4. Jaeger, H. M. and S. R. Nagel." Physics of the Granular State." *Science* 255 (1992): 1523-1531.

5. Richman, M. W. and R. Martin."Boundary Conditions for Granular Flows at Randomly Fluctuating Bumpy Boundaries." *Mech Mat'ls* 16 (1,2) (1993):211-218.

6. Walton, O. R. and R. L. Braun. "Viscosity, Granular-Temperature, and Stress Calculations for Shearing Assemblies of Inelastic, Frictional Disks." *J. Rheology* 30 (5) (1986):949-980.

7. Gray, W.A. *The Packing of Solid Particles.* Chapman and Hall (1968): 87-122.

8. Shatalova, I. G., N.S., Gorbunoy, and J. L. Zambrow. "Perpectives in Powder Metallurgy." *Plenum Press* (1967)

9. Stewart, D. A. *High Quality Concrete.* .Spon Publ., London (1951).

10. Cussens, "The Packing of Solid Particles and Its Application" A. R., Ph.D. Dissertation, Univ. London, (1955)

11. Plowman, J. M. " Vibratory Compaction in Civil Engineering." *Rein.Concr. Rev.* 4 (3).(1956)

12. Macrae, J. C. and W. A. Gray, "The Packing of the Sphere." *Brit. J. Appl. Phys* 12 (1960):164

13. Evesque, P. and J. Rajchenbach. "Instability in a Sand Heap."*Phys. Rev. Lett.,* 62(1) (1989): 44-46.

14. Evesque, P., E. Szmatula and J. P. Denis. *"Surface Fluidization of a Sand Pile." Europhys. Lett.*12 (7) (1990): 623-627.

15. Bachmann, D. "Shallow Vibating Beds." *Verfahrenstechnik Z.V.D.I. Beiheft* 2(1940):43

16. Thomas, B., M.O. Mason,Y. A. Liu, and A. M. Squres."Identifying States in Shallow Vibrated Beds." *Powder Tech.*, 57 (1989):267-280.

17. Clement, E., and J. Rajchenbach. "Fluidization of a Bidimensional Powder." *Europhys. Lett.* 16(2) (1991):133

18. Hunt, M.L., S.Hsiau and K. T. Hong. "Particle Mixing and Volumetric Expansion in a Vibrated Granular Bed." *Proc. National Heat Transfer Confence.*(1993).

19. Mehta, A., and G.C. Baker. "Vibrated Powders: A Microscopic Approach." *Phys. Rev. Lett.*, 67(3) (1991):394-397.

20. Rajchenbach, J. "Dilatant Process for Convective Motion in a Sand Heap" *Europhys. Lett.* 16(2) (1991):149-152.

21. Taguchi,Y-h. "New Origin of a Convective Motion:Elastically Induced Convection in Granular Materials." *Phys. Rev. Lett.*, 69(9) (1992): 1367-1370.

22. Gallas, J. A., H. J. Herrmann, and S. Sokolowski."Convective Cells in Vibrating Granular media." *Phys. Rev. Lett.* 69(9) (1992): 1371-1374.

23. Savage,S.B., and R. Dai. "Some Aspects of Bounded and Unbounded Shearing Flow of Granular Materials." *Advances in Micromechanics of Granular Materials*, (eds. H. H. Shen, M. Satake, M. Mehrabadi, C. S. Chang, C. S. Campbell), Elsevier, Amsterdam (1991).

24. Zik, O., and J.Stavans."Self-Diffusion in Granular Flows" *Europhys. Lett.*16(3)(1991): 255-258.

25. O'Brien, K.T., A. D. Rosato, and Y. Lan. "Segregation in the Flow of Polymeric Particulates with Two Constituents." *Proc. of Annual Technical Meeting, Society of Plastics Engineers, Dallas, Tx.* (1990).

26. Williams, J. C. "Segregation of Powders and Granular Materials." *Fuel Soc. J.* Univ. Sheffield, 14 (1963): 29-34.

27. Bridgwater, J., and N. D. Ingram. "Rate of Spontaneous Inter-particle Percolation." *Trans. Instn Chem. Engr.* 49 (1971): 163-169.

28. Bridgwater, J., and N. W. Shape. "Particle Mixing by Percolation." *Trans. Instn Chem Engr.* 47 (1969): 114-119.

29. Ahmed, K., and I. J. Smalley. " Observation of Particle Segregation in Vibrated Granular System." *Powder Tech.* 8 (1973): 69-75.

30. Harwood, C.F. "Powder Segregation Due Vibration." *Powder Tech.* 16 (1977) 51-57.

31. Kawakita, K. "Some Consideration of Powder Particle Segregation by Tapping and Vibration." *Proc. of International Powder Technology & Bulk Granular Solid Conference.* (1971): 103-109.

32. Haff, P. K., and B. T. Werner. "Computer Simulation of the Mechanical Sorting of Grains." *Powder Tech.* 48 (1986): 239-245.

33. Rosato, A. D., F. Prinz, K. Strandburg, and R. Swendsen. " Monto Carlo Simulation of Particulate Matter Segregation." *Powder Tech.* 49 (1986): 59-69.

34. Lan, Y. "The Rate of Vibrational Segregation in Particulate Materials." MS Thesis, New Jersey Institute of Technology, (1989):33-40.

35. Rosato, A. D., Y. Lan, and D. Wang. " Vibratory Particle Size Sorting in Multi-Component Systems." *Powder Tech.* 66 (1991): 149-160.

36. Jullien, R., and P. Meakin. "Three-Dimensional Model for Particle-Size Segregation by Shaking." *Phys. Rev. Lett.* 69 (4) (1992): 640-642.

37. Knight, J. B., H. M. Jaeger, and S. R. Nagel. "Vibration-Induced Size Separation in Granular Media: The Convection Connection." *Phys. Rev. Lett.* 70 (24) (1993): 3728-3731.

38. Ogawa, S. "Multitemperature Theory of Granular Materials." Proc. US-Japan Seminar on Continnum-Mechanical and Statistical Approaches in the Machanics of Granular Materials, Tokyo (1978): 208-217.

39. Savage, S. B., and D. J. Jeffrey. "The Stress Tensor in a Granular Flow at High Shear Rates." *J. Fluid Mech.* 110 (1981): 255-272.

40. Lun, C. K. K., S. B. Savage, D. J. Jeffrey, and N. Chepurniy, " Kinetic Theories for Granular flow: Inelastic Particles in Couette flow and Slightly Inelastic particles in a General Flow Field." *J. Fluid Mech.* 140 (1984): 223-256.

41. Jenkins, J. T., and M. W. Richman. "Boundary Conditions for Plane Flows of Smooth, Nearly Elastic, Circular Disks." *J. Fluid Mech.* 171 (1986): 53-69.

42. Richman, M. W. "Boundary Conditions Based upon a Modified Maxwellian Velocity Distribution for Flows of Identical, Smooth, Nearly Elastic Spheres." *Acta Mechanica* 75(1988): 227_240.

43. Rosato, A. D., and H. Kim. " Particle Dynamics Calculations of Wall Stress and Slip Velocities For Couette Flow of Smooth Inelastic Spheres." *Continuum Mech. Thermodyn.* 61(1994): 1:20.

44. Kim, H., and A. D. Rosato. "Particle Simualtion of the Flow of Smooth Spheres between Bumpy Boundaries." *Advances in Micromechanics of Granular Materials*, (eds. H. H. Shen, M. Satake, M. Mehrabadi, C. S. Chang, C. S. Campbell), Elsevier, Amsterdam (1991).

45. Kim, H. "Particle Dynamics Modelling of Boundary Effects in Granular Couette Flow" Dissertation, New Jersey Institute of Technology. (1992).

46. Richman, M. W., and R. E. Martin. "Unconfined Granular Materials Thermalized by Fluctuating horizontal Surfaces." Proc. 9th conf. Engr. Mech. (ed. L.D.,Lutes, J. N., Niezwecki), ASCE, NY (1992):900-903.

47. Richman, M. W., and R. E. Mark. "The Effect of Anisotropic Boundary Vibrations on Confined, Thermalized, Granular Assemblies." to appear *J. Applied Mech.*

48. Verlet, L., "Computer 'Experiments' on Classic Fluids. I Thermodynamical Properties of Lennard-Jones Molecules." *Phys. Rev.*, 159 (1967):98-103.

49. Mindlin, R. D., and H. Deresiewicz, "Elastic Spheres in Contacts Under Varying Oblique Forces," *J. Appl. Meeh (Trans. ASME)*, 20 (1953):327.

50. Walton, O. R., "Numerical Simulation of Inelastic, Frictional Particle-Particle. Interactions." *Particulate Two-Phase Flow*, (ed. M. C. Roco), Butterworth-Heinemann, Boston..(1992)

51. Walton, O. R., H. Kim, and A. D. Rosato,"Microstructure and Stress Difference in Sheraing Flow." , *Mechanic Computing in 1990s and Beyond*, (1991):1249-1253.

52. Newland, D. N., *An Introduction to Random Vibrations and Spectral Analysis*, Longman, London and New York, 1975.

53. Allen, M. P., and D. J. Tildelay, *Computer Simulation of Liquid,* Oxford Science Publ, London, 1987.

54. Hansen, J. P., and I. R. McDonald, *Theory of Simple Liquid*, Academic Press, New York 1976.